DISSERTATION

FINITE ELEMENT CALCULATIONS OF ENERGY BARRIERS IN MAGNETIC SYSTEMS

ausgeführt zum Zwecke der Erlangung des akademischen Grades
eines Doktors der technischen Wissenschaften

unter der Leitung von
Univ. Doz. Dr. Thomas Schrefl
Institut für Festkörperphysik E138

eingereicht an der Technischen Universität Wien
Fakultät für Naturwissenschaften und Informatik

durch

Rok Dittrich-Rasovic
Rosengasse 12, 2601 Sollenau
Matt. Nr. 9426357

Wien, am 25. Mai 2003

TABLE OF CONTENTS

1 Introduction 8

1.1 High density magnetic recording and the superparamagnetic limit 8

1.2 Future storage media 10

1.2.1 Longitudinal media 11

1.2.2 Perpendicular media 11

1.2.3 Antiferromagnetically coupled media 12

1.2.4 High anisotropy media and self assembled particle arrays 12

1.2.5 Patterned media 13

1.2.6 Magnetic RAM 13

1.3 Thermal effects 15

1.4 Outline of the thesis 18

2 Micromagnetics at finite temperature 19

2.1 Rare but important events 19

2.2 Micromagnetic basics 21

2.3 Dynamics 22

2.4 Stochastic dynamics 24

2.5 The path method 26

2.6 Comparison of the methods 27

3 Finite element method 29

3.1 Calculation of the stray field 32

3.2 Mesh size dependency of the strayfield calculation in thin elements 33

3.3 Time integration 36

4 The Nudged elastic band method 37

4.1 Introduction 37

4.2 Equivalent ordinary differential equation 38

4.3 Spring force and definition of a length 42

4.4 Choosing the initial path 44

4.5 Criterion for stopping 44

4.6 Time integration 47

4.7 Spline interpolation 48

4.8 Climbing image NEB method 50

4.9 Examples 51

4.9.1 Interacting single domain particles 51

4.9.2 Small quadratic magnet 53

4.9.3 Elongated magnetic grain 54

4.9.4 Patterned granular media 58

4.10 A comment 60

5 Reversal modes and energy barriers in Discrete recording media 62
5.1 Introduction 62
5.2 Discrete ("patterned") media for perpendicular recording 63
5.3 Finite element model of discrete media with granular structure 66
5.4 Tree-algorithm 66
5.5 Hysteresis 68
5.6 Dipolar interactions 71
5.7 Writing speed 73
5.8 Multi domain structures 74
5.9 Energy barriers as a function of the intergranular coupling 76
5.9.1 Two coupled single domain grains 76
5.9.2 Grain boundaries in patterned media 78
5.10 Dependence of the energy barrier on the island si2e 82

6 Vortex core reversal by Bloch points 86
6.1 Introduction 86
6.2 Finite element model 89
6.3 Dynamic calculations 91
6.4 Direct computation of the energy barrier 95
6.5 Mesh size dependency 102

7 Configurational and shape anisotropy in permalloy platelets 103
7.1 Introduction 103
7.2 Configurational anisotropy 104
7.3 Results 105
7.3.1 Quadratic elements 107
7.4 Thermal switching 111

8 Thermally induced magnetization reversal in AFC media 115
8.1 Introduction 115
8.2 Results 116

9 Energy barriers in magnetic random access memory elements 122
9.1 Introduction 122
9.2 Model of the free data layer 122
9.3 Reversal modes at 1.12 mm size 124
9.4 Variation of the particle size 125
9.5 Stability of half selected cells 125
9.6 Field dependence of the reversal mode 128

10 comparison of langevin dynamics with energy barrier computation 131
10.1 Transition rates in squared soft magnetic elements 131
10.2 Summary 135

11 Outlook 136

12 Appendix **137**

12.1 Demo source code fora 2D example 137

12.1.1 Analyzing the "path.log" file 137

12.1.2 Changing the parameters 140

References **144**

Lebenslauf **151**

Curriculum Vitae **152**

List of publications **153**

Presentations **155**

Abstract

With decreasing size of magnetic nanostructures thermal effects become increasingly important. Prominent examples are magnetization noise in magnetic sensor elements and the thermal stability of MRAM (Magnetic Random Access Memory) cells or magnetic storage media. In this work we apply both stochastic time integration and path finding techniques in the framework of the finite element method, in order to simulate thermal effects in magnetic nanostructures. Thus, it is possible to take into account complex geometries and realistic element shapes. Both methods are complementary. The stochastic time integration is restricted to simulation times of about 10 ns. As a consequence the calculation of barrier crossing by stochastic time integration is limited to small energy barriers. The transition rate for large barriers can be estimated from the barrier height which can be calculated from the minimum energy path. In addition to the energy barrier, the elastic band method provides a global view of the energy landscape such as local minima and saddle points along the path. The magnetization processes as computed from the stochastic time integration method and the minimum energy path are compared for transitions between different ground states in magnetic nanoelements.

Studying reversal modes in small softmagnetic elements such as MRAM, complex processes were found even at sizes where homogeneous reversal was expected. As a consequence the corresponding energy barrier is lower than when estimated with simpler models. For thin permalloy squares a 8-fold like in-plane configurational anisotropy was observed at a certain size, a feature overlooked in previous studies. In granular patterned media the thermal reversal mode and the height of the energy barrier strongly depend on the intergranular exchange strength. Similarly, the energy barrier as function of the interlayer exchange is calculated for antiferromagnetically coupled media. For optimum exchange, the energy barrier can be increased by 15% as compared to conventional recording media without an increase of the coercivity. In softmagnetic nanodots a novel reversal mode involving Bloch-point structures was investigated. The observed switching fields agree well with experimental data. For small elements we compared the two methods and obtained good agreement of the predicted results. The calculated saddle points obtained with the nudged elastic band method indeed represent the transition state found with Langevin dynamics.

Kurzfassung

Mit abnehmender Größe von magnetischen Elementen werden thermische Effekte immer wichtiger. Beispiele sind magnetisches Rauschen in magnetischen Sensor-Elementen und die thermische Stabilität von magnetischen Speichermedien. In dieser Arbeit wenden wir stochastische Zeitintegration und Wegesuchetechniken im Rahmen der Finite-Element-Methode an, um thermische Effekte in magnetischen Strukturen zu studieren. So ist es möglich, komplizierte Geometrien und realistische Elementformen in Betracht zu ziehen. Die beiden Methoden ergänzenen einander. Die stochastische Zeitintegration ist auf Simulationszeiten von ungefähr 10 ns eingeschränkt. Daher ist die Berechnung von Energiebarrieren durch stochastische Zeitintegration auf kleine Barrieren begrenzt. Die Übergangsrate für große Energiebarrieren kann mit der Höhe der Energiebarriere abgeschätzt werden, die aus dem minimalen Energieweg berechnet werden kann. Zusätzlich zu den Energiebarrieren gibt die elastische Bandmethode eine globalere Ansicht von der Energielandschaft und liefert die lokalen Minima und Sattelpunkte entlang dem minimalen Energieweg. Die Magnetisierungsprozesse, die mittels der stochastischen Zeitintegrationsmethode und dem minimalen Energieweg berechnet wurden, werden für Übergänge zwischen unterschiedlichen Grundzuständen in magnetischen Nanoelementen verglichen. In kleinen weichmagnetischen Elementen wurden komplizierte Ummagnetisierungsmoden gefunden, obwohl bei kleinen Abmessungen Ummagnetisierung durch homogene Rotation erwartet wird. Durch inhomogene Ummagnetisierung sind die realen Energiebarrieren niedriger als die Barrieren, die mit einfachen Modellen für die Ummagnetisierung abgeschätzt werden. Für ein dünnes NiFe Plättchen wurde bei bestimmten Abmessungen eine 8-fache Anisotropie in der Ebene beobachtet. Diese Eigenschaft wurde in den vorhergehenden Studien bisher nicht gefunden. In nanostrukturierten Speichermedien hängt der thermische Ummagnetisierungspfad und die Höhe der Energiebarriere stark von der Stärke der intergranularen Austauschkopplung ab. Die Energiebarriere als Funktion der Zwischenschichtkopplung wurde auch für antiferromagnetisch gekoppelte Speichermedien berechnet. Durch die antiferromagnetische Kopplung kann bei optimaler Stärke für die Zwischenschichtkopplung eine um 15% höhere Energiebarriere erreicht werden als bei konventionellen Speichermedien mit gleicher Koerzitivfeldstärke. In weichmagnetischen Nanodots wurde ein Ummagnetisierungsmodus, der Blochpunkt Strukturen mit einbezieht, untersucht. Für kleine Elemente konnte eine gute Übereinstimmung der Resultate der stochastischen Zeitintegration und der elastischen Bandmethode erzielt werden.

Acknowledgment

Once Thomas inspired Dieter to join the micromagnetics group by explaining that micromagnetics is basically just about how "compass needles" arrange. In a fancy animation Dieter showed the gyromagnetic dancing of the "compass needels" during the magnetization reversal of a small magnetic recording element. This convinced me to try it myself, and I joined the micromagnetics group of Josef Fidler and Thomas Schrefl.

I would like to thank Thomas Schrefl for giving me the opportunity to work on exciting and challenging topics. His support, advice and encouraging words helped me a lot when sometimes things did not evolve as wanted. With his enthusiasm he showed, that almost everything can be done. If something did not work, he said "Wait, I'll help you", and things seemed much easier again. I would also like to thank him for the opportunity to attend many conferences and to visit other research groups all around the world. This gave me the chance to work with many interesting people, to exchange scientific knowledge but also to get to know the characters behind the names that I have only known from papers.

I want to thank my colleagues Hermann Forster, Dieter Suess, Werner Scholz and Markus Kirschner for a great time during work, on conferences but also for activities beyond physics. Thanks to Dieter and Werner I have become an enthusiastic windsurfer, although my first steps on the board in Santorini were a bit painful for my legs ;). A special thank to Werner for his technical support. His knowledge really saved us a lot of time with all computer related problems. The collaborations with my colleagues led to many joint publications and participations on conferences.

Josef Fidler´s effort to create a lively group of young physicists made a very good working atmosphere, and this should not be left unmentioned here.

The research visit to the group of Jacques Miltat at the CNRS Université Paris-sud was an unforgettable experience for me. Thanks to Andre I can now open Champagne bottles with a sword. Good teacher as he is I managed this at the first attempt.

Dominka, es gibt vieles wofür ich dir danken sollte. Danke für deine Geduld in Zeiten wo ich wieder einmal unansprechbar vertieft war in meine Programme. Ich danke dir auch dafür, dass du mir zur Seite gestanden bist und mich aufgebaut hast in den schwierigen Zeiten in meiner Familie.

Finally, I want to acknowledge the financial support of the Austrian Science Fund, Y-132 PHY and the EU Marie Curie Host Fellowship, ETNANOMAG HPMT-2000-00066.

1 INTRODUCTION

To introduce the scope of this thesis, the impact of thermal activation on magnetic data storage and theoretical methods to estimate the lifetime of stored data are reviewed. The basic concepts of new magnetic storage devices are explained. Both novel hard disc media and magnetic random access memories are discussed with respect to the superparamagnetic limit. Two complementary methods to treat thermal activation quantitatively are introduced. Finally, the outline of the thesis is given.

1.1 High density magnetic recording and the superparamagnetic limit

Every year the number of bits that are crammed onto each square inch of a commercial hard disk almost doubles (see Fig. 1.1). Fortunately this growth rate cannot continue forever because of physical limits. The limit in the case of hard disc drives is given by an effect called superparamagnetism. It denotes the phenomenon that the magnetic regions on the disk cannot retain their magnetic orientation (=the data) over the lifetime of the product when they become too small. Novel storage media can push this limit some steps further away. This work introduces new methods to estimate the lifetime of bits in these recently developed recording systems.

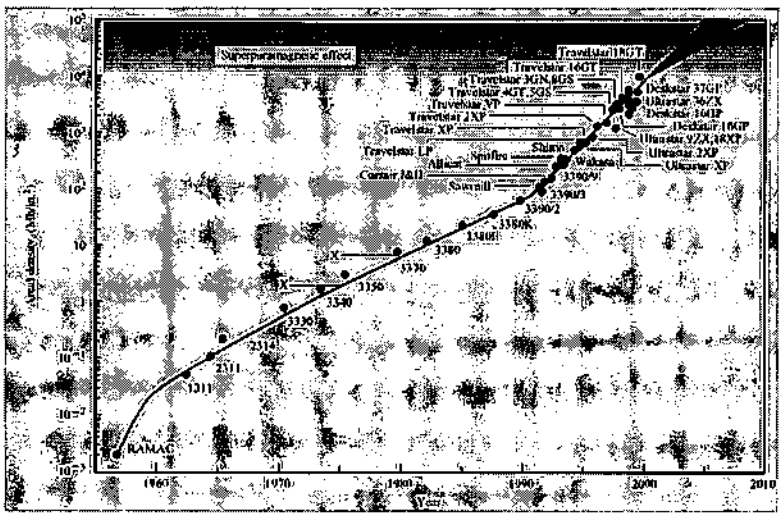

Figure 1.1 Evolution of the areal density (source IBM). Every year the density almost doubles. Current record achieved is 130 GBit $/in^2$.

The data layer in conventional magnetic hard drives consists of a thin granular magnetic film. The grains in this film are exchange decoupled thus each grain behaves like an independent single domain magnet. Each grain has two possible directions along which it can be magnetized. In order to store one bit of information, a rectangular region in the layer is magnetized by the recording head into one of its two directions. To guarantee the readability of the signal this region typically consists of at least 300 magnetic grains of the layer (see Fig. 1.2). In order to increase the areal density of the magnetic layer the size of the magnetic grains has to decrease which is impressively demonstrated in figure 1.2. Here the magnetic data layers of two hard discs are compared in a Transmission Electron Microscope (TEM). We compared a hard disc from the year 1988 with a newer one from the year 2000. In 12 years the areal density increased by a factor of about 1000 while the average grain size at same time drastically decreased. When the grains become too small these grains can switch from one equilibrium state to the opposite state because of thermal agitations. The signal becomes too weak and the data will be lost if the number of grains switched by thermal activation is too high.

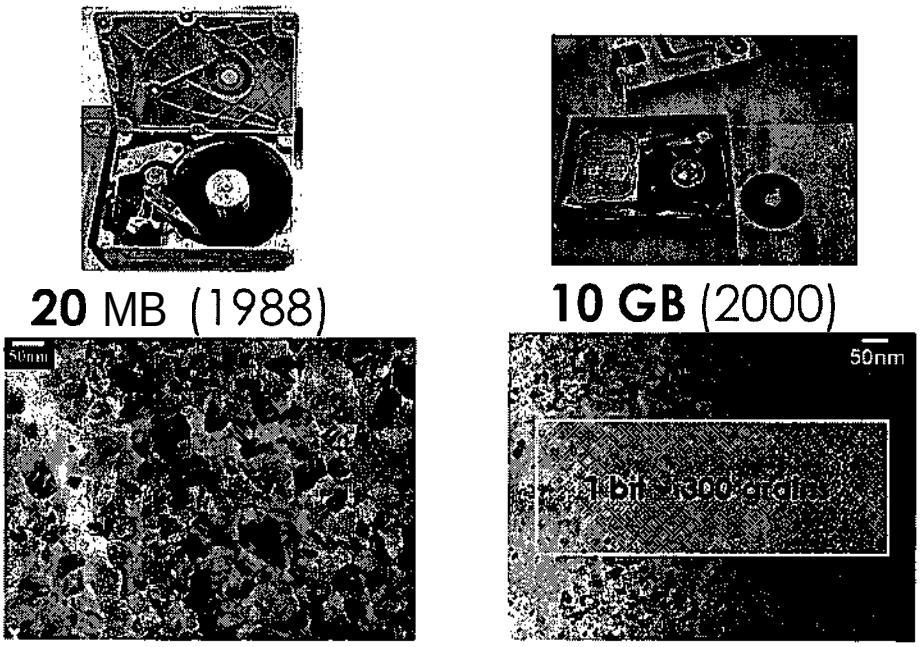

Sabine Höflnger, TEM brightfield, Institut für Festkörperphysik, TU-Wien, 2003

Figure 1.2 Comparison of two commercial hard disks. The bottom figures show TEM top views of the magnetic data kyer in bright field mode. The storage density has increased by a factor of 1000 in 12 years. As seen from the pictures this required a drastic decrease of the average grain size [61].

Considering the effect of superparamagnetism Charap [21] predicted in 1997 an areal density of 40 Gbits/in^2 as the upper bound. A new technology overcame this limit. In May 2001 IBM first shipped in the Travelstar laptop hard disk drives with antdferromagnetically-coupled (AFC) media. The current world record of 130 Gbits/in^2 was achieved by Read-Rite at the end of April 2002. (130 Gbits/in^2 = 20.15 Gbits/cm^2 = 2.52 GBytes/cm^2). This new level of storage density translates to 82 hours of DVD-quality video on a single disc.

1.2 Future storage media

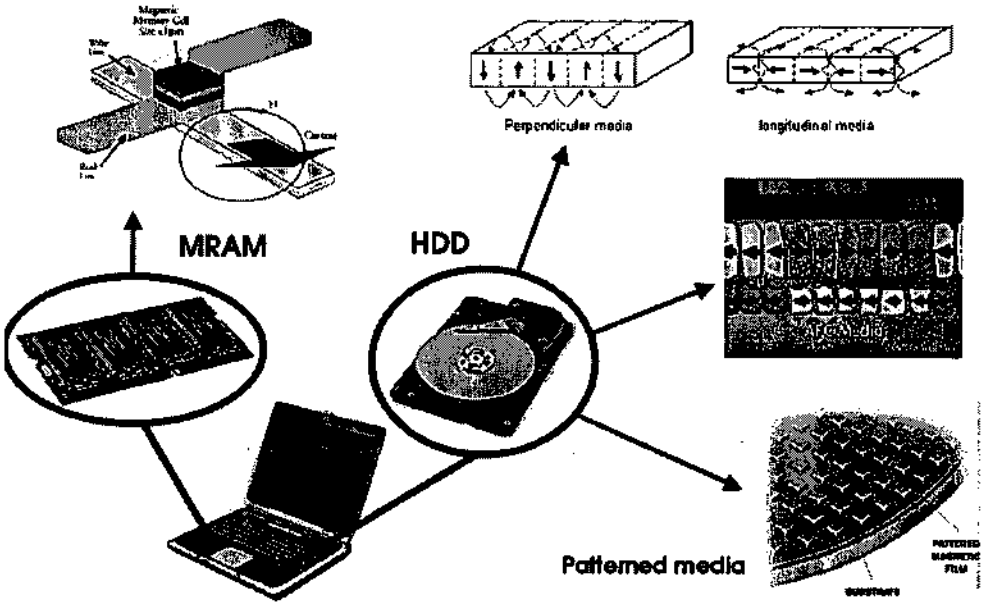

Figure 1.3 Future magnetic recording media.

There are several novel candidates to increase the thermal stability of the data. Fig. 1.3 shows some of the possibilities. Thermal stability is also important for the designing of magnetic random access memory (MRAM) elements. The idea here is to replace the conventional DRAM in a computer with a magnetic RAM. The advantage is low power consumption and non volatile storage with a high data rate comparable to the current DRAM technology. Another advantage is the robustness of the storage against radiation which makes it very interesting for applications in space.

1.2.1 Longitudinal media

In common hard disk drives the information is stored in the magnetization state of a ferromagnetic granular film. A granular film is a composition of grains, that are regions with the same crystal structure favoring the magnetization to align parallel to one axis, called easy axes. Usually neighboring grains have the same crystal structure but the easy axes are different. In modern hard disk drives the grain size diameter is less than 10 nm. In longitudinal recording the easy axes are randomly oriented in the plane of the film. One bit is represented by the magnetization state of about 50 neighboring grains. Because of the in-plane anisotropy in longitudinal recording the magnetization is parallel to the film plane. Small grains are required because the minimum bit length, below which neighboring transitions become indistinguishable, is determined by the transition width which in turn depends on the grain size of the film. Usually the grains are weakly exchange coupled to each other. For too strongly exchange coupled grains the magnetization in neighboring grains aligns parallel, effectively larger grains are formed. Thus, magnetic interaction increases the effective grain size. As a consequence larger bit lengths would be required. On the other hand completely decoupled grains are thermally unstable because the thermal stability decreases with decreasing grain volume. Thus, an important task in longitudinal recording is to find the optimal exchange coupling strength between grains.

In addition, the thermal stability is decreased by the strong demagnetizing field that opposes the magnetization. At low recording density, when the bit length is much larger than the film thickness the demagnetizing field is small. However, at high densities where the bit length becomes smaller than the film thickness the magnetic charges inherent to longitudinal recording are pushed together and high demagnetizing fields occur.

1.2.2 Perpendicular media

The idea of perpendicular recording is to represent bits with magnetization directions perpendicular to the film plane. As argued above a perpendicular orientation of the magnetization reduces the demagnetizing field in the high density limit. Thus, opposite bits act as domains that reduce the stray field. To achieve a perpendicularly magnetized configuration textured films with easy axes perpendicular to the film plane are used.

Another advantage of the aligned grains in perpendicular recording is a narrow switching field distribution. In conventional longitudinal media the grains are oriented randomly. Since

the switching field depends on the angle between the easy axis and the external field, some grains may not switch, leading to a broadening of the transition between the bits.

1.2.3 Antiferromagnetically coupled media

A breakthrough to decrease the demagnetizing field in longitudinal recording was achieved by antiferromagnetically coupled media (AFC). In contrast to common media where one ferromagnetic film stores the information, AFC media consist of two ferromagnetic films which are antiferromagnetically coupled. The opposite direction of the two films is achieved by an ultra-thin ruthenium layer which may be better known as "pixie dust". The opposite orientation of the films decreases the demagnetizing field which makes the entire multilayer structure appear much thinner than it actually is. However the thermal stability is proportional to the sum of the two layer thicknesses. Thus, concerning thermal stability the system appears to be thick.

1.2.4 High anisotropy media and self assembled particle arrays

Another possibility to increase the thermal stability is the use of high anisotropy materials. Thermal stability is proportional to the grain volume times the anisotropy. However, the strength of the field produced by the write head is limited which in turn imposes a limit on the media coercivity. One possibility to overcome the writing problem is to employ temperature assisted methods. A laser beam heats up the region where the bit is intended to be written. The anisotropy decreases with temperature which makes it possible to write it with fields of common write heads. Promising candidates for high anisotropy media are rare earth materials such as NdFeB, Co_5Sm, or FePt. For example the anisotropy of Co_5Sm is about 20 times larger than that of pure Co that is a typical hard disk material. Co_5Sm offers thermally stable grain diameters down to 2.8 nm.

A new fascinating approach are the so called self assembled particles, discovered by S. Sun et al. [104]. Chemical synthesis routes were applied to prepare FePt monodisperse particles. These monodisperse magnetic nanoparticles self assemble into a three dimensional array. The particle size that can be varied from 3-10 nm and the high crystalline anisotropy make self assembled FePt nanoparticles attractive for storage in the Tb/in^2 regime. Today various techniques exist to create self assembled particles.

1.2.5 Patterned media

Patterned media have long been proposed as a possible candidate for high density recording up to the Tbit/in² regime. It consists of a periodic array of discrete magnetic elements. Each element is exchange isolated from other elements but the grains within one element are strongly exchange coupled, thus more behaving like one large grain. The elements are sufficiently small so that the magnetization state is a single domain state. The two possible directions imposed by the crystalline anisotropy (usually perpendicular to the film plane) are interpreted as the binary 1 or 0. Since the superparamagnetic limit applies to the whole single bit, not to each of the many grains as in a conventional continuous multigrain bit, the volume and switching energy for the single-element bit in the patterned media are much larger than that of a single grain in conventional continuous media. This allows to scale down the size of the patterned elements without loss of thermal stability. Another advantage of patterned media is that transition noise between bits is eliminated because the bits are well separated by a non magnetic phase. The problem with patterned media is that, until now, there are no cheap and mass-production-compatible manufacturing methods. To compete in the magnetic storage market the net production cost of the hard disk needs to be preferably less than 1 US $[106,107] per disk! Currently existing techniques are far above this value and a breakthrough in the production technique will be needed to decrease the costs.

1.2.6 Magnetic RAM

You hit the power button on your television and it instantly comes to life. But do the same thing with your computer and you have to wait a few minutes while it goes through its boot-up sequence. Why can't we have a computer that turns on as instantly as a television or radio? Several companies are promising to launch a new technology in the next few years that will eliminate the boot-up process. Magnetic random access memory (MRAM) [30] has the potential to store more data, access that data faster and use less power than current memory technologies. In order to guarantee the high speed data access there are no moving parts in the MRAM storage. Instead the data is accessed trough a grid of current lines, where each crossing point carries one bit of data (one MRAM cell) and can be addressed individually.

The basic storage element of an MRAM cell is a small ferromagnetic thin film element. The element has two distinct magnetization configurations with the magnetization pointing in two opposite direction. The magnetization can be switched by a current line placed next the

the ferromagnetic cell (see Figure 1.4). For the read process the giant magneto resistance effect is used. One MRAM element usually consists of two magnetic layers with different coercivity that are separated by a non-magnetic or insulating interlayer. Depending on the angle of the magnetization between the two ferromagnetic layers the resistivity of the tri-layer changes. That effect called giant magneto resistance (GMR) was discovered in 1988 [9]. It did not solely drastically improve the performance of MRAMs but it is also used to increase the sensitivity in read heads of hard disc drives. In MRAM elements the magnetization of the hard magnetic layer represents the data bit. The data is written by a magnetic field that is applied by a current through a conductor line adjacent to the element. The field is strong enough that the hard magnetic element can be magnetized in the field direction. An opposite current changes the magnetization of the element. The magnetization direction of the soft magnetic film can be changed by a smaller current, that does not change the magnetization state of the hard magnetic film. The soft magnetic element is used to probe the state of the hard magnetic element. Depending on the state of the hard magnetic film and the imposed direction of the soft magnetic film the resistivity changes. MRAM elements are arranged in a rectangular array and are connected with conductor lines, allowing individual elements to be selected. The advantage of MRAM elements over common semiconductor-based dynamic random access memories (DRAMs) are low energy consumption and high storage densities. Furthermore MRAM elements are non-volatile storage devices so they retain information when the computer is switched off. To optimize the switching speed of MRAM elements a profound knowledge of the reversal process is important Micromagnetic simulations are a suitable tool to resolve in homogeneities during reversal that significantly influence the switching time. Further applications of magnetic nano-elements are sensors, magneto-electronics devices and magnetic logic gates [27,81].

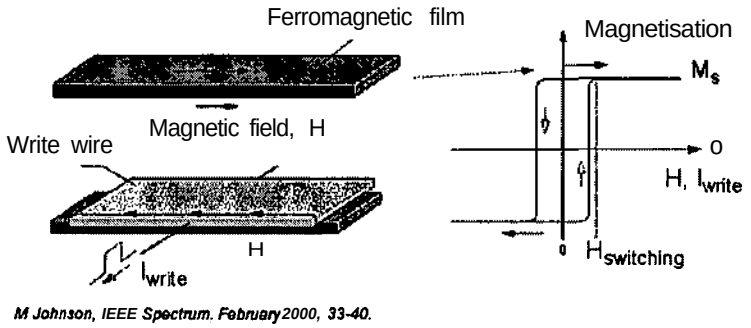

Figure 1.4 In a magnetic random access memory element the magnetization can occupy two stable states. This is used in data storage to write a bit either with a "0" or a "1". To switch between the states energy is needed (field has to be applied) which is reflected by the hysteresis.

1.3 Thermal effects

As outlined in the previous section thermal effects become increasingly important when the size of magnetic nanostructures becomes smaller and smaller. Prominent examples are the thermal stability of magnetic MRAM (Magnetic Random Access Memory) cells [88] and magnetic storage media [115] as shown in the previous section. Thermal effects also play a role on shorter time scales. An example is magnetization noise in magnetic sensor elements [99,13,119]. Magnetic sensors require a high sensitivity so that small magnetic fields can be detected. Thus, thermal fluctuations which will lead to thermal noise should be suppressed. The free layer of a multilayer sensor element is soft magnetic and may have a size well below one micrometer. Thermally induced magnetization processes may cause local or global magnetization rotations which cause the magnetization noise. With decreasing lateral extension of the elements thermal fluctuations become more pronounced. Magnetic RAM storage elements require a low and well defined switching field which in practice is limited by the current through the write line in an array of MRAM cells. On the other hand the shape or the induced anisotropy should guarantee a life time of a stored bit of about 10 years. Again the energy barrier for thermally induced magnetization reversal decreases with increasing size of the storage elements. The corresponding time scales differ by several orders of magnitude: Thermal noise

arises on a time scale of a few nanoseconds; thermally induced switching of the magnetization over energy barriers extends over seconds to years. Random thermal fluctuations of the magnetization are the underlying physical process which causes both thermal noise and spontaneous switching.

A micromagnetic system will be close to a local minimum of the total magnetic Gibbs' free energy. Thermal fluctuations of the magnetization cause the magnetization to wander around this minimum. Occasionally the system will reach a region next to a saddle point. The system may cross the energy barrier and move into the basin of attraction of a different energy minimum. This process can be described by the Néel-Brown theory [78,16]. The relaxation time, is the inverse of probability per unit time for crossing the barrier E_B. The attempt frequency, f_0, depends on material parameters, like anisotropy, particle shape, and damping [15]. Its value, which ranges from $f_0 = 10$ Hz to $f_0 = 10^{12}$ Hz, sets the time scale for thermally assisted magnetization reversal. Figure 1.5 shows demonstrates the crossing over an energy barrier for a MRAM cell. Thermal fluctuations drives the micromagnetic system from the stable region A to another stable region B in the energy landscape. The path with the smallest energy barrier is chosen since the population probability decreases exponentially with the energy of the system. To calculate the crossing point with the lowest energy one needs to find the relevant saddle points between the two stable regions. The example in Fig. 1.5 shows that the thermal switching between A and B passes a saddle point where the magnetization is in a two domain state.

The theoretical treatment of thermally induced magnetization processes starts from the stochastic Landau-Lifshitz-Gilbert equation and the corresponding Fokker-Planck equation [16]. The energy barrier can be calculated for coherent rotation in single domain particles and the formation of reversed domains in thin ferromagnetic wires. The attempt frequency can be estimated by solving the Fokker-Planck equation numerically or analytically [16,18,15,45,23]. Alternatively, the stochastic Landau-Lifshitz-Gilbert equation can be solved numerically for short time scales and small systems [48,117,18,91,92]. Recently, numerical solutions of the stochastic Landau-Lifshitz Gilbert equation were reported for extended micromagnetic systems [119,92]. Zhu [119] analyzed the magnetization noise in submicron sized sensor elements based on the numerical solution of the stochastic Landau-Lifshitz-Gilbert equation. The time integration of the stochastic Landau-Lifshitz-Gilbert equation is restricted to short times and is thus a proper tool to analyze magnetization noise. The calculation of long term

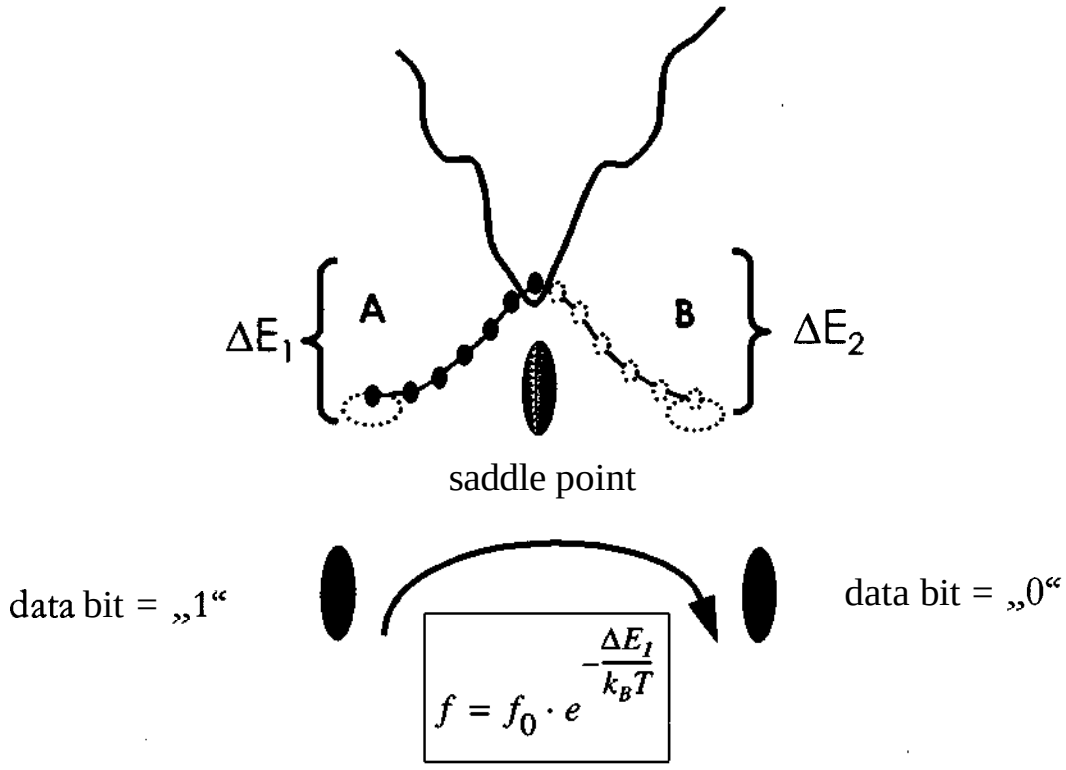

Figure 1.5 Thermal switching of the magnetization: fluctuations drive the magnetic system from the stable region A to another stable region ß in the energy landscape. The path with the smallest energy barrier is chosen since transition frequency decreases exponentially [18] with the height of the energy barrier. To determine the crossing point with the lowest energy the separating saddle points between the two regions needs to be calculated. An example for two stable regions are the stable states in an MRAM (data bit „1" or „0“). Switching between „0" and „1“ passes a saddle point where the magnetization is in a two domain state. The color code corresponds to the net-in-plane magnetization direction (red..."down“, blue..."up“).

thermal effects needs a detailed characterization of the energy landscape along the most probable path which is taken by the system to cross the energy barrier (see figure 1.5). The calculation of the energy barrier basically requires the calculation of the relevant saddle point. Berkov [11] calculated the transition path of interacting single domain particles by minimizing the action along the path. He showed that a direct minimization of the action may also give paths through local maxima which have to be excluded. Ren [37] proposed the "string method", a slightly modified version of the elastic band method [56], to calculate a minimum energy path in micromagnetic systems. Starting from an initial guess for the path which con-

nects two local minima of the system, a highly probable path is found by moving the points along the path according to an algorithm which resembles tensioning an elastic band across a mountain. Variants of elastic band methods are commonly used to calculate transition rates in chemical physics [57,75,83]. Once the energy barrier is calculated the Néel-Brown theory can be used to calculate the transition probability for the energy barrier crossing.

1.4 Outline of the thesis

In this work we apply both stochastic time integration and path finding techniques in the framework of the finite element method, in order to simulate thermal effects in magnetic nanostructures. Thus, it is possible to take into account complex geometries and realistic element shapes. Both methods are complementary. The stochastic time integration is restricted to simulation times of about 10 ns. As a consequence the calculation of barrier crossing by stochastic time integration is limited to small energy barriers. The transition rate for large barriers can be estimated from the barrier height which can be calculated from the minimum energy path. In addition to the energy barrier, the elastic band method provides a global view of the energy landscape such as local minima and saddle points along the path.

Section 2 introduces the basics of micromagnetic simulations at zero and finite temperature: A short introduction to the finite element method is given in section 3. Section 4 gives a detailed description of the method for finding minimum energy paths and saddle points in micromagnetics. Section 5 compares the reversal process in a perpendicular granular film, patterned media, and a single magnetic island. The effect of the intergrain exchange on the energy barrier is investigated. Section 6 deals with a novel reversal mode of vortex cores in permalloy disks using both quasistatic dynamics and the nudged elastic band method. The reversal involves the creation and displacement of a Bloch point singularity. Section 7 investigates configurational anisotropy in softmagnetic nanoelements. In section 8 the nudged elastic band method is applied to calculate optimal paths for the thermal switching in AFC media. In section 9 thermal reversal modes of the free layer in an elliptical MRAM cell are calculated. Finally, in section 10 we compare transition rates in Langevin simulations with results obtained from the nudged elastic band method for the thermal switching of small permalloy squares.

2 MICROMAGNETICS AT FINITE TEMPERATURE

Two complementary methods for the simulation of thermally activated magnetization processes are introduced: A path finding method based on the nudged elastic band method and a novel semi-implicit stochastic time integration scheme. As an example the transition probability between stable equilibrium states in magnetic sensor elements is calculated.

2.1 Rare but important events

An important problem in condensed matter physics and theoretical chemistry is the understanding of transition processes. In chemistry one is interested in reaction rates and diffusion processes. In micromagnetics we are interested in thermally activated switching events of submicron-sized magnetic elements. In magnetic storage applications these thermal switching events determine the long term stability of the stored information. The main difficulty in the computation of transition processes is caused by the disparity of the time scales. Let us consider a simple gradient system

$$\frac{dx}{dt} = -\nabla V(x) \tag{2.1}$$

$V(x)$ is the potential energy of the system. Without the presence of noise, the system would simply move towards the closest energy minimum of the potential. In the presence of noise however, the system can evolve away from the minimum and the whole configuration space can be explored by this type of stochastic dynamics.

If the thermal energy $k_B T$ is comparable to the energy barrier ΔE that separates two local energy minima, direct simulations of the escape over the energy barrier using Langevin equation^) are possible [90]. Unfortunately, this is no longer the case when $k_B T << \Delta E$ (either high energy barriers or low temperature limit) which is the case for most of the interesting problems. The time to escape from the energy minimum grows exponentially with the barrier height, the escape time is inversely proportional to the probability to escape from a local minimum of a barrier with barrier height AE

$$p_{escape} \propto exp\left(-\frac{\Delta E}{k_B T}\right) \tag{2.2}$$

Now two different time scales are involved. For a very long period the system stays in the vicinity of the energy minimum. And from time to time the system can overcome the energy barrier and switch to another minimum. These events occur very seldom and are therefore called "rare events". We are interested to calculate the probability of such "rare events" to occur.

An example where such events are crucial are magnetic storage media. Here data bits are stored in small magnetic elements where the magnetization can only occupy two stable states (energy minima). It is desired that spontaneous switching events between these states occur as seldom as possible, since they lead to the loss of stored data. The desired time scale for the stability is in the range of years and decades. On the other side the duration of the switching event itself takes only a few nanoseconds. The dynamics proceeds by long waiting periods around the local minima followed by sudden jumps from one state to another. In the simulation of the dynamics of the system most of the computation time is spent in resolving unimportant fluctuations around the minima. We would have to wait a for very long time to observe the interesting but rare switching events. This is what is meant with the "disparity of time scales". Various methods have been developed to speed up the computation and to overcome this problem [120,113].

When $k_B T << \Delta E$ the task simplifies because it is sufficient to find the lowest saddle point between the two energy minima. The height of the saddle point will then give the relevant energy barrier. The probability can then be calculated using the Arrhenius-Néel formula

$$f \propto f_0 exp\left(-\frac{\Delta E}{k_B T}\right) \tag{2.3}$$

f is the transition frequency and f_0 is the attempt frequency of the equation. The problem of finding the saddle point cannot be solved analytically except for simple situations. The reason is that at a saddle point neither a maximum nor a minimum should be achieved. The solution can only be found by solving the equation $\partial E/\partial x_i = 0$ and inspecting the Hessian matrix which leads to non-linear equations in the general case. We lack general methods for solving such systems. Instead we will use a path method which sources for highly probable paths between energy minima in high dimensional energy landscapes. Various methods exists to calculate such paths. We use the so called Nudged Elastic Band method (NEB) [56]. Starting from an initial guess for the path which connects two local minima of the system, a highly probable path is found by moving the points along the path according to an algorithm which

resembles tensioning an elastic band across a mountain. Using such a method we do not only obtain the saddle point(s) between energy minima, but also get a more global view of the energy landscape.

2.2 Micromagnetic basics

The micromagnetic description of a micromagnetic system starts from the total magnetic Gibbs' free energy [18,17]

$$E = \int \left(A\left[\sum_{i}^{x,y,z} (\nabla u_i)^2\right] + K_1[1-(\mathbf{u}\cdot\mathbf{a})] - \frac{J_s}{2}(\mathbf{u}\cdot\mathbf{H}_s) - J_s(\mathbf{u}\cdot\mathbf{H}_{ext}) \right) dV \tag{2.4}$$

E is the sum of the four underlying magnetic energy terms: the exchange energy, the anisotropy energy, the stray field energy, and the Zeeman energy; u denotes the unit vector parallel to the magnetization, A is the exchange constant, K_1 is the uniaxial magnetocrystalline anisotropy constant, a is the unit vector along the easy axis, and J_s is the spontaneous magnetic polarization. Fig. 2.1 explains the four basic energy contributions of equation (2.4). The integral (2.4) is over the total volume of the magnetic particles.

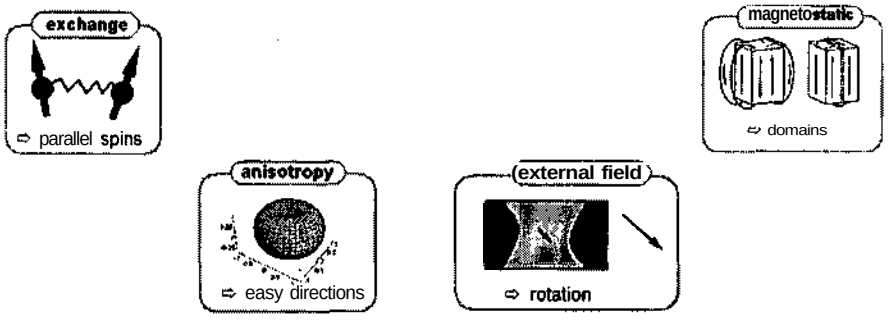

Figure 2.1 The four basic energy contributions of the total Gibb's free energy of a magnetic system. The exchange energy tries to align the spins parallel. Thus, it competes with the magnetostatic energy where closure domains are favorable. Additionally there can be a presence of a magnetocrystalline anisotropy which defines easy directions (low energy directions) of the magnetization. When a field is applied the zeeman energy part favors the alignment into the direction of the applied field.

Exchange energy

The exchange energy tries to align the magnetic spins parallel. This term is responsible for the arise of ferromagnetism and can be derived from quantum mechanics.

Magnetostatic energy

The exchange energy competes with the magnetostatic energy and breaks up large into smaller magnetic domains, since magnetic flux closure configurations are energetically favorable.

Anisotropy energy

Depending on the material there is a contribution of a magnetocrystalline anisotropy which defines easy directions (low energy directions) of the magnetization.

Zeeman energy

When a field is applied the Zeeman energy part favors the alignment of the magnetization into the direction of the applied field.

On micro- and nanometer scale the strength of energy contributions are of about same order. The competition between them is the reason for the large complexity and the numerous phenomena observed in magnets at these sizes.

In a stationary state the magnetic system occupies a local minimum of (2.4). Owing to thermal activation the system may overcome an energy barrier and spontaneously move towards a different local minimum of the energy.

2.3 Dynamics

At zero temperature the magnetization dynamics is described by the Gilbert equation of motion [51],

$$\frac{\partial \boldsymbol{J}}{\partial t} = -|\gamma|\boldsymbol{J} \times \boldsymbol{H}_{eff} + \frac{\alpha}{J_s}\boldsymbol{J} \times \frac{\partial \boldsymbol{J}}{\partial t}, \tag{2.5}$$

where $\boldsymbol{J}$ is the magnetic polarization vector, $\boldsymbol{H}_{\text{eff}}$ is the effective field, and J_s is the spontaneous polarization. $\boldsymbol{J}$ is assumed to be a continuous function of space. To obtain the general

form $\frac{dy}{dt} = f(t, y)$ foran ordinary differential equation (ODE), we transform equation (2.5) into the mathematically equivalent Landau-Lifshitz-Gilbert (LLG) equation

$$\frac{\partial \boldsymbol{J}}{\partial t} = -\frac{|\gamma|}{1+\alpha^2}\boldsymbol{J} \times \boldsymbol{H}_{eff} - \frac{\alpha}{1+\alpha^2}\frac{|\gamma|}{J_s}\boldsymbol{J} \times (\boldsymbol{J} \times \boldsymbol{H}_{eff}), \tag{2.6}$$

with the gyromagnetic ratio

$$|\gamma| = 2,210175 \times 10^5 \frac{\mathrm{m}}{\mathrm{As}}, \tag{2.7}$$

and the phenomenological Gilbert damping constant a. The first term on the right hand side of equation 2.6 describes the precessional motion of the magnetization in presence of a magnetic field, here the effective field $\boldsymbol{H}_{\mathrm{eff}}$. If taking this term only, the magnetic polarization $\boldsymbol{J}$ would move undamped on a cone around $\boldsymbol{H}_{\mathrm{eff}}$ with a precession frequency $\gamma \boldsymbol{H}_{eff}$. No energy would be dissipated, and the magnetic system would stay on an equipotential line in the corresponding energy landscape (2.4). The second term on the right hand side of (2.6) is the phenomenologically introduced dissipative term proportional to the generalized velocity $\partial \boldsymbol{J}/\partial t$. This damping term drives the magnetic polarization J towards the direction of the effective field. Equilibrium is reached when $\boldsymbol{J}$ and $\boldsymbol{H}_{\mathrm{eff}}$ are parallel. The magnetic system has then dissipated its energy and reached a local energy minimum of (2.4). The strength of the damping term is determined by the damping constant α. In magnetic recording media typical values for a are 0.02 [64]. This describes a relatively weakly damped system, and a dynamic treatment is important. Taking α=1 describes the high damping limit of (2.6). Here similar results are obtained when comparing energy minimization methods with the results obtained by integrating the equation of motion (2.6).

The simulation of the time evolution of the magnetization requires to calculate the effective field, $\mathbf{H}_{\mathrm{eff}}$, defined by the negative variational derivative of E. We use the finite element method to evaluate the total energy E of the magnetic system. The direction cosines of the magnetization, u_k, are interpolated by piecewise linear functions on a tetrahedral finite element mesh. In order to calculate the magnetic stray field, tt_y we use a hybrid finite element / boundary element method [44]. The effective field on the nodes of the finite element mesh may be approximated using a box scheme

$$\mathbf{H}^{l}_{\text{eff}} = -\frac{1}{\mu_0}\frac{\partial E}{\partial \mathbf{m}^{l}}, \tag{2.8}$$

where $\mathbf{m}^{l}$ is the magnetic moment associated with node l of the finite element mesh. More details about the finite element method are given in section 3.

2.4 Stochastic dynamics

The previous sections showed the finite element treatment of micromagnetic dynamics for the zero temperature limit. Powerful time integration methods can be applied since we are dealing with an ordinary differential equation. To introduce temperature into the dynamic equations a randomly fluctuating field is added to the total effective field. Equation (2.5) then transforms into

$$\frac{\partial \boldsymbol{J}}{\partial t} = -|\gamma|\boldsymbol{J}\times(\boldsymbol{H}_{eff}+\boldsymbol{H}_{th})+\frac{\alpha}{J_s}\boldsymbol{J}\times\frac{\partial \boldsymbol{J}}{\partial t}. \tag{2.9}$$

We can transform (2.9) into the mathematical equivalent stochastic Landau-Lifshitz-Gilbert (LLG) equation. The stochastic Landau-Lifshitz equation is a system of $3N$ Langevin equations with multiplicative noise [48]

$$\frac{\partial u^{l}_{i}}{\partial t} = A^{l}_{i}(t)+\sum_{k} B^{l}_{ik}(t)H^{l}_{\text{th},k}(t) \tag{2.10}$$

$$A^{l}_{i} = \left[-\frac{|\gamma|}{1+\alpha^2}\left(\mathbf{u}^{l}\times\mathbf{H}^{l}_{\text{eff}}\right)-\frac{|\gamma|\alpha}{1+\alpha^2}\left(\mathbf{u}^{l}\times\left(\mathbf{u}^{l}\times\mathbf{H}^{l}_{\text{eff}}\right)\right)\right]_{i} \tag{2.11}$$

$$B^{l}_{ik} = -|\gamma|\sum_{j}\varepsilon_{ijk}u^{l}_{j}-\frac{|\gamma|\alpha}{1+\alpha^2}\left(u^{l}_{i}u^{l}_{k}-\delta_{ik}\right) \tag{2.12}$$

where the indices i,j,k run over the three space directions, and the index $l = 1,\ldots,N$ runs over the number of nodes. The drift term, A^{l}_{i}, is the right hand side of the deterministic Landau-Lifshitz-Gilbert equation. a is the Gilbert damping constant and y is the gyromagnetic ratio. $\mathbf{H}^{l}_{\text{th}}$ is the random thermal field. The thermal field is assumed to be a Gaussian random process with the following statistical properties:

$$\left\langle H^{l}_{\text{th},i}(t)\right\rangle = 0 \quad \text{and} \quad \left\langle H^{l}_{\text{th},i}(t), H^{k}_{\text{th},j}(t')\right\rangle = 2D\delta_{ij}\delta_{lk}\delta(t-t') \tag{2.13}$$

The average of the thermal field, taken over different realizations, vanishes in each direction i in space. The thermal field is uncorrelated in time and space. The strength of the thermal fluctuations follows from the fluctuation-dissipation theorem [48]:

$$D = \frac{\alpha k_B T}{|\gamma| \mu_0 m_i} \tag{2.14}$$

Numerically the equations (2.10) to (2.12) are solved using a semi-implicit time integration method [35]. The time is divided into a lattice of discrete points t_n. The Langevin equation is solved in the time interval t_n to t_{n+1} with the initial condition $u_i^l = u_i^l(t_n)$. The right hand side of (2.10) is evaluated at the midpoint $t_n = (t_n + t_{n+1})/2 = t_n + \Delta t/2$. The update of the direction cosines is given by

$$\Delta u_i^l = A_i^l(\ldots, \bar{u}_i^{l-1}, \bar{u}_i^l, \bar{u}_i^{l+1}, \ldots)\Delta t + \sum_k B_{ik}^l(\ldots, \bar{u}_i^{l-1}, \bar{u}_i^l, \bar{u}_i^{l+1}, \ldots) \Delta W_{\mathrm{th},k}^l \tag{2.15}$$

with the noise integral

$$\Delta H_{\mathrm{th},k}^l = \int_{t_n}^{t_{n+1}} H_{\mathrm{th},k}^l(t)\,\mathrm{d}t \tag{2.16}$$

The magnetization direction at the midpoint of the time interval is

$$\bar{u}_i^l = \left(u_i^l(t_n) + u_i^l(t_{n+1})\right)/2 = u_i^l(t_n) + \Delta u/2, \tag{2.17}$$

assuming linearization of u_i within the time interval. The midpoint value, $\bar{u}_i^l$, is given implicitly by the equations (2.15) and (2.17) which is solved by functional iteration. Numerical tests show that about five iterations are sufficient to gain the required accuracy of 10^{-5}. From the midpoint value the magnetization at the time t_{n+1} is calculated from (2.17) and then normalized:

$$\tilde{u}_i^l(t_{n+1}) = 2\bar{u}_i^l - u_i^l(t_n), \quad \mathbf{u}^l = \tilde{\mathbf{u}}/|\tilde{\mathbf{u}}| \tag{2.18}$$

2.5 The path method

The previous section showed the numerical method for the simulation of thermal effects on short time scales. However transition events over large energy barriers ($> 50\ k_B T$) as in magnetic recording media occur on very long time scales (e.g. decades). It is clear that such events cannot be simulated directly by stochastic time integration methods. To simulate such events we directly search for the most probable path through the energy landscape for such an event. A common feature of path finding methods is the discrete representation of the path connecting the initial state of the system with its final state. First we construct a sequence of magnetic states from the initial magnetization state, $\mathbf{M}^{(i)}$, to the final magnetization state, $\mathbf{M}^{(f)}$. An optimization algorithm is then applied until at any point along the path the gradient of the energy is only pointing along the path. This path is called minimum energy path which means that the energy is stationary for any degree of freedom perpendicular to the path. The minimum energy path typically represents the path with the greatest statistical weight. From this path statistical quantities as the transition rate for the thermally induced magnetization reversal can be estimated.

Various other methods exist which can calculate either the saddle points (transition state) or the entire minimum energy path for the thermally activated barrier crossing. Most of these methods come from chemical physics and condensed matter physics where thermally activated barrier crossing is of great interest for the calculation of reaction rates. A nice overview methods for finding saddle points and minimum energy paths in high dimensional systems is given in [58].

Henkelman and Jónsson proposed the nudged elastic band method to calculate minimum energy paths [56]. We represent a path by a sequence of images. An initial path is assumed which connects the initial magnetization state $\mathbf{M}^{(i)} = \mathbf{M}^{(1)}$ with the final magnetization state $\mathbf{M}^{(f)} = \mathbf{M}^{(m)}$. The index k runs from 1 to m. The path is optimal, if for any image $\mathbf{M}^{(k)}$ the gradient of the energy is only pointing along the path or in other words the component of the energy gradient normal to the path, D, is zero. If t denotes the unit tangent vector along the path, a minimum energy path has the following property

$$\mathbf{D}^{(k)} = \nabla E(\mathbf{M}^{(k)}) - [\nabla E(\mathbf{M}^{(k)}) \cdot \mathrm{t}]\, \mathbf{t} = 0, \quad \text{for } k = 1,\ldots,m \tag{2.19}$$

The optimal path can be found using an iterative scheme. In each iteration step the images move towards lower energy in a direction perpendicular to the path. So the image $\mathbf{M}^{(k)}$ is moved into the direction, $-\mathbf{D}^{(k)}$. Figure 2.2 shows the calculation of $\boldsymbol{D}_k$. In order to keep an equal distance between successive images a spring force may be introduced [56]. A more detailed description of the method and the implementation in our simulation package is given in section 4.

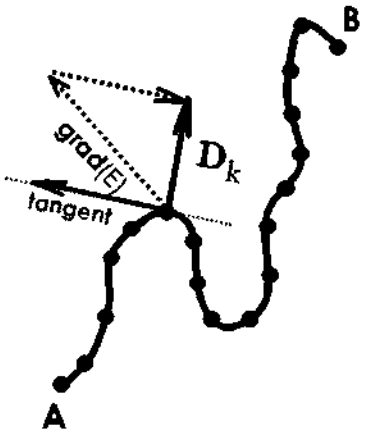

Figure 2.2 Schematic representation of the path, with shows how $\boldsymbol{D}_k$ in equation (2.19) is calculated. A number of images is chosen to discretize the path connecting the two states A and B.

2.6 Comparison of the methods

Figure 2.3 compares the transition between two stable minimum energy configurations of a 150 x 100 x 5 nm^3 thin film element [34] calculated with stochastic time integration and the elastic band method. In the top figure sequence the minimum energy path is shown for the reversal between two S-states. The bottom figure sequence shows the dynamic thermal switching between a C-state and a S-state. With both methods we obtain the same transition state.

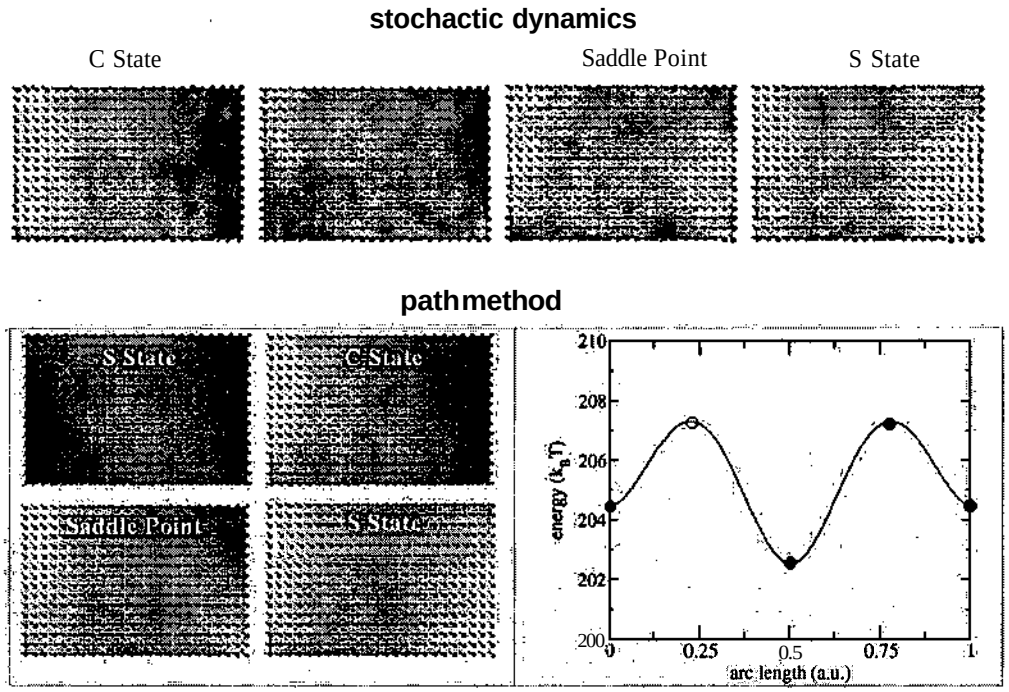

Figure 2.3 Thermal switching between the S-state and the C-state in NiFe platelets. The element size is 50 x 100 x 5 nm^3. Top: Magnetization states at 300K in a NiFe platelet at zero applied field. Bottom, left: Magnetization configurations along the minimum energy path: S-state, saddle point (not shown), C-state, saddle point, inverted S-state. Bottom right, right: Energy along the minimum energy path.

3 FINITE ELEMENT METHOD

This section gives a short introduction to the finite element method which is used to discretize the micromagnetic equations. Both for the time integration of the stochastic LLG equation, and for the nudged elastic band method the numerical treatment starts with the discretization of the total Gibbs' free energy of the magnetic system. The effective field and the gradient of the energy are derived as the functional derivative of the total energy.

In order to be able to perform numerical calculations and simulations with a computer we first have to formulate the problem in a way that the computer can understand. Our region of interest, the magnetic region, must be expressed as a finite number of evaluation points in space, where each point has a corresponding region surrounding it. The regions are constructed in a way so that there is no overlap between them. The solution of the equations can be evaluated numerically on each of these points. Two ways of discretizing the regions can be used: The finite differences method simply uses a homogeneous mesh of rectangular prisms. More complex element types are used in the finite element method. In our simulation package we use tetrahedral finite elements. Surfaces are meshed with triangles.

The advantage of the finite differences method is, that it gives a simpler formulation of the discretized equations than the finite element method. In addition a fast and powerful algorithm, FFT (Fast Fourier Transformation), can be applied to solve the time consuming evaluation of the demagnetizing field. The advantage of the finite element method however is the great flexibility in the modeling of the magnets (see figure 3.1). Complex shapes and granular materials can be modeled. The mesh size can be adapted where needed and kept coarse in less important regions. In many cases this gives a drastic speed up as compared with a homogeneous mesh. An example are circular soft magnetic dots where the mesh size has to be fine only at the position of the magnetic vortex core.

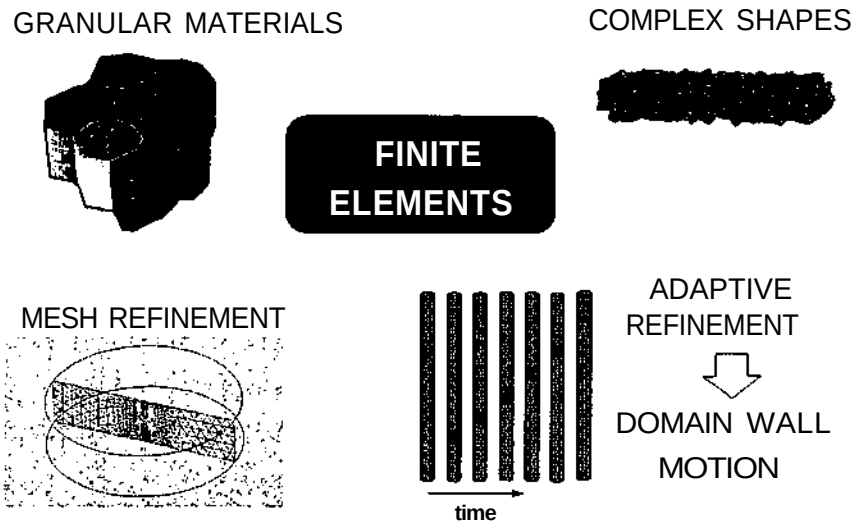

Figure 3.1 Using finite elements to discretize the magnetic region gives great flexibility in the modeling. Complex shapes and granular materials can be modeled. Moreover the mesh size can be adapted where needed, and can also be changed during the simulation itself.

The mesh can also be changed during the simulation itself. During the motion of a domain wall through a magnetic wire, the mesh is adapted while the simulation proceeds. The mesh is fine at the position of the wall and coarse in the rest of the magnet. This gives the impression that a region with fine mesh size moves together with the domain wall („moving mesh“).

We use the finite element method to simulate thermal effects both on short and long time scales with the two methods as introduced in section 2. For both methods the numerical treatment starts with the discretization of the total Gibbs' free energy E (see equation (2.4)). The magnetic polarization $\boldsymbol{J}(\boldsymbol{x})$ is expanded with piecewise linear basis functions $\varphi_i(\boldsymbol{x})$. For one component of $\boldsymbol{J}$ we can write

$$J^k(\boldsymbol{x}) \approx J^k_{app}(\boldsymbol{x}) = J_s(\boldsymbol{x}) \sum_{i=1}^{n} u_i^k \varphi_i(\boldsymbol{x}). \tag{3.1}$$

$J^k_{app}(\boldsymbol{x})$ is the finite element approximation of the k - th component of the magnetic polarization. The coefficient u_i^k denotes the k-th component of the normalized spontaneous

polarization ($|u_i^k| < 1$) on the node point i. The number of unknowns (u_i^k) is three times the number of node points of the finite element mesh.

To perform the time integration, we have to calculate the effective field on every node point of the finite element mesh. However we cannot directly use the analytic formula for the effective field, which follows from the negative functional derivative of the total Gibbs' energy (2.4) as,

$$\boldsymbol{H}_{eff} = -\frac{\delta E_t}{\delta \boldsymbol{J}} = \frac{2A}{J_s^2}\Delta \boldsymbol{J} + \frac{2}{J_s^2}K_1(\boldsymbol{J}\boldsymbol{a})\boldsymbol{a} + \boldsymbol{H}_S + \boldsymbol{H}_{ext} \,. \tag{3.2}$$

Here A is the exchange constant, K_1 is the magnetocrystalline anisotropy constant, a is the unit vector parallel to the anisotropy axis, $\boldsymbol{H}_s$ is the magnetostatic stray field, and $\boldsymbol{H}_{ext}$ is the external applied field. The first term on the right side of equation (3.2) is the exchange field. Its calculation needs the second derivative of the magnetic polarization. Numerically the second derivatives cannot be calculated directly using linear basis functions. In addition, the calculation of the stray field which follows from the gradient of a scalar potential is crucial. With linear basis functions the gradient of the potential, which is proportional to the stray field, is only defined within an element but not on the node points. To overcome this problem we start from the total Gibbs' energy for a ferromagnetic particle [18]

$$E_t = \int_n e_t(\boldsymbol{J})dV = \int_n \left(A\left[\sum_k^{x,y,z} (\nabla u_k)^2\right] + K_1[1-(\boldsymbol{u}\boldsymbol{a})^2] - \frac{1}{2}J_s\boldsymbol{u}\boldsymbol{H}_s - J_s\boldsymbol{u}\boldsymbol{H}_{ext} \right) dV \,. \tag{3.3}$$

The exchange energy, the anisotropy energy, the strayfield energy and the Zeeman energy contribute to the total energy [18]. The second term is the simple uniaxial anisotropy energy. It would be no problem to replace it with any other form of anisotropy energy. We neglect the contributions to the total energy which arise from the conversion of the true microscopic exchange and dipole interactions to the continuum form as well as intrinsic surface anisotropy [18].

The total energy is an integral over the particle volume. For the magnetic polarization J the expansion according to (3.1) is used. The k-th component of the effective field on node i is approximated using the box scheme [49],

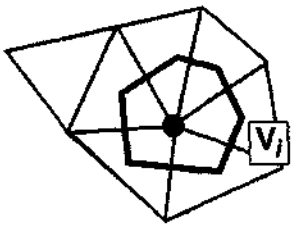

Figure 3.2: The volume *Vj* surrounding the node /' shown in a 2 dimensional example.

$$H^k_{i\,eff} \approx -\frac{1}{m_i}\frac{\partial E_t}{\partial u^k_i}, \tag{3.4}$$

where m_i denotes the magnetic moment on the node point i. It follows from the integral

$$m_i = \int_{V_i} J_s(x)dV. \tag{3.5}$$

V_i is the surrounding volume (figure 3.2) of the node i, such that

$$\sum_j Vj = V \text{ and } V_i \text{n } Vj = 0 \text{ for } i \neq j. \tag{3.6}$$

Usually, in a single phase magnetic material the spontaneous polarization, J_s, is constant in space. However, the spontaneous polarization is a function of space and is discontinuous at grain boundaries if a magnet with different magnetic phases is modeled. In our model the nodes of the finite elements are located at grain boundaries. Regions with different values of the spontaneous polarization surround these points. Thus, we assume an average magnetic moment for these nodes as given by (3.5).

3.1 Calculation of the stray field

The most time consuming part in the calculation of the effective field is the long range magnetostatic interaction which is described by the stray field $\boldsymbol{H}_S$. The stray field $\boldsymbol{H}_S$ is obtained from a boundary value problem,

$$\text{AM} = \frac{\nabla J_s}{\mu_0} \text{ and } H_S = -\text{V«} \tag{3.7}$$

To apply the boundary condition $u = 0$ at infinity, a hybrid finite element boundary element method [43] is used. No finite elements are needed outside the magnetic particle to solve the boundary value problem (3.7). This is the advantage of the hybrid FE/BE method. For the solution of equation (3.7) with the hybrid FE/BE method one Poisson equation with Neumann boundary conditions and one Laplace equation with Dirichlet boundary conditions have to be solved. To obtain the boundary conditions a matrix vector product has to be performed. We split the total magnetic potential u into two parts, $u = u_1 + u_2$. The potential u_1 solves the Poisson equation (3.7) inside the magnetic particles with Neumann boundary conditions at the surface of the magnets and it is zero outside the magnets. The potential u_2 solves the Laplace equation everywhere in space and shows a jump at the surfaces of the magnets. Thus, «2 is the potential of a dipole sheet at the surfaces of the magnet. After discretization the integral operator may be expressed as a matrix vector product

$$u_2 = Bu_1 \tag{3.8}$$

The storage requirement for the matrix B is the bottleneck of the method since B is a fully populated $N_S \text{X} N_S$ matrix. N_S is the number of boundary nodes. Especially for thin films the method loses efficiency since most of the nodes are located at the boundary. To overcome this problem two novel boundary methods were developed. For details see the thesis of H. Forster [41].

3.2 Mesh size dependency of the strayfield calculation in thin elements

The mesh size which has to be used in a particular problem is determined by the characteristic lengths [3], the Bloch parameter

$$\delta_0 = \sqrt{\frac{A}{K_1}}, \tag{3.9}$$

and the exchange length

$$l_{ex} = \sqrt{\frac{2\mu_0 A}{J_s^2}}. \tag{3.10}$$

The mesh size must be smaller than the smallest of these values.

In some cases this is not sufficient. Care has to be taken when simulating thin platelets. Here it is important to adapt the mesh near the edges when the magnetization is in-plane. As an example Fig. 3.4 shows the mesh size dependency of the magnetostatic energy calculation for a 75x75x5 nm³ permalloy platelet. The element was magnetized uniformly in-plane. We compare the magnetostatic self-energy for three meshes with the exact theoretical value [1] (see Fig. 3.3). The results are shown in table 1 and figure 3.4.

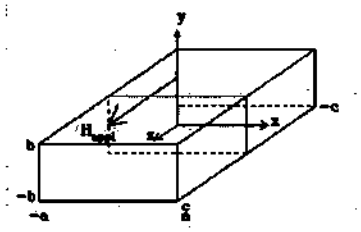

$$\pi D_z = \frac{b^2-c^2}{2bc}\ln\left(\frac{\sqrt{a^2+b^2+c^2}-a}{\sqrt{a^2+b^2+c^2}+a}\right) + \frac{a^2-c^2}{2ac}\ln\left(\frac{\sqrt{a^2+b^2+c^2}-b}{\sqrt{a^2+b^2+c^2}+b}\right) + \frac{b}{2c}\ln\left(\frac{\sqrt{a^2+b^2}+a}{\sqrt{a^2+b^2}-a}\right) + \frac{a}{2c}\ln\left(\frac{\sqrt{a^2+b^2}+b}{\sqrt{a^2+b^2}-b}\right)$$

$$+ \frac{c}{2a}\ln\left(\frac{\sqrt{b^2+c^2}-b}{\sqrt{b^2+c^2}+b}\right) + \frac{c}{2b}\ln\left(\frac{\sqrt{a^2+c^2}-a}{\sqrt{a^2+c^2}+a}\right) + 2\arctan\left(\frac{ab}{c\sqrt{a^2+b^2+c^2}}\right) + \frac{a^3+b^3-2c^3}{3abc}$$

$$+ \frac{a^2+b^2-2c^2}{3abc}\sqrt{a^2+b^2+c^2} + \frac{c}{ab}\left(\sqrt{a^2+c^2}+\sqrt{b^2+c^2}\right) - \frac{(a^2+b^2)^{3/2}+(b^2+c^2)^{3/2}+(c^2+a^2)^{3/2}}{3abc}.$$

Figure 3.3 Calculation of the volume averaged demagnetizing factor for a uniformly magnetized prism (along the z-axis here). The magnetostatic self-energy then writes $E = 2\pi D_z M_s^2 = 1/2 D_z J_s^2/\mu_0$ [1].

To calculate the magnetic strayfield we use the FE / BE method [44]. When a scalar potential is used, the numerical solution always underestimates [2] the true magnetostatic self-energy: the higher the energy, the more accurate is the numerical result. When the body is magnetized in-plane, the magnetic field becomes inhomogeneous only near the edges. Thus, a fine discretization along the thickness is needed in order to resolve the field correctly in this

region. Since contributions from this region to the total magnetostatic self-energy dominate for in-plane magnetized thin bodies (with a very small demagnetizing factor), their errors strongly change the value of the energy.

mesh size	*magnetostatic self-energy density* (kJ/m^3)	*magnetostatic self-energy density (difference to the theoretical value)*
A) 5 nm	24.89	-17%
B) 2.5 nm	27.83	-5%
C) 1.7 nm near edges 5 nm in the rest	28.53	-2%
theory (Fig. 3.3)	29.18	exact

Table 1 Mesh size dependency of the numerical calculation of the magnetostatic self-energy for a uniformly in-plane magnetized 75x75x5 nm^3 permalloy element (see Figs. 3.4 and 3.3).

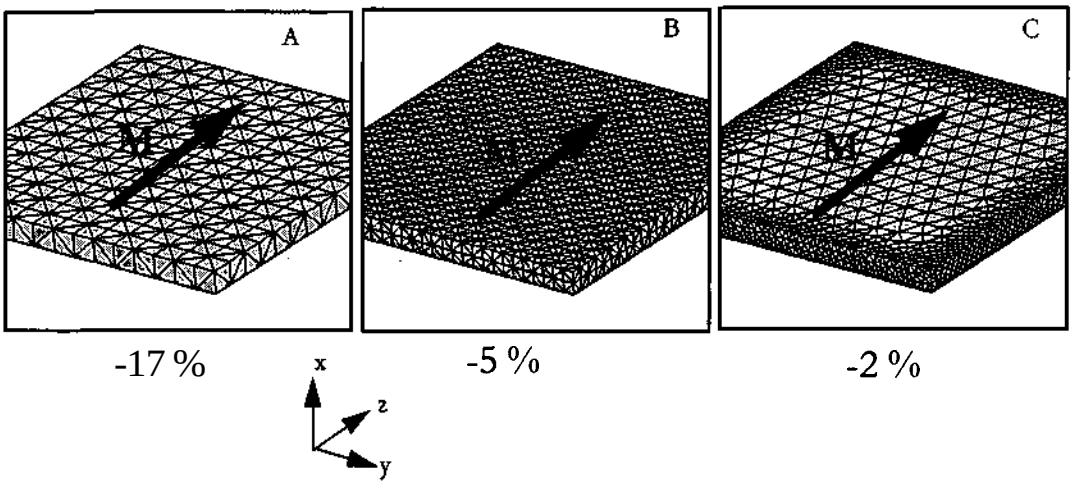

Figure 3.4 Mesh size dependency of the magnetostatic energy calculation. A 75x75x5 nm^3 permalloy platelet was magnetized uniformly in-plane along the z-axis. Three meshes are compared: A) uniform 5 nm mesh B) uniform 2.5 nm mesh C) mesh adapted to 1.7 nm near edges and 5 nm in the center. Mesh C has the highest accuracy in the strayfield calculation. The percentage values give the error in the magnetostatic energy.

3.3 Time integration

We use the CVODE package [24,25] for solving both the LLG equation and for the differential equation defined by the nudged elastic band method (4.3). The relative performance of the Adams method, the BDF method and the BDF method with preconditioning changes depending on the microstructure, material parameters, and the finite element mesh. The Adams method seems to be attractive because of the low cost per time step. In contrast to the one-step methods (e.g. Runge-Kutta) multistep methods make use of the past values of the solution. At each time step a nonlinear system of equations has to be solved. The Adams method solves the nonlinear system with functional iteration and thus requires only the evaluation of the right hand side of (2.6). However, if the problem is stiff the convergence of the functional iterations is slow. For a stiff problem it is advisable to use an implicit method such as BDF. The nonlinear system is solved using a Newton method. Normally only a few Newton steps are required. Within CVODE the linear system for each Newton-step is solved either with a direct solver or with a Krylov subspace method. Krylov subspace methods have been explored in micromagnetics by Tsiantos et al. [110,111]. The solution is approximated iteratively by a linear combination of the basis vectors of the Krylov subspace. At each iteration step one orthonormal basis vector is added which increases the subspace dimension by one. If the Krylov subspace dimension is equal to the number of unknowns the exact solution is found. For practical applications a very good approximation is obtained for a Krylov subspace dimension much smaller than the number of unknowns. The default value for the maximum Krylov subspace dimension in CVODE is 5. An additional parameter in the CVODE package is the maximum order of the time integration method. We obtained good results with a maximum order, $qu_{\max} = 2$.

For details on the finite element micromagnetics as implemented in our simulation package see [102,103].

4 THE NUDGED ELASTIC BAND METHOD

In this section a method for finding saddle points and minimum energy paths is introduced and the implementation in a finite element micromagnetics package explained. The method is based on the elastic band method which is successfully being used in chemistry for the calculation of reaction rates. The theory is explained starting from simple test cases as for example a 2D energy landscape. The method was found to be robust and fast for both simple test problems as well as for large systems such as patterned granular media.

4.1 Introduction

The thermal stability of magnetic media and magnetic storage elements becomes important with decreasing size of the magnetic structures [96]. The calculation of the thermal stability requires the estimation of transition rates between stable equilibrium states of the magnet. The calculation of transition rates needs a detailed characterization of the energy landscape along the most probable path which is taken by the system from its initial state to a final state. The energy landscapes of micromagnetic systems drastically depends on the microstructure of the magnet and may contain many local minima. Using the finite element method it is possible to represent complex geometries and grain structures. The combination of the finite element method and an algorithm for finding the minimum energy path provides a tool to calculate the energy barriers in large scale micromagnetic systems.

Berkov [11,12] calculated the transition path of interacting single domain particles by minimizing the action along the path. He showed that a direct minimization of the action may also give paths through local maxima which have to be excluded. In theoretical chemistry, path integral Monte Carlo methods are applied to calculate the rate of transitions in chemical reactions of diffusion events [31]. The Monte Carlo method is used to sample the most probable transition paths. Another family of methods for the calculation of transition paths is the elastic band method proposed by Henkelman and Jónsson [56]. Starting from an initial guess for the path which connects two local minima of the system, a highly probable path is found by moving the points along the path according to an algorithm which resembles tensioning an elastic band across a mountain. A common feature of all methods is the discrete representation of the path connecting the initial state of the system with its final state.

In micromagnetics we represent the magnetic states of a system by a set of magnetic moments. This corresponds to the magnetization at the nodes of the finite element mesh, which is used to model the geometry and grain structure of the magnet. A sequence of magnetic states can be constructed in such a way as to form a discrete representation of a path from the initial magnetization state $\mathbf{M}_i$ to the final magnetization state $\mathbf{M}_f$. The most simple case of the initial path is just a straight line interpolation in the configuration space between $\mathbf{M}_i$ and Mf. For the configuration space we use polar coordinates of dimension *2N,* where *N* is the number of magnetization vectors (nodes). An optimization algorithm is then applied until at any point along the path the gradient of the energy is only pointing along the path. This path is called minimum energy path (MEP) and means that the energy is stationary for any degree of freedom perpendicular to the path.

The method thus does not just give the saddle point, but also gives a more global view of the energy landscape, for example, if more local minima and saddle points are found along the minimum energy path. The minimum energy path typically represents the path with the greatest statistical weight. From this path statistical quantities as for example rate constants for the thermally induced magnetization reversal can be calculated. In magnetic recording applications the knowledge of rate constants is crucial since they determine thermal stability of the recorded data.

We use the finite element method to calculate *E* for complex magnetic systems. The direction components of the magnetic polarization, u_k, are interpolated by piecewise linear functions on a tetrahedral grid. The integral in (2.4) breaks into a sum of integrals over tetrahedral elements. In order to evaluate the stray field, H_s, we use a hybrid finite element / boundary element method [43]. Using the finite element method it is possible to represent irregularly shaped grains and boundary phases.

4.2 Equivalent ordinary differential equation

Henkelman and Jónsson proposed the nudged elastic band method to calculate minimum energy paths [56]. We follow this approach to evaluate transition paths in micromagnetics. An initial path is assumed which connects the initial magnetization state $\mathbf{M}_i$ = Mj with the final magnetization state $\mathbf{M}_f = \mathbf{M}_n$. A path is represented by a sequence of *n* images, $\mathbf{M}_k$, where the index *k* runs from 1 to *n.* The path is optimal, if for any image $\mathbf{M}_k$ the gradient of the energy

is only pointing along the path. Therefore the images of the optimal path have the following properly

$$(\nabla E(\mathbf{M}_k)) \times t = 0 \qquad \text{for } k = 1, \ldots. \tag{4.1}$$

Here t denotes the unit tangent vector along the path.

The optimal path can be found using an iterative scheme. In each iteration step the images are moved in a direction parallel to the negative gradient of the energy and normal to the current path. So $\mathbf{M}_k$ is moved in a direction parallel to

$$D = -\{\nabla E(\mathbf{M}_k) - (\nabla E(\mathbf{M}_k) \cdot t)t\}. \tag{4.2}$$

To keep an equal distance between successive images, Henkelman and Jónsson [56] introduce a spring force in addition to D (see section 4.3). E and co-workers apply a reparametrization after a few iterations to ensure equal distance between the images [38,83]. We obtained good results without the spring force, using a variable order, variable time step method to relax the initial path towards a minimum energy path. Details on using the spring force are given in section 4.3. We represent the path finding scheme with a system of ordinary differential equations

$$\frac{\partial \mathbf{M}_k}{\partial t} = D(\mathbf{M}_k) \qquad \text{for } k = 2, n-1. \tag{4.3}$$

We solve (4.3) numerically (see section 4.3), using the software package CVODE [25]. In this package we can choose between the implicit BDF (backward differentiation scheme) scheme and the explicit Adams scheme. The time in (4.3) is introduced for numerical convenience and has no physical meaning. It turned out to be important for the efficiency of the time integration to rescale the right hand side of (4.3). We divide the right hand side by the average volume assigned to one finite element node.

$$D(\mathbf{M}_k) \to D(\mathbf{M}_k)/V_{average} \qquad V_{average} = \frac{\text{total mesh volume}}{\text{number of mesh nodes}} \tag{4.4}$$

This ensures that the magnitude of D always keeps the same order of magnitude and becomes independent of the mesh.

We use polar coordinates to represent the magnetization configuration of an image, $\mathbf{M_k}$. The dimension of the configuration space is *2N*, where N is the number of nodes of the finite element mesh. This gives a total number of variables of $2N \times (n-2)$ in equation (4.3), as the initial and the final magnetization state do not move. The direction *D* is calculated in the con-

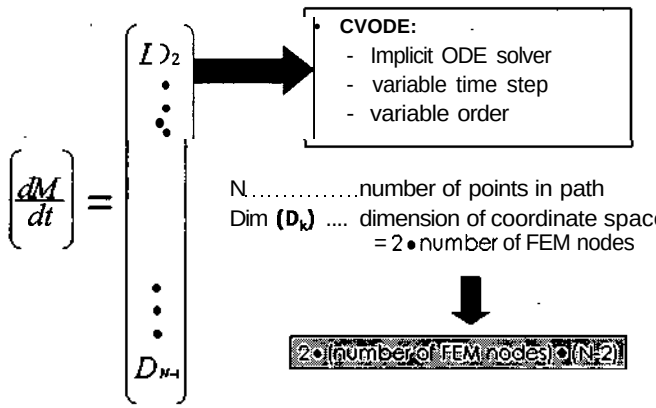

Figure 4.1 Schematic view of the right hand side of equation 4.3 with the total number of unknowns. The equation is solved implicit by a BDF (backward differentiation) scheme using the differential equation solver package CVODE [25].

figuration space. In order to calculate the gradient of the energy in polar coordinates, we use the following equations [100]:

$$\frac{\partial E}{\partial \vartheta_i} = \frac{\partial E}{\partial u_{1,i}}\frac{\partial u_{1,i}}{\partial \vartheta_i} + \frac{\partial E}{\partial u_{2,i}}\frac{\partial u_{2,i}}{\partial \vartheta_i} + \frac{\partial E}{\partial u_{3,i}}\frac{\partial u_{3,i}}{\partial \vartheta_i}, \tag{4.5}$$

$$\frac{\partial E}{\partial \varphi_i} = \frac{\partial E}{\partial u_{1,i}}\frac{\partial u_{1,i}}{\partial \varphi_i} + \frac{\partial E}{\partial u_{2,i}}\frac{\partial u_{2,i}}{\partial \varphi_i} + \frac{\partial E}{\partial u_{3,i}}\frac{\partial u_{3,i}}{\partial \varphi_i}, \tag{4.6}$$

where i runs over all nodes of the finite element mesh. This transforms the energy gradient from cartesian coordinates to polar coordinates. Care has to be taken, calculating the local tangent at an image k. The single use of either a forward difference approximation, backward difference approximation, or a central difference approximation develops kinks in the path [56]. The kinks prevent the string from converging to the minimum energy path. The optimal choice of the appropriate difference approximation depends on the energy difference between successive magnetization states. In a first approach we use forward differences

climbing up a hill, backward differences going down a hill, and central differences at energy maxima and minima:

$$t = \frac{\mathbf{M}_{k+1} - \mathbf{M}_k}{|\mathbf{M}_{k+1} - \mathbf{M}_k|} \qquad \text{if } E(\mathbf{M}_{k-1}) < E(\mathbf{M}_k) < E_t(\mathbf{M}_{k+1}), \tag{4.7}$$

$$t = \frac{\mathbf{M}_k - \mathbf{M}_{k-1}}{|\mathbf{M}_k - \mathbf{M}_{k-1}|} \qquad \text{if } E(\mathbf{M}_{k-1}) > E(\mathbf{M}_k) > E(\mathbf{M}_{k+1}), \tag{4.8}$$

$$t = \frac{\mathrm{ML}_{k+1} - \mathbf{M}_{k-1}}{|\mathbf{M}_{k+1} - \mathbf{M}_{k-1}|} \qquad \text{if } E(\mathbf{M}_{k-1}) < E(\mathbf{M}_k) > E(\mathbf{M}_{k+1}) \text{ or}$$

$$E(\mathbf{M}_{k-1}) > E(\mathbf{M}_k) < E(\mathbf{M}_{k+1}). \tag{4.9}$$

This prevents the formation of kinks. A detailed analysis on this topic and the motivation for this choice of the tangent can be found in the work of Henkelman and Jónsson [56]. In short it is motivated by another method for the calculation of the MEP if the saddle point is already known. Starting from the saddle point the system is displaced by some small increment and the energy minimized, keeping the distance from the saddle point fixed. This gives one more point of the MEP. Then the system is displaced again starting from this new state and the energy is minimized while keeping the distance to the previous state fixed. By repeating this procedure we obtain the MEP and at some point we end in a local minimum of the system. But important is, that the MEP can be found by starting at the saddle point and follow forces lines down the energy landscape. The other way around does not work. If following forces lines up the hill starting from an energy minimum, it will mostly not pass the saddle point but somewhere else. This motivates the choice for the tangent to be determined by the higher energy neighboring image (see equations (4.7)-(4.9)). However in some cases numerical problems with the time integration occurred in certain situations. These problems get eliminated by using the slightly modified "smooth" version of these equations [56]. We still use forward differences climbing up a hill and backward differences going down a hill:

$$\boldsymbol{\tau}_i^+ = \mathbf{M}_{k+1} - \mathbf{M}_k \quad \text{and} \quad \mathrm{T}; = \mathbf{M}_k - \mathbf{M}_{k-1} \tag{4.10}$$

$$\boldsymbol{\tau}_i = \boldsymbol{\tau}_i^+ \qquad \text{if } E(\mathbf{M}_{k-1}) < E(\mathbf{M}_k) < E_t(\mathbf{M}_{k+1}), \tag{4.11}$$

$$\mathrm{T},. = \boldsymbol{\tau}_i^- \qquad \text{if } E(\mathbf{M}_{k-1}) > E(\mathbf{M}_k) > E(\mathbf{M}_{k+1}) \tag{4.12}$$

But instead of using central differences at maxima and minima we use a formulation which smoothly switches from (4.11) to (4.12):

$$\tau_i = \begin{cases} \tau_i^+ \Delta E_i^{max} + \tau_i^- \Delta E_i^{min} & \text{if} \quad E_{i+1} > E_{i-1} \\ \tau_i^+ \Delta E_i^{min} + \tau_i^- \Delta E_i^{max} & \text{if} \quad E_{i+1} < E_{i-1} \end{cases} \quad \text{and}$$

$$E_{i-1} < E_i > E_{i+1} \quad \text{or} \quad E_{i-1} > E_i < E_{i+1} \quad . \tag{4.13}$$

where

$$\begin{aligned} \Delta E_i^{max} &= max(|E_{i+1} - E_i|, |E_{i-1} - E_i|) \\ \Delta E_i^{min} &= min(|E_{i+1} - E_i|, |E_{i-1} - E_i|) \end{aligned} \tag{4.14}$$

In the end the tangent still needs to be normalized. This formulation differs only at the extrema (see (4.13)) along the MEP from the simpler formulation in equations (4.7)-(4.9). At the extrema the formulas contains weight factors. This weighted formulation serves to smoothly switch between the two possible tangents τ_+ and T_. Otherwise there is an abrupt change in the tangent as one image becomes higher in the energy than another and this was the reason for the numerical problems that sometimes occurred with the simpler formulation.

4.3 Spring force and definition of a length

In the first calculations no spring forces were used. Here the images tend to move towards the endpoints and local minima of the path giving low resolution near saddle points and high resolution near energy minima. This problem is known as "sliding-down" [58] and can be solved by introducing spring forces between the images which make them stay equally spaced. First a definition of the "length" (norm) is needed that will be used to calculate the distances between the images. In a first approach we just used the conventional L2-norm in the configuration space (polar coordinates) since we need this norm for the geometrical vector operations and normalization of the local tangent (equations (4.7)-(4.9)) anyway. However there is some unphysical distance when two images have the same azimuth angle of $0, \pi, 2\pi$ etc. and different polar angles. According to the L^2-norm in polar coordinates these points are sepa-

rated. However, all these points represent the same magnetization state in cartesian coordinates. This problem is solved by an improved way for the calculation of the distance:

$$\|M_{i+1} - M_i\| = \sqrt{\frac{\sum_{k=1}^{N} \alpha_k^2 V_k}{\sum_{k=1}^{N} V_k}} \qquad \text{N...number of FEM nodes} \tag{4.15}$$

where

$$\alpha_k = acos\left(\frac{m_{i+1}^k \cdot m_i^k}{|m_{i+1}^k| \cdot |m_i^k|}\right) \tag{4.16}$$

is the angle between the spin m_{i+1}^k on the finite element node k in image M_{i+1} and the spin m_i^k on the node k in the image M_i. V_k is the volume (see figure 3.2) which corresponds to the spin on the node k such that

$$\sum_k V_k = V \quad \text{and} \quad V_i \cap V_j = 0 \quad \text{for} \quad i \neq j \tag{4.17}$$

Here V is the total volume of the finite element mesh. The weighting by the volume V_k which corresponds to the node k of the finite element mesh serves to make the length definition independent of the number of finite elements used but also independent of the way how a particular magnet is meshed (e.g. adapted mesh). We obtained good results with this definition of the length. For a columnar CoCr grain (see section 4.9.3) now the total length of the initial path becomes exactly π, independent on how we mesh the particle. But note that the conventional L^2-norm in polar coordinates is still needed for all geometrical operations in the nudged elastic band (NEB) method (normalization of the tangent, calculation of the normal component of the gradient).

Using the norm definition in equation 4.15 we define the spring force on the image i as

$$F_i^S = k(\|M_{i+1} - M_i\| - \|M_i - M_{i-1}\|)\frac{\tau_i}{|\tau_i|} \qquad k\text{...spring constant} \tag{4.18}$$

Note that here only the component of the spring force parallel to the path is taken. At the same time only the normal (perpendicular) component of the true force (energy gradient) is used in *D*. This force projection is what is referred as "nudging". Without this projection of the forces the "corner-cutting" problem would have occurred. With the introduction of the spring force the total force becomes:

$$\boldsymbol{F}_i = \boldsymbol{F}_i^s - \nabla E(\boldsymbol{M}_i)_{\perp} = \boldsymbol{F}_i^s + D \tag{4.19}$$

Here *D* is defined in (4.2).

One problem is the choice of the strength of the spring constant *k*. The optimal value for *k* depends on the number of images used, on the number of finite elements and on the size of the model. It is difficult to give a general rule for the value of the spring constant. It should be strong enough to prevent images to fall down into the energy minima, but not to strong as to dominate by orders of magnitude in equation (4.19). However it is usually not very critical and can be varied over several orders of magnitude without losing speed with the time integration CVODE. It depends on the accuracy of the solution that we want to obtain with the time integration. The accuracy of the solution is an input parameter of the CVODE package. If 5 digits of accuracy is chosen, then a difference of 5 orders of magnitude in the forces has the consequence that the smaller force is in the order of the rounding errors of the larger force. Thus, the weaker force gets completely suppressed and wrong results will be obtained.

4.4 Choosing the initial path

At first an initial path must be chosen. There is variety of ways to do this. In most cases we found that the path which is just the linear interpolation between two images (two stable states of the system) gives good results. Another way is to start from a path that is obtained from a hysteresis calculation. One can also generate one completely random image. Then an initial path can be generated using the two stable states and this random state in between.

4.5 Criterion for stopping

One must also define when the simulation is to be stopped, that means a parameter which defines how accurate the MEP is. In a first approach we used the maximum value of the force

acting on the nodes. A better stopping criterion comes directly from the time integration scheme. The simulations stops when

$$max_{i,j}\left(\frac{\left|m_i^k(t) - m_i^k(t+\Delta t)\right|}{\Delta_t}\right) \leq tol. \tag{4.20}$$

tol is the variable stopping parameter. The maximum change of a component of the solution vector (all images) in one step of the time integration must drop below this value. Care must be taken when choosing the value for stopping. An example where this is critical is shown in Fig. 4.2. The minimum energy path was calculated for the thermal reversal between two S-states in a $100 \cdot 100 \cdot 5\ nm^3$ permalloy platelet. Fig. 4.2 shows the energy along the path as the optimization proceeds. It seems like if the red curve minimum energy path and equilibrium has been reached. If we chose a stricter stopping criterion (smaller *tot)* the optimization continues until the correct minimum energy path (green curve) is reached.

One way of testing if really an minimum energy path was calculated is to perform Langevin dynamic simulations starting from the prior calculated saddle point. If it is really a saddle point we should access both sides of the saddles ending in either one of the valleys, when the simulations repeated several times.

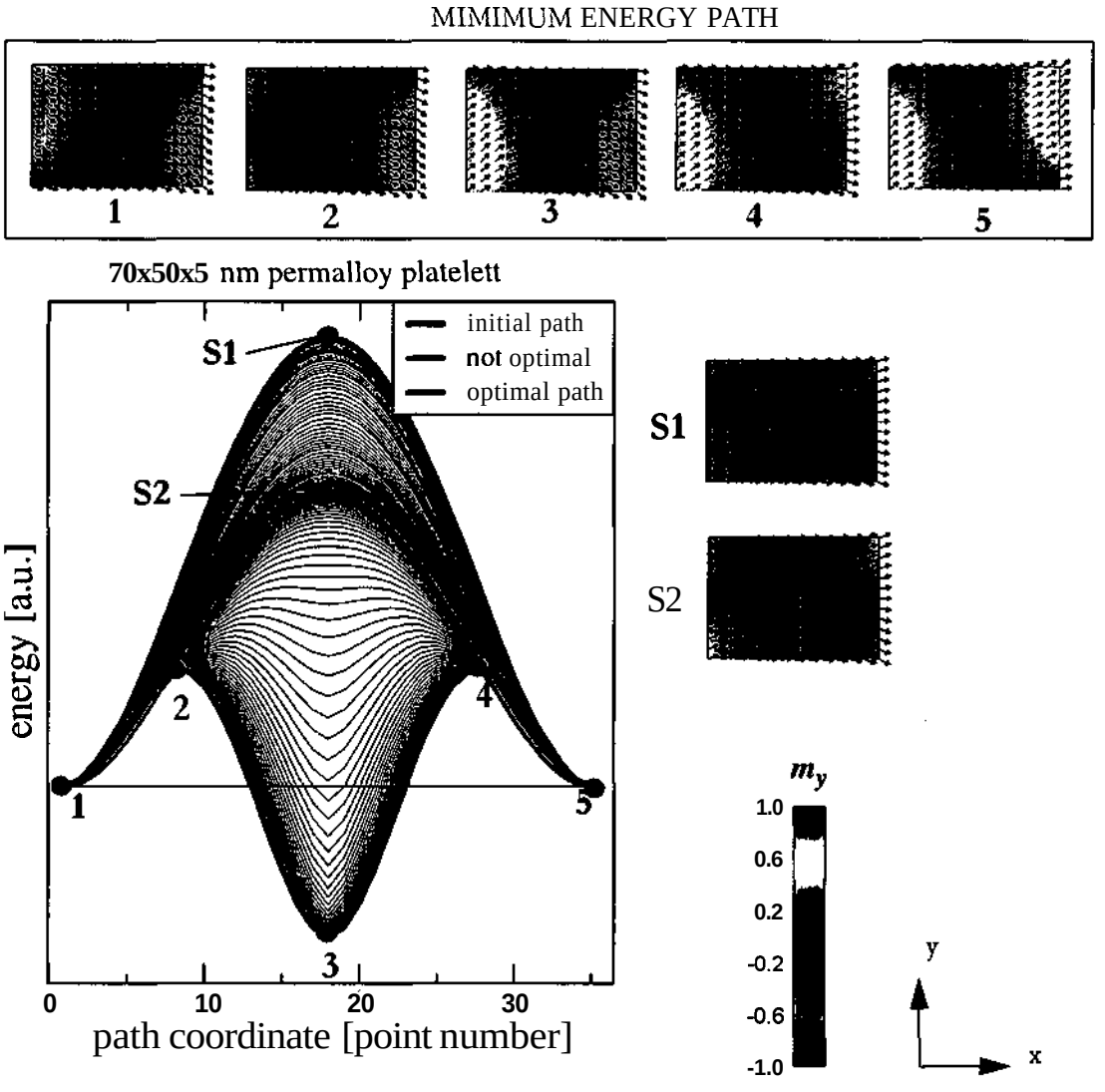

Figure 4.2 Energy along the path during the nudged elastic band simulation of the thermal reversal between two S-states in a 100 • 100 • 5 nm³ permalloy platelet. Care has to be taken when interpreting the results. It seems like the red curve (passing S2) has reached equilibrium. But if the stopping criterion for the simulation is strict, the optimization continues until the correct minimum energy path (green curve, passing "3") is reached.

4.6 Time integration

To solve (4.3) we use the backward differentiation scheme (BDF). This worked well for all applied problems and was found to be quite fast and robust against the introduction of spring forces. Compared to the explicit Adams method, the BDF method is about 10-50 times faster which is shown in figure 4.3. We compared it for the energy barrier computation of an elliptical MRAM element meshed with an adapted finite element mesh with 18 000 elements (6600 nodes).

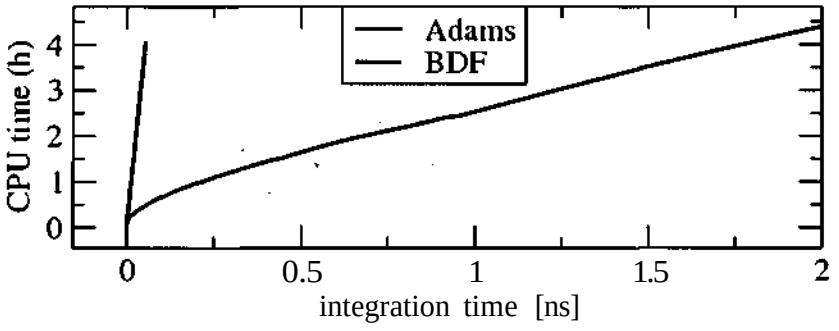

Figure 4.3 Comparison of the CPU time for the calculation of a minimum energy path of an elliptical MRAM ($1000 \cdot 400 \cdot 4$ nm^3). The backward differentiation scheme (BDF) is more than one order of magnitude faster as compared to the explicit Adams scheme.

In dynamic simulations it is important to keep a good accuracy during the integration since errors can result in different solutions after a certain time of integration. In the elastic band method this is less important since only the solution ("minimum energy path") that we obtain at the end counts and not how we get there. The time integration is only needed to get to this "end point". So the way to go there is not of much interest except that it should be one which minimizes the spent CPU time. This means that we drive the integration at the limit of numerical stability in order to maximize the computation speed. If desired we can still restart a calculation with an increased accuracy starting from the path obtained with less accuracy.

As an alternative to the time integration of (4.3) one could reformulate the problem and use a constrained energy minimization method. The minimizing functional is then simply the sum of the energies of all images along the path:

$$F(\boldsymbol{M}_1, \boldsymbol{M}_2, \ldots, \boldsymbol{M}_N) = \sum_{i=2}^{N-1} E_{Gibbs}(\boldsymbol{M}_i) \tag{4.21}$$

and the constraint is the equal spacing of the images:

$$\|\boldsymbol{M}_{i+1} - \boldsymbol{M}_i\| = \|\boldsymbol{M}_i - \boldsymbol{M}_{i-1}\| \text{ for } i \in \{2 \ldots N-1\} \tag{4.22}$$

A simpler method than the constrained minimization would be to add all spring energies to the functional and minimize this total without the need of a constraint:

$$F(\boldsymbol{M}_1, \boldsymbol{M}_2, \ldots, \boldsymbol{M}_N) = \sum_{i=2}^{N-1} E_{Gibbs}(\boldsymbol{M}_i) + \sum_{i=2}^{N-1} \frac{k}{2}(\|\boldsymbol{M}_{i+1} - \boldsymbol{M}_i\| + \|\boldsymbol{M}_i - \boldsymbol{M}_{i-1}\|)^2 \tag{4.23}$$

Both approaches could lead to a further speed up as compared to the time integration. In the framework of this thesis we did not test these ideas, thus they should be treated as a suggestion for improvement but without a guarantee for success.

4.7 Spline interpolation

To increase the accuracy of the saddle point estimation we interpolate between the images of the obtained MEP. In addition to the energy of the images, the force along the band provides important information and is incorporated into the interpolation. By including the force, the presence of intermediate local energy minima can often be extracted from bands with very few images. The interpolation can be done with piecewise cubic polynomials for each segment $[\boldsymbol{M}_i, \boldsymbol{M}_{i+1}]$. The four parameters needed for the polynomial are chosen to ensure continuity in energy and force (tangential component of the energy gradient) at both ends. With the polynomial as $f(x) = a_i x^3 + b_i x^2 + c_i x + d_i$ the four parameters are obtained from the four equations

$$f(x|_{\boldsymbol{M}_i}) = E_i \quad \text{and} \quad f(x|_{\boldsymbol{M}_{i+1}}) = E_{i+1} \tag{4.24}$$

$$\frac{df}{dx}(x|_{\boldsymbol{M}_i}) = F_i \quad \text{and} \quad \frac{df}{dx}(x|_{\boldsymbol{M}_{i+1}}) = F_{i+1} \tag{4.25}$$

The parameters then become

$$a_i = \frac{2(E_i - E_{i+1})}{R^3} - \frac{F_i + F_{i+1}}{R^2} \tag{4.26}$$

$$b_i = \frac{3(E_{i+1} - E_i)}{R^2} + \frac{2F_i + F_{i+1}}{R} \tag{4.27}$$

$$c_i = -F_i \tag{4.28}$$

$$d_i = E_i \tag{4.29}$$

Here x denotes the arclength, E_i and E_{i+1} the energy, and F_i and F_{i+1} the forces along the path (=tangential component of the energy gradient). R is the distance $R = |x_{i+1} - x_i|_M$ between the two images. A nice overview about interpolation of curves with an interactive interface is found in [80]. We demonstrate the interpolation with two

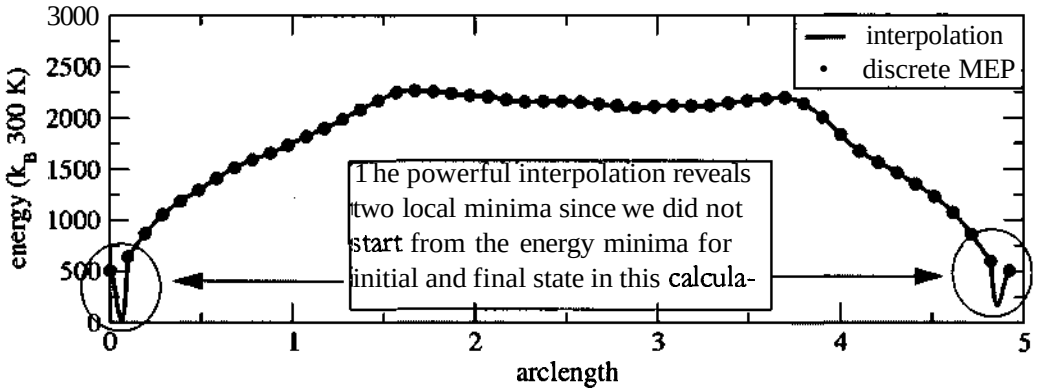

Figure 4.4 Discrete minimum energy path with 50 images and the interpolated path according to equations (4.26)-(4.29). The example shows the minimum energy path for a 70*70*21 nm^3 patterned element with 49 grains. The initial and final images were not completely equilibrated here. Thus, these images were not yet located in the energy minima. Therefor the interpolated curve predicts the local minima between the first and the second image, and the last and last but one image.

examples. In the first example we calculate the minimum energy path for a granular patterned element. In order to test the interpolation we choose the initial and final state to be close to the energy minimum, but not exactly in the minimum. The powerful interpolation method reveals the presence of two local minima very close to the initial and final state (see figure 4.4). These minima are also obtained when just the number of images is increased to 150. In a second example we calculate the minimum energy path for the reversal of a vortex core in a

small softmagnetic disc. An external field just below the switching field was applied in the opposite direction of the vortex core orientation. In this case the final state where the vortex is reversed has much lower energy (see figure 4.5). The energy barrier is small since the field strength is close to the zero temperature switching field. As result the image resolution is very low at the region of interest, the saddle point Here the interpolation increases the accuracy of the saddle point energy (figure 4.5). Without interpolation the energy barrier would have been strongly underestimated here.

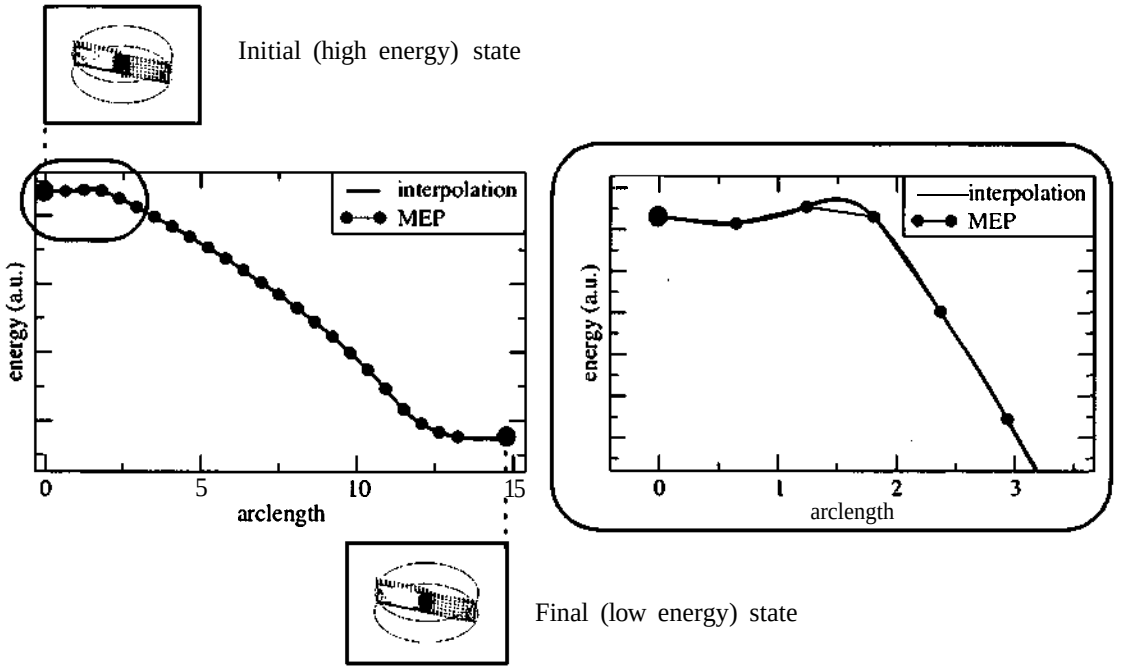

Figure 4.5 The interpolation is important when the resolution of the images is low at the location of the saddle. Without interpolation the saddle point and the energy barrier would have been underestimated here. The example here shows the MEP for the reversal of the vortex core in a softmagnetic disk. The initial and final state have different energies since an external field was applied. In the final state the vortex core is reversed and points in the field direction. The energy is thus lower. For details on Bloch points see section 6.

4.8 Climbing image NEB method

As an alternative to the interpolation we also implemented the climbing image algorithm (CINEB) [57] into our code. This requires only a small modification and guarantees a rigorous convergence towards the saddle point. After some iterations of the regular NEB method, the images which are local maxima are identified. The force on these images is then given by

$$D = -\{\nabla E(\mathbf{M}_k) - 2(\nabla E(\mathbf{M}_k) \cdot t)t\} \tag{4.30}$$

This means that we keep the normal component of the energy gradient but invert the tangential component. In addition these images don't get affected by the spring forces. Qualitatively, the images now move up the energy landscape along the nudged elastic band. The task of the other images is only to define that one degree of freedom along which the energy maximization is performed. Using this method it is possible to decrease the number of images but still maintain a rigid convergence towards the saddle point(s). In simple cases good results are obtained even with as few as 5 images.

The results obtained with the CINEB method agree very well with the results from the interpolation. As an example we calculate the energy barrier for the reversal of a vortex core in a small softmagnetic disc. In figure 4.5 the third image now moves exactly to the top (local maximum) of the interpolated red curve when the CINEB method is switched on.

4.9 Examples

4.9.1 Interacting single domain particles

In order to test our path finding method we start with a simple test case. We study two single domain particles with saturation polarization J_s, uniaxial anisotropy (K_1) and identical volumes (V). The line connecting the particles is parallel to the uniaxial anisotropy direction. The distance between the particles is R. In polar coordinates the magnetization of this two particle system is described by four angles ($\theta_1, \phi_1, \theta_2, \phi_2$). Although there are four independent variables only cases where the magnetizations of the two particles are in the same plane describe equilibrium states. It is therefore sufficient to study cases where only θ_1 and θ_2 vary. The total energy then becomes [22]

$$E/(K_1 V) = \sin^2\theta_1 + \sin^2\theta_2 + k_{\mathrm{int}}[\sin\theta_1 \sin\theta_2 - 2\cos\theta_1 \cos\theta_2] \tag{4.31}$$

$$k_{\mathrm{int}} = J_s^2 V/(2\mu_0 R^3 K) \quad \text{reduced interaction constant} \tag{4.32}$$

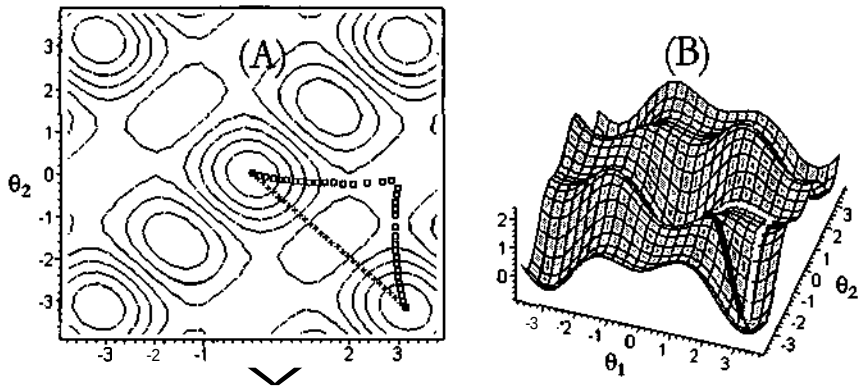

Figure 1: (A) Contour plot with initial path (crosses) and minimum energy path (boxes). (B) energy surface with initial path (black) and minimum energy path (white) for a system of two interacting magnetic particles. k_{int}=0.2

Thus, ∇E can be calculated analytically in this case. With this reduction to two dimensions the energy landscape with paths can be plotted which helps us to verify our method and results. Figure 1 shows one possible case of the energy landscape where no external field is applied. In the initial state the magnetization of both particles is parallel ("up up"). We then connect the initial state with the final state ("down down") with a straight line. This initial path describes the coherent rotation of the magnetizations where the two magnetic moments rotate from the initial state to the final state in opposite direction (asymmetric fanning $\delta\theta_1 = -\delta\theta_2$). The energy landscape with the initial path and the minimum energy path are shown in figure 1. The initial path (black line) moves over the top of the hill. Applying the algorithm described in section 2 we obtain a minimum energy path as given by the white line in figure 1. In the minimum energy path one particle starts rotating. The system passes the first saddle point and reaches a local minimum. The moments are antiparallel. Then the second particle rotates. The system crosses a second saddle point and ends in the final state where the magnetic moments are parallel. It becomes obvious from the energy landscape that there is a second possible minimum energy path which can be reached from the same initial path. Both paths describe the same process. The particles start to switch in the opposite order in the two paths. Figure 4.6 shows the energy as a function of the arclength of the initial path and the minimum energy path. During the solution of equation (4.3), the path relaxes to the minimum

energy path. The path becomes longer and the maximum develops into two saddle points and a local minimum in between.

Testing more complex problems with the 2D energy landscape, we found that the tangent estimate is crucial for the convergence of the method [56] and has to be evaluated as described in section 4.2.

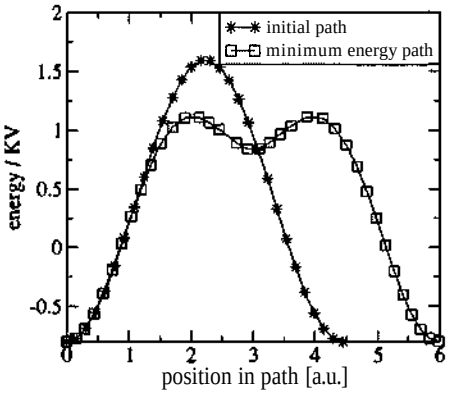

Figure 4.6 Energy along the initial path and the minimum energy path for a system of two interacting magnetic moments.

4.9.2 Small quadratic magnet

As another simple problem, we study a small quadratic thin magnet of CoCr which has high uniaxial anisotropy (K_1 = 0.3MJ/m^3, J_s = 0.5 T, A - 10 pJ/m). The particle size is 5 nm x 5 nm x 1 nm and is meshed with a finite element grid with 16 nodes. The particle lies in the yz-plane (see figure 2). The dimension of the configuration space is 32 and a visualization of the energy landscape is no more possible. The magnetocrystalline anisotropy axis, a, is parallel to one long edge. In the initial state the magnetization is parallel to the easy axis and therefore in a local minimum. In the final state the magnetization has opposite direction to the initial state and is also in a local minimum. For testing our method we assume an initial path in which the magnetization rotates coherently out of the plane. In the minimum energy path the magnetization still rotates coherently since the particle is small and thus behaves like a single

domain particle. However, the rotation now takes place in-plane since here the magnetostatic contribution to the total energy is lowest (see figure 2).

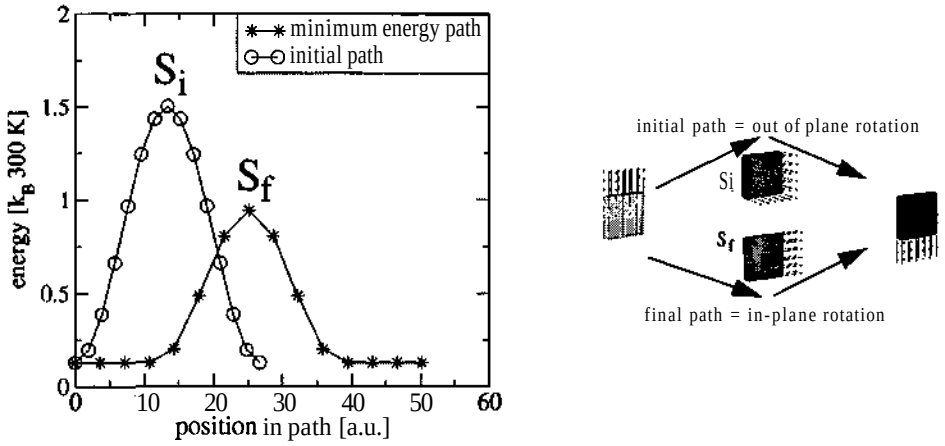

Figure 2 Energy along the initial path and minimum energy path with illustration of the magnetization along the paths. The particle has a size of *5x5x1* nm^3 and high uniaxial anisotropy parallel to the edge. In the minimum energy path the magnetization reverses by rotation in-plane since this lowers the magnetostatic energy. (S_i....energy barrier of initial path, S_f.....energy barrier of minimum energy path = saddle point.)

4.9.3 Elongated magnetic grain

A more complicated problem is one elongated magnetic particle with uniaxial magneto-crystalline anisotropy parallel to the long axis. This model represents one magnetic grain in a perpendicular recording medium such as CoCr [101]. The grain diameter is 13 nm. As before we start with a straight line in polar coordinates for the initial path. The angle of the magnetization and the long axis of the particle increases by a constant step from one image to the next. This path represents the coherent rotation of the magnetization from the initial to the final state (see figure 4.7).

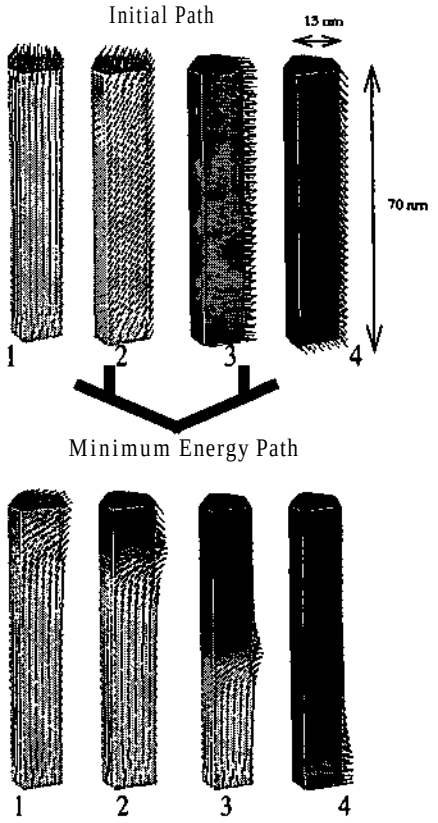

Figure 4.7 Magnetization states along the initial path and the minimum energy path for an elongated CoCr particle with the easy parallel to the long axis. Grey: magnetization up; black: magnetization down.

It was found that above a certain critical length, l_c, of the particle the minimum energy path changes from coherent rotation to nucleation followed by domain wall motion until the whole magnetization is reversed (see figure 4.7). This can also be understood by an analytical estimate. In the following F denotes the area of the basal plane of the elongated grain. The domain wall energy is $E_{wall} = 4F\sqrt{AK_1}$ while the energy for coherent rotation is $E_{rot} = K_1 V$. Now if the particle length is increased only V increases while F remains constant. Thus, there will be a critical length where $E_{wall} < E_{rot}$ and the nucleation and expansion of a domain wall becomes energetically favorable. With A = 10 pJ/m and K = 300 kJ/m^3 the critical length becomes $l_{crit} = \frac{(4F\sqrt{AK_1})^2}{K_1 l_{ex}^3}$ =19 nm. l_{ex} denotes the length of the particle. This agrees very well with the numerical results. Figure 4.8 shows the maximum exchange energy and the effective volume for the thermal reversal of an elongated CoCr particle as a function of the column

length. The diameter is 13 nm. Above a size of 20 nm the reversal mode becomes inhomogeneous. Below 20 nm the maximum exchange energy is almost zero. Here the particle reverses by coherent rotation. Above 40 nm the particle is large enough to form a full domain wall. Increasing the length further does not change the maximum exchange energy any more. Once the wall is formed it only moves through the particle. The same is true for the energy barrier, here expressed as an effective switching volume. Above 40 nm the effective volume V_{eff} saturates. It is therefore clear that an further increase of the column length of the grains does not increase the thermal stability in perpendicular recording material.

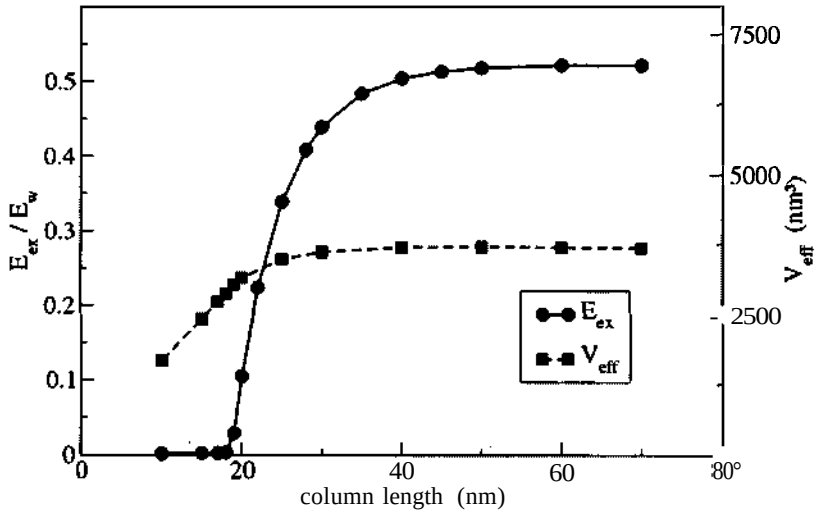

Figure 4.8 Maximum exchange energy and effective volume for the thermal reversal of an elongated CoCr particle as a function of the column length. The diameter is 13 nm. Above a si2e of 20 nm the reversal mode becomes inhomogeneous. Above ~50 nm column length, the size is large enough to form a full domain wall. The maximum exchange energy saturates as function of the length and takes the value of a domain wall exchange energy.

Figure 4.7 shows images along the initial path and the minimum energy path for a particle with a length $l > l_c$. Clearly, the algorithm detects the minimum energy path, which is given by the nucleation of a reversed domain at one end of the particle. The wall moves through the particle and the reversed domain expands. A nucleation of reversed domains at both ends will require twice the wall energy, E_{wall}, and this is no minimum energy path. Figure 4.9 shows the energy as a function of the arclength along the initial path and the minimum energy path. The

energy increases as the reversed domain is formed and remains constant during the motion of the domain wall.

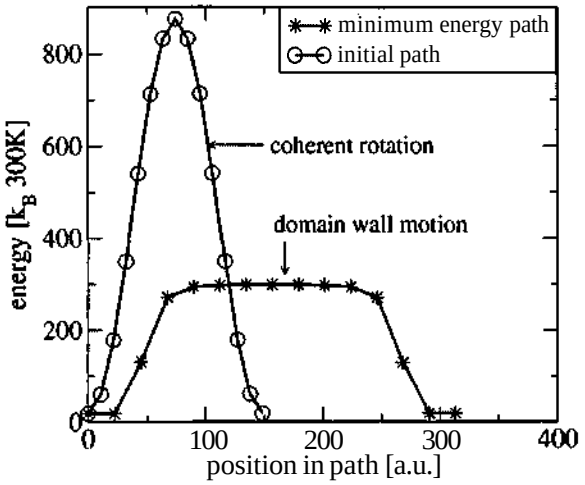

Figure 4.9 Energy along the initial path and the minimum energy path for an elongated CoCr particle with the easy axis parallel to the long axis. In the minimum energy path the magnetization reverses by nucleation followed by domain wall motion.

Hermann Forster and coworkers investigated this problem in detail [41], focusing on "Energy barriers and effective thermal reversal volume in columnar grains" [42]. For particles larger than the exchange length these barriers represent non-uniform paths between the two approximately uniform equilibrium states. Both the zero field energy barrier and the intrinsic switching field were determined over a wide range of particle exchange and magnetocrystalline anisotropy parameters. Besides the above mentioned path which involves a Bloch type domain wall motion, also vortex nucleations can occur when the anisotropy is smaller (figure 4.10). Using the form of the energy barrier for a uniformly reversing particle an effective reversal volume was determined. This volume decreased with both increasing anisotropy and decreasing exchange. A simple model [42] semi-quantitatively explained these effects corresponding to reversal by end nucleation of a cubic region and a domain wall.

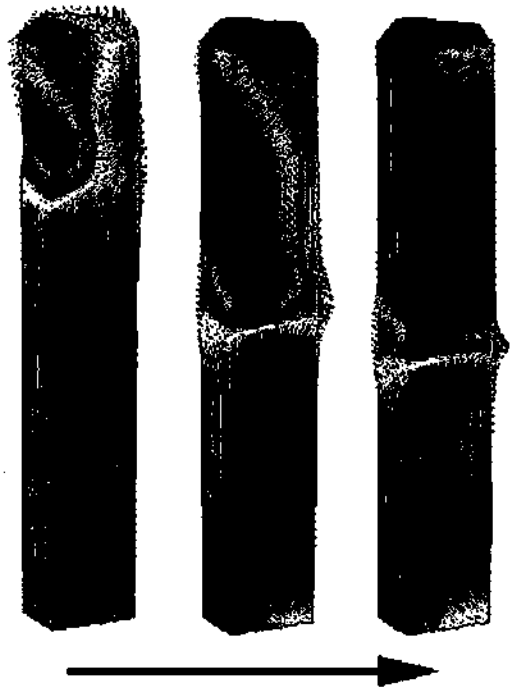

Figure 4.10 [41] Minimum energy path for an elongated particle with zero anisotropy. A=10 pJ/m, J_s=0.5 T. The reversal starts with the nucleation of a vortex on one end. red: magnetization up, blue: magnetization down. The diameter of the particle is ~13 nm, the height is 70 nm.

4.9.4 Patterned granular media

Patterned media [84] show great potential for future ultra-high density magnetic recording. In patterned media, each discrete element is exchange isolated from other elements, but inside each element polycrystalline grains are strongly exchange-coupled, behaving more like a larger single magnetic grain.

We apply the path method to one island of such patterned media. The edge length is 70 nm, the grain diameter is about 10 nm and the film thickness is 2 nm. The island consists of 49 grains. The grains are in direct contact and perfectly exchange coupled. The easy axes of the grains are perpendicular to the film plane with a random deviation of the direction from the plane normal within a cone of about 8° for each grain.

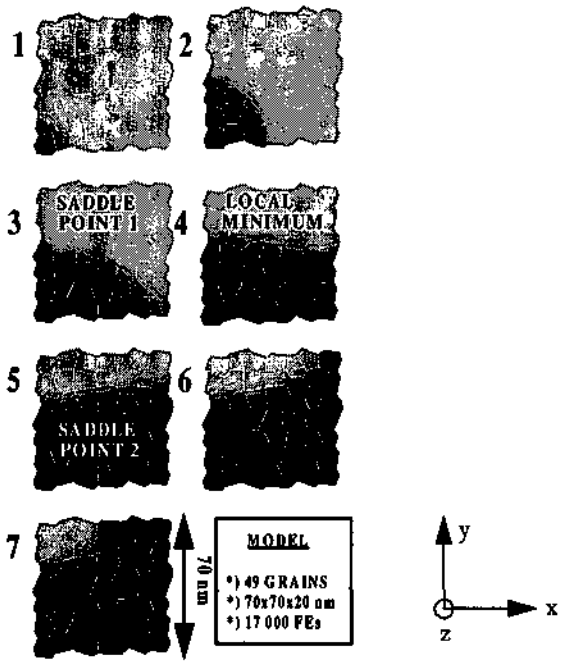

Figure 4.11 Magnetization states along the initial path and the minimum energy path for an island of a patterned CoCrPt media with granular structure. The easy axis is perpendicular to the plane. The color code corresponds to the z-component of the magnetization. bkck: $M_z = 1$, grey: $M_z = -1$

Again we start with the coherent rotation for the initial path. The minimum energy path is shown in figure 4.11. The reversal starts with a nucleation in one corner. The domain expands and the length of the domain wall increases. At the first saddle the length of the domain wall reaches a maximum. A minimum state is also found where about half of the magnetization is reversed. This two domain state has a straight (short) domain wall (see figure 4.11) which reduces the total wall energy. In addition, the two domain state is magnetostatically favorable. Therefore the two-domain state is a local energy minimum. Figure 4.12 shows the energy as a function of the arclength along the initial and the minimum energy path. The energy barrier for crossing the second saddle from the local minimum (two domain state) is about 200 $k_B T$, for T = 300 K. Thus, the intermediate two domain state is quite stable.

The high energy barriers between the initial and the final state are due to the perfect coupling between the grains. As the grains cannot reverse independently, the energy barrier is much larger than $K_1 V$, where V is the average grain volume. Further investigations of the

effect of the intergrain exchange constant on the minimum energy path showed that a reduction of the intergrain exchange constant reduces the energy barrier. Below a certain critical value the reversal mode changes from a collective mode to a reversal mode where the grains reverse individually or in smaller clusters. This leads to a loss in the total energy barrier. For more details see section 5.

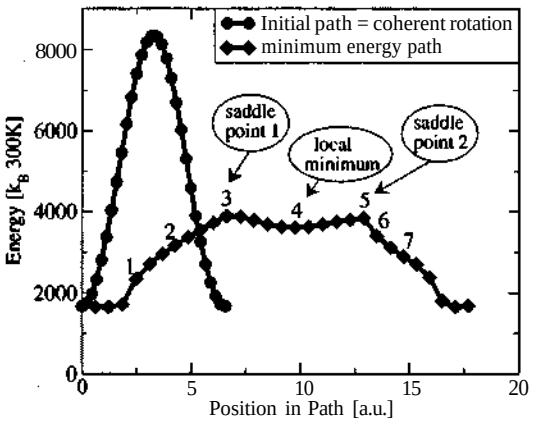

Figure 4.12 Energy along the initial path and the minimum energy path for a element of a patterned CoCrPt media with granular structure. The easy axis is perpendicular to the plane.

4.10 A comment

One problem is also the interpretation of the minimum energy path. Imagine a path connecting two equivalent minima with a metastable state in between but where the two saddle points have different height. An example is a system of two antiferromagnetically coupled grains where the grains have different volumes. The minimum energy path is shown in Fig. 4.13. The magnetization reverses in two steps, passing two energy barriers. Since the problem is symmetric (both minima have same energy when no external field are present) we can think of both processes: A) coming from the right side in Fig. 4.13. and crossing the larger barrier first or B) coming from the left side in Fig. 4.13. and first cross the smaller barrier. However, for the statistical quantities as transition rates between the minima only the larger energy barrier is important due to the exponential dependence of the transition rate on the energy barrier height Thus, both processes should give the same transition rate.

The minimum energy path represents a highly probable way trough the energy landscape for thermally assisted magnetization reversal. Thermal fluctuations can drive the system to

higher energies. However once the barrier is passed thermal activation is no more needed to proceed in the motion, and indeed the downhill parts are mainly dominated by precessional motion. Thus, it is not sure if the metastable state must be visited if we come from the higher barrier since the system actually has enough energy to directly overcome the second barrier by precessional motion thus avoiding to fall into the closest minimum as it would if the motion would follow the steepest descent. However in the case of high damping we also expect to fall down to the closest minimum and thus to visit the metastable state.

One can think of a paraglider. First he has to walk up to the mounting. The walking corresponds to the thermally driven climbing uphill in the micromagnetic energy landscape. At the mountain top the flight starts. Starting from a high point he can fly over mountains and valleys which have smaller height than the starting point (saddle point). This flying part of the journey corresponds to the precessional part of the motion downhill.

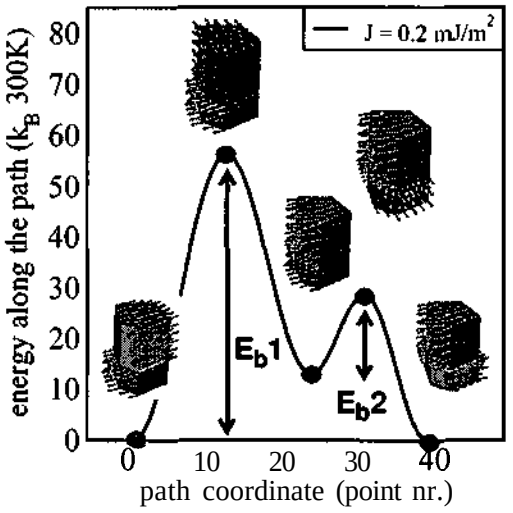

Figure 4.13 Energy along the optimal path for two antiferromagnetically coupled grains. The intergrain exchange coupling $J=0.2\ mJ/m^2$ (J^*Area ~ 4.8 k_BT). The magnetization reverses in two steps, passing two energy barriers. The material properties are shown in Fig. 8.1

5 REVERSAL MODES AND ENERGY BARRIERS IN DISCRETE RECORDING MEDIA WITH PERPENDICULAR ANISOTROPY

Discrete media show great potential for future ultra-high density magnetic recording. A hybrid finite element / boundary element method is used to compare the magnetization reversal process in a perpendicular granular film, patterned media, and a single magnetic island. The results show that the influence of magnetostatic interactions on the switching field is comparable with the spread of the nucleation field due to the dispersion of the magnetic easy axes. For CoCrPt this value is about 75 kA/m. Further, we use the nudged elastic band method to calculate energy barriers as function of the intergranular coupling strength. Below a critical coupling strength the magnetization reversal process changes from single large island reversal to the individual switching of separated grains.

5.1 Introduction

The term discrete media is used to refer to media that consist of arrays of discrete, for example ion-beam patterned magnetic elements [84], each of which can store one bit of data. Ideally, the storage density is then equal to the surface density of the elements. In patterned media, each discrete element is exchange isolated from other elements, but inside each element polycrystalline grains are strongly exchange-coupled, behaving more like a larger single magnetic grain. Nevertheless the micromagnetic simulations show that a single island reverses incoherently by the expansion of a small reversed nucleus. For the calculation of the magnetostatic interactions between the islands a novel hierarchical method is applied. We compare the hysteresis behavior of a single island, a continuous film and patterned media. In addition we analyze the effect of the magnetostatic interactions on the coercive fields and calculate the dynamic coercivity as a function of the Gilbert damping constant a. In the last section we use a more complex model to introduce grain boundaries between the grains allowing a variation of the intergranular exchange coupling strength. We compare switching fields for different coupling strengths. Using the nudged elastic band method we also calculate the energy barriers as function of the intergranular coupling strength.

5.2 Discrete ("patterned") media for perpendicular recording

The currently used thin film magnetic recording media consist of small, single-domain magnetic grains, which are exchange isolated from each other. For an acceptable media signal-to-noise ratio, each recording bit must contain a minimum number of grains. Grain diameters in the range of 7 nm to 20 nm and several tens to several hundreds of magnetic grains in each written bit are currently used (see figure 1.2). To increase the storage density further, the multigrain bits and therefore each grain in each bit must be scaled down to smaller sizes. However, if the grain size becomes too small, the magnetization state cannot be retained against thermal decay due to the small energy barrier height. The magnetization will switch easily, leading to loss of recorded data.

Patterned media [116,53] have long been one of the most promising approaches towards breaking through the boundary of conventional continuous thin film media. In the simplest scheme, the magnetic elements could have only a single axis of magnetization. The direction of magnetization is interpreted as a binary 1 or 0. Ideally, the storage density is then equal to the surface density of the elements. In patterned media, each discrete element is exchange isolated from other elements, but inside each element polycrystalline grains are strongly exchange-coupled, behaving more like a larger single magnetic grain. The single-domain magnetic element can be made of polycristalline materials as well as single crystal or amorphous materials. Because the superparamagnetic limit applies to the whole single island, not to each of the many grains as in a conventional continuous multigrain bit, the volume and switching energy for the single-element bit in the patterned media are much larger than that of a single grain in conventional continuous media, allowing significant reduction in bit size. The minimum volume of the discrete element bit is still determined by the superparamagnetic limit, and could be as small as a few nm in diameter, depending on the magnetic properties of the material. This gives an areal density as high as tens of Tbit/in^2. Another advantage of patterned media is that the SNR for the read head is increased due to the elimination of the random $N^{1/2}$ noise associated with acceptable number of decoupled grains within each continuous multigrain bit and elimination of the noise associated with irregular or zigzag transitions that cause noise in continuous thin film media.

Another advantage is that the constraints on the writing and reading process itself are greatly reduced [73]. Due to the single domain nature of every dot, the writing of such a bit is an all-or-nothing event and the head does not have to be positioned exactly above the bit. To

achieve a single domain like behavior the intergranular exchange between the grains in the island has to be increased. The grains then do not behave like an ensemble of decoupled grains but more like a large single grain only.

However there is a big disadvantage of patterned media. In order to make it into the magnetic recording market the net production cost of the disk media needs to be preferably less than US $ 1 [107] per disc! Currently existing techniques to produce patterned media are far above this value and a breakthrough in the production technique will be needed to decrease the costs.

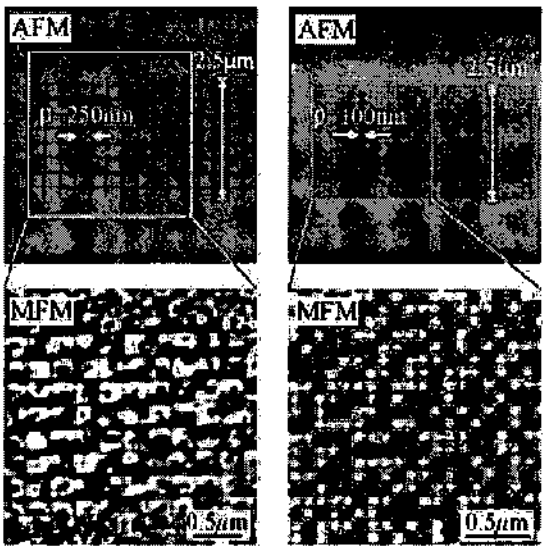

Figure 5.1 AFM and MFM images of square island arrays in granular CoCrPt recording media with a perpendicular magnetic anisotropy after magnetizing in a 1200 Oe field. The island periods are p = 248 nm (left) and p = 100 nm (right). [74]

For scientific use and demonstration applications, a possible patterning scheme removes magnetic material from existing media using a focused ion beam (FIB) [74]. Figure 5.1 shows AFM and MFM images of discrete magnetic islands produced by focused ion beam. The ion beam cuts 20 nm wide and 6 nm deep trenches into the ~20 nm thick $Co_{70}Cr_{18}Pt_{12}$ film forming square arrays of magnetically isolated islands with periods in the range of 50 nm to 500 nm. The irradiation does not remove all the material but makes the magnetic material non magnetic (see figure 5.2). A 50 nm periodicity would represent a storage density of about

250 GBit/in^2. The islands have a granular structure with cylindrical grains with a typical diameter of 10 nm and a height comparable to the film thickness. The easy axis is perpendicular to the film plane with a random deviation of the easy axis from the plane normal within a cone of about 8°-10°.

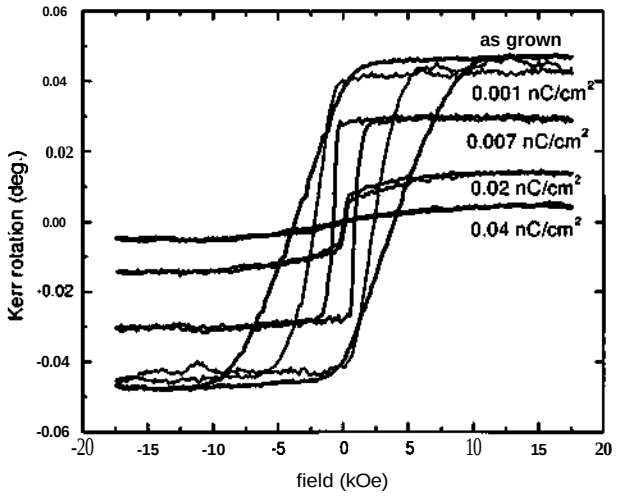

Figure 5.2 Patterning by ion irradiation. The irradiation does not remove all the material but makes the magnetic material non magnetic. The figure [6] shows a hysteresis loop for a material that was irradiated by an ion beam as a function of the irradiation dosis.

The patterned films were ac-demagnetized. A perpendicular field was decreased from 20 kOe to 100 Oe in 1% field steps with reversal of the field at each step. It was found that below a bit size of ~100 nm only single domain magnetization is observed (see figure 5.1 images on the right) while patterns with larger islands could support more than one domain (see figure 5.1 images on the left). Patterns with a periodicity of about 70 nm were of similar size to domains in unpatterned regions. Due to the absence of exchange coupling between the islands the magnetization after de-demagnetization tends to form a "frustrated checkerboard" distribution of "up" and "down" oriented magnetization states due to the strayfield coupling. Without strayfield effects a random distribution would be expected.

5.3 Finite element model of discrete media with granular structure

Based on the experimental work by IBM [84,85] we start with a continuous CoCrPt film (uniaxial anisotropy K_1 = 0.3 MJ/m³, exchange constant A = 10 pJ/m, magnetic polarization J_s = 0.5 T) consisting of 625 columnar grains, which are obtained from a Voronoi tessellation [95]. The grain diameter is 10 nm and the film thickness is 21 nm. The easy axis is perpendicular to the film plane with a random deviation from the plane normal within a cone of about 8-10° for each grain. We assume full exchange coupling between the grains. In a second step, we take out elements in a grid pattern, to obtain an array of individual islands. The island size is 70 nm with a gap of 20 nm (Fig. 5.3). The total size of our model is 250*250*21 nm. The model was meshed with 160000 finite elements.

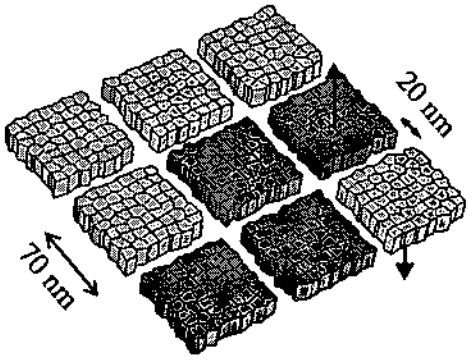

Figure 5.3 Islands of discrete media at an external perpendicular field of 870 kA/m. bright: Magnetization down; dark: Magnetization up.

The large number of nodes of the finite element mesh located at the surface of this model leads to capacity problems for the storage of the corresponding boundary matrix (see section 3). A tree algorithm [10] is applied in order to avoid this problem and to speed up the calculation of the magnetic strayfield.

5.4 Tree-algorithm

The dynamic response of a magnetic particle to an applied field follows from the LLG equation (2.6). The effective field is obtained from the variational derivative of the total Gibbs

free energy. For the calculation of the strayfield, $\mathbf{H}_{\text{str field}}$, a novel numerical method is used. The stray field is obtained from a boundary value problem,

$$\Delta u = \frac{\nabla \cdot \mathbf{J}}{\mu_0} \quad \text{and} \quad \mathbf{H} = -\nabla u \tag{5.1}$$

A hybrid finite element / boundary element method [43] is used to treat the magnetostatic interactions between the islands and to apply the boundary condition $u=0$ at infinity. The advantage of this method is that no finite elements are needed outside of the magnetic particle. For the solution of (5.1) we split u into two parts, $u = u_1 + u_2$. The potential u_1 is 0 outside of the magnetic particles and the solution of the Poisson equation with the boundary condition $\partial u_1 / \partial n = \mathbf{J} \cdot \mathbf{n} / \mu_0$. Then the potential u_2 is solution of the Laplace equation with the boundary condition [67]

$$u_2(\mathbf{x} \in \Gamma_y) = \frac{1}{4\pi} \oint_{\Gamma_y} \frac{u_1(\mathbf{y}) \cdot (\mathbf{x}-\mathbf{y})}{|\mathbf{x}-\mathbf{y}|^3} \mathbf{n}\, d\Gamma_y + \left(\frac{\Omega(\mathbf{x})}{4\pi} - 1 \right) u_1(\mathbf{x}) \tag{5.2}$$

Here Γ_y is the surface of the magnetic particles and Ω is the solid angle. The direct evaluation of (5.2) requires a matrix vector product with a fully populated N_s X N_s matrix. Especially for thin films as in the case of patterned media, the number of surface nodes N_s can get very high, since most nodes are located at the boundaries. The following method is more efficient The first term of the right hand side of equation (5.2) is the potential of a dipole sheet with the dipole density $u_1\mathbf{n}$ [67]. Therefore the surface integral over the surface Γ can be approximated by a sum over dipoles. The sum can be effectively evaluated using a tree code [10]. The potential u_2 at node k is

$$u_2^k = \sum_{i=1}^{N_\Delta} f(\mathbf{p}_i) \tag{5.3}$$

N_Δ is the number of surface triangles. Each surface triangle Δ_k has an assigned dipole $\mathbf{p}_i$ equal to the integral of the dipole density, $u_1\mathbf{n}$, over the triangle i. Since the dipole field decreases rapidly with the distance, dipoles far away from the node k are grouped together forming one larger dipole. This method reduces the computational effort from $O(N_S^2)$ to $O(N_S \log N_\Delta)$. The second term on the right hand side of (5.2) is local and thus of order $O(N_S)$.

Further details on numerical methods for speeding up the calculation of the magnetic stray field can be found in [41].

5.5 Hysteresis

The subsequent calculation of equilibrium states solving the Gilbert equation of motion provides the demagnetization curve (Fig. 5.4). In this quasistatic calculation a damping constant $\alpha=1$ was used. Figure 5.3 shows a stable configuration at an applied field of -870 kA/m. The individual islands switch at different values of the external field. In contrast, the continuous exchange coupled film shows a single switching field (Fig. 5.4). In the continuous film, the magnetization starts to reverse near the center of one edge, forming a bubble like domain (Fig. 5.5 and 5.7). The domain expands leading to the reversal of the entire film. In a single island the reversed domain is formed near one corner. The local demagnetizing field and the misorientation of the grains determine the nucleation field. The continuous film has a larger demagnetizing field and thus shows a lower switching field as compared to the single island. The granular film and the granular single island switch at a single switching field. The demagnetization curve of the patterned media shows steps at the switching fields of the individual islands. The spread of the coercive fields is ΔH_c =144 kA/m. In a reference calculation without demagnetizing field the spread in the switching field of the individual island is smaller (ΔH_c = 84 kA/m). The fields are about 230 kA/m higher than in a calculation with magnetostatic effects. This result suggests that the magnetostatic interactions increase the spread of the switching field.

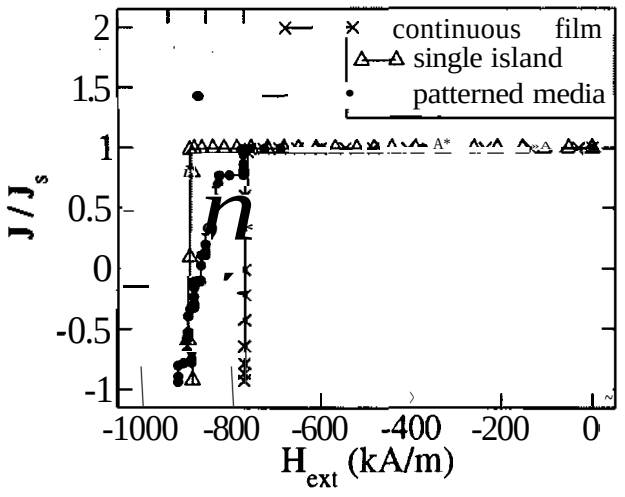

Figure 5.4 Calculated demagnetization curves for the granular film, patterned media, and a single island.

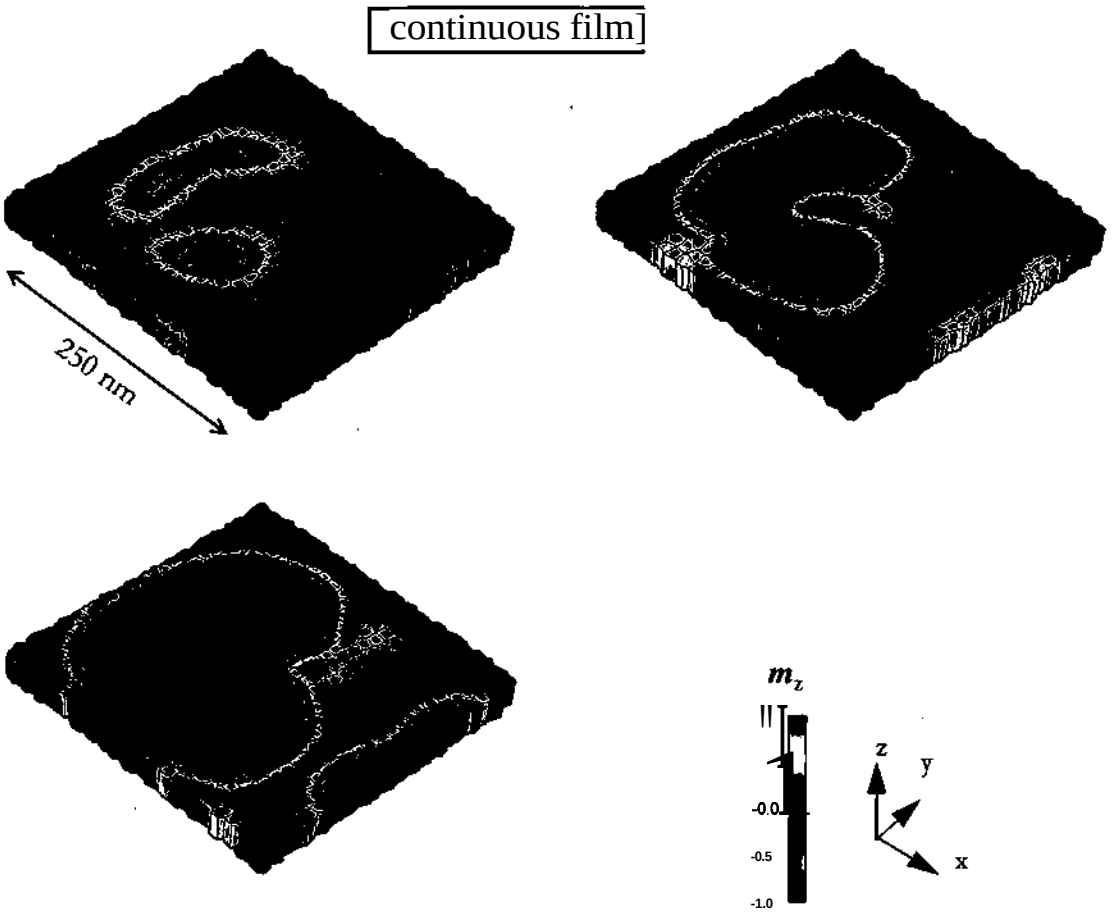

Figure 5.5 Magnetization states during the reversal of a 250 nm squared island with 625 grains. The reversal starts with formations of bubbles in the center regions where the magnetic stray field is strongest. α=1.

For large island size the reversal preferably starts with a nucleus of reversed magnetization near the center of the island while for smaller models the nucleation process starts at free edges or free corners. The numerical results qualitatively agree with experimental data (see figures 5.6 and 5.7).

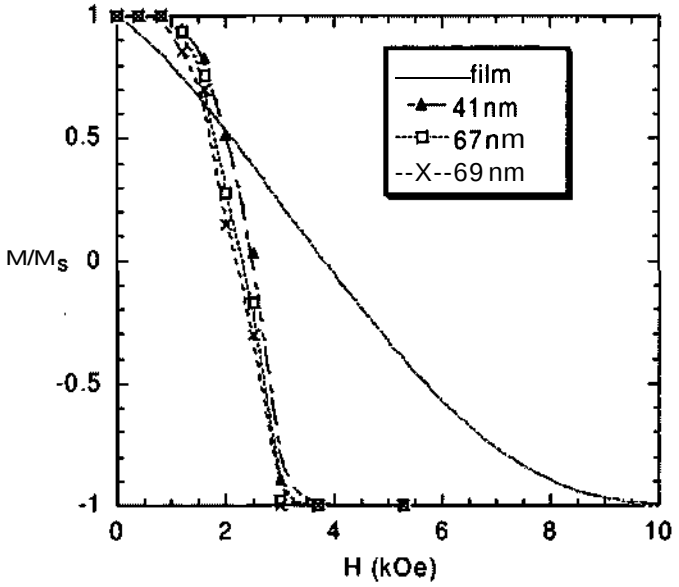

Figure 5.6 Experimentally measured remanent curves for a film and patterned film for different island sizes. The coercivity is reduced for the islands, however the nucleation field increased. [6] and [85].

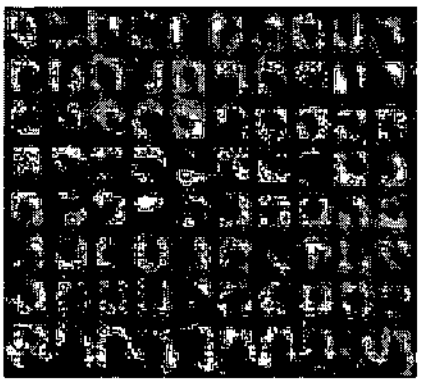

Figure 5.7 MFM images [6] for an array of 230 nm large islands. Bubble domains occur.

5.6 Dipolar interactions

To study the effect of the dipolar interactions, we considered an array of exchange decoupled islands, where each island represents one bit of data (Fig. 5.8). In order to reduce the computational effort, we simplify the model, focusing on the influence of dipolar interactions on the reversal process of a single island. We create an array of 121 islands. The "middle island" is the one of interest. It has granular structure consisting of 49 grains and is meshed with a fine grid of 5 nm finite element size. This is fine enough to resolve domain walls for the material parameters of CoCrPt.

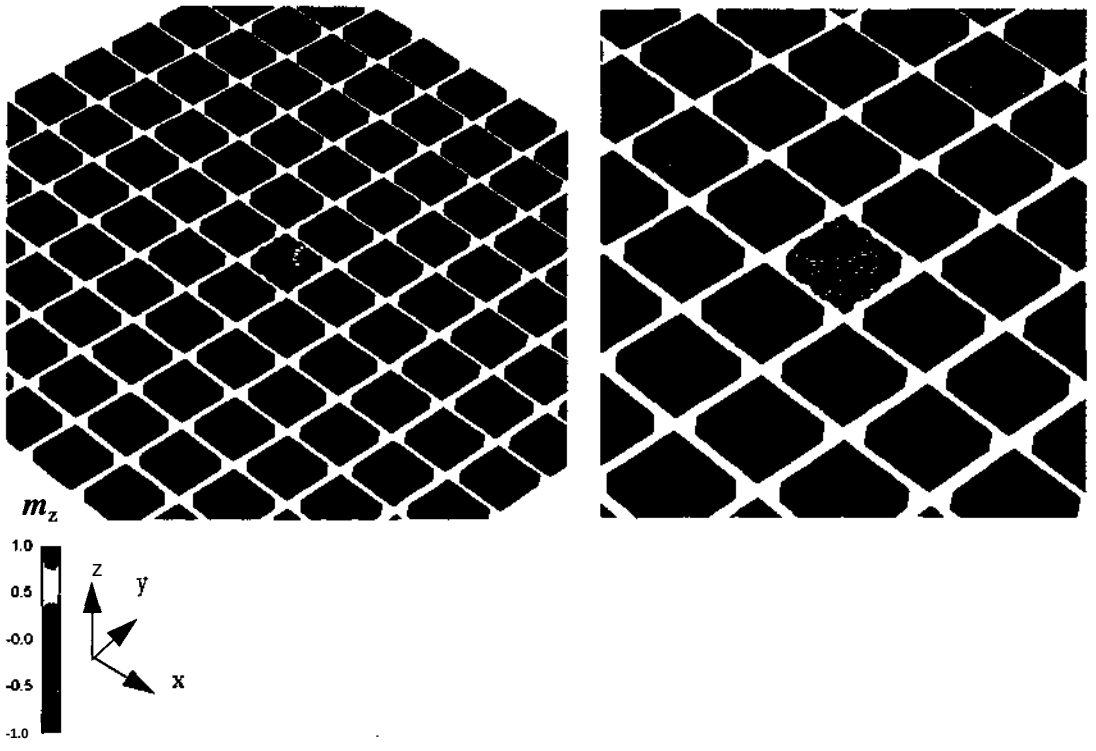

Figure 5.8 Bit pattern and finite element mesh of and array of discrete media. The magnetization is randomly set to "up" (red) or "down" (blue) representing the magnetization state of a hard disk with stored data. The island in the dotted region represents the region interest. For this island a granular structure and a fine FEM mesh is used.

The middle bit is surrounded by 120 additional islands. The only task of these islands is to produce the magnetic field. The external field is applied only in the region of the "middle island" which represents a very simple model of writing one bit on patterned media. Since the magnetization of the neighbor islands is kept homogeneous and unchanged during the simulation a coarser finite element grid can be used for the surrounding islands. With increasing distance to the "middle island" the size of the finite elements is increased, since their influence on the "middle island" position decreases rapidly with the distance.

The magnetization state of Figure 5.8 represents the bit pattern of a hard disk with written data. The written data (information) is assumed to look like a random magnetization pattern. For the average of many bits the total magnetization should be zero. The hysteresis was calculated for several bit patterns (different data stored) in order to study the dispersion of the coercivity owing to long-range magnetostatic interactions. The "worst case" is shown in Figure 5.9A where all neighbors are magnetized in the same direction as the middle bit leading to a demagnetizing field which favors the reversal of the middle bit. Therefore, the lowest coercivity is obtained while the "best case" (all neighbors are magnetized in opposite direction as the middle bit, see Figure 5.9F) has the highest H_c due to the stabilizing demagnetization field. In between, the more general cases with random magnetization states are found (B, D).

For data storage applications a small dispersion of H_c is desired. This will enable the optimization of the write head and the switching time. The above investigations show that dipolar interactions cause a maximum spread of H_c of 75 kA/m. This value is comparable to the dispersion of H_c caused by the misorientation of grains.

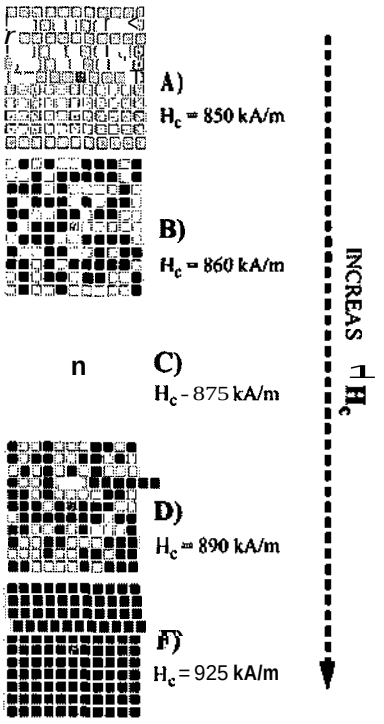

Figure 5.9 Magnetizations states and coercivity in patterned media. A) all neighbors "up" B) random C) isolated island without neighbors D) random F) all neighbors "down"

5.7 Writing speed

Beside the effort of reaching higher and higher areal densities, another crucial point for magnetic recording applications is a fast writing speed in order to guarantee high data rates. To study the writing time of a single bit, an external field is applied perpendicular to the film plane which is increased linearly in time with different speeds (field "sweep rate"). Now H_c depends on the speed of change of the external field [9].

Calculations were made for low damping (a = 0.02) and for high damping (a = 1). Figure 5.10 shows the calculated dynamical coercivity of the patterned media. H_c depends on both the damping constant CC and the sweep rate of the external field. H_c increases with increasing

sweep rate of the external field. Thus, a higher field has to be applied for writing at higher speed. This effect itself also depends on a, and is stronger for smaller damping constants (Figure 5.10). For a very low sweeping rate of the external field, H_c approaches the limit obtained in a static hysteresis curve for both values of the damping constant (a = 1 and a = 0.02). The static limit does not depend on the damping constant a.

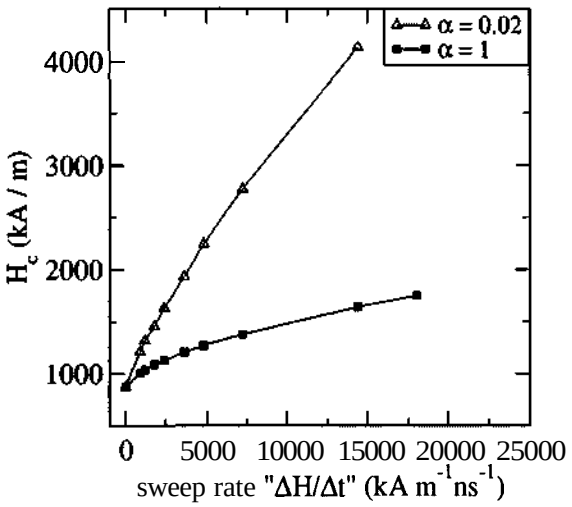

Figure 5.10 Coercivity as a function of the field sweep rate for two different values of the damping constant α.

5.8 Multi domain structures

In order to study the formation and the stability of multi-domain states of the islands a local external field was applied covering only a certain amount of the area of one single island. This experiment will test whether a two-domain state is stable. For an island size of 70 nm a two domain state has a higher total energy due to the domain wall energy than the state with homogeneous magnetization parallel to the easy axes. The two domain state also represents a local energy minimum. The magnetization can stay in the metastable state after the field pulse

is turned off. Shifting the domain wall to the left or right leads to a higher strayfield energy. An energy barrier has to be overcome to achieve the single domain state (see Fig. 5.16).

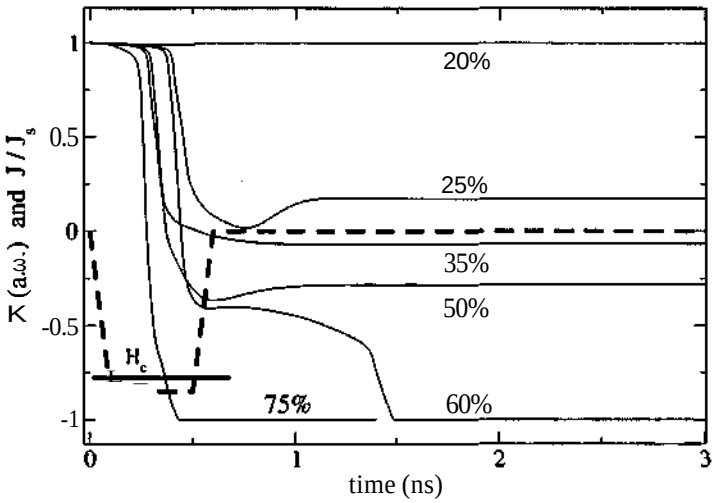

Figure 5.11 Time evolution of the magnetization in a single island for different area coverage of the field pulse (dashed line). For 1 ns an external field was applied with a strength of 1.1 H_c (switching field).

The results are shown in Fig. 5.11. If the external field covers 25%-50% of the island's area the final magnetization configuration is me metastable state after the field pulse has been switched off. Below 25% coverage the magnetization stays homogeneous also during the field pulse. This indicates, that the field covering this small area cannot create reversed domains. Above 60% coverage of the whole island reverses its magnetization.

5.9 Energy barriers as a function of the intergranular coupling

5.9.1 Two coupled single domain grains

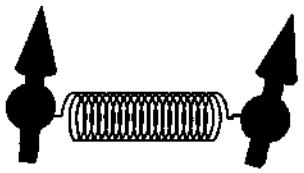

Figure 5.12 Model of two exchange coupled spins as a simplified description of two small magnetic grains separated by a grain boundary.

Using the saddle search algorithm we are able to study the effect of coupling strength of the grain boundaries on the energy barrier. We start by illustrating the problem on a system of two single domain particles with perpendicular uniaxial anisotropy which are exchange coupled. The system is fully described by four angles. In an approximation we fix the rotation plane of the two spins and the magnetization of one spin along its easy axis. Only one of the spins can rotate and the problem can be described with one angle in this rough approximation. For weak coupling the system has to pass two energy barriers visiting a metastable state in between where the two spins are antiparallel. This metastable state disappears above a critical coupling value and the reversal is a single barrier crossing mode. In this simple model we first write down the total energy as

$$E = E_{interface} + E_{anisotropy} = -\frac{J \cdot Area}{2}\cos\vartheta + K \cdot V \cdot \sin^2\vartheta \tag{5.4}$$

Here / is the exchange constant in J/m and *Area* is the total grain boundary area. To calculate if a local energy minimum is present we differentiate by ft and set the expression to 0 which gives

$$\vartheta = acos\left(-\frac{J \cdot Area}{4 \cdot K \cdot V}\right). \tag{5.5}$$

For $J \cdot Area > 4KV$ the relation has no solution. Above this critical coupling strength $J_{critical} = 4KV/Area$ the local minimum disappears.

A full model needs four angles to describe the system however it reduces to two angles since both spins stay in the same plane due to symmetry arguments [22]. The energy then becomes:

$$E = -\frac{J \cdot Area}{2} cos(\vartheta_1 - \vartheta_2) + KVsin^2\vartheta_1 + KVsin^2\vartheta_2 \tag{5.6}$$

Now the situation is already more complex since we need to find the saddle point(s) in a 2D energy landscape. First we need to find all points $(\vartheta_1, \vartheta_2)$ where $\nabla E = 0$, here

$$\begin{pmatrix} \frac{\partial}{\partial\vartheta_1}E \\ \frac{\partial}{\partial\vartheta_2}E \end{pmatrix} = \begin{pmatrix} 0 \\ 0 \end{pmatrix} \tag{5.7}$$

In a second step we need to find which of the solutions are saddle points. For this we calculate the determinant of the Hessian

$$det\begin{bmatrix} \frac{\partial^2 E}{\partial\vartheta_1\vartheta_1} & \frac{\partial^2 E}{\partial\vartheta_1\vartheta_2} \\ \frac{\partial^2 E}{\partial\vartheta_2\vartheta_1} & \frac{\partial^2 E}{\partial\vartheta_2\vartheta_2} \end{bmatrix} = \begin{cases} = 0 & saddle \\ > 0 & minima \\ < 0 & maxima \end{cases} \tag{5.8}$$

Points where (5.8) is zero are saddle points. Depending on the ratio of J/K more than one saddle point can exists, allowing more than one reversal mode. This is true when the coupling energy J is of about the same strength as the anisotropy energy K. For very strong coupling only one saddle point will "survive". A detailed theoretical work which deals with such a 2D system can be found in [22]. A recent work [114] on thermally induced switching of two coupled magnetic grains also includes simple subgrain discretization

For systems with many dimensions as for example our finite element micromagnetic models equation (5.7) gives a system of non linear equations. Also the calculation of the Hessian in (5.8) becomes very time consuming since the effort grows quadratically with the degrees of freedom. Thus, as an alternative to the procedure described above we use the nudged elastic band method (section 4) to calculate the saddle points between local energy minima.

5.9.2 Grain boundaries in patterned media

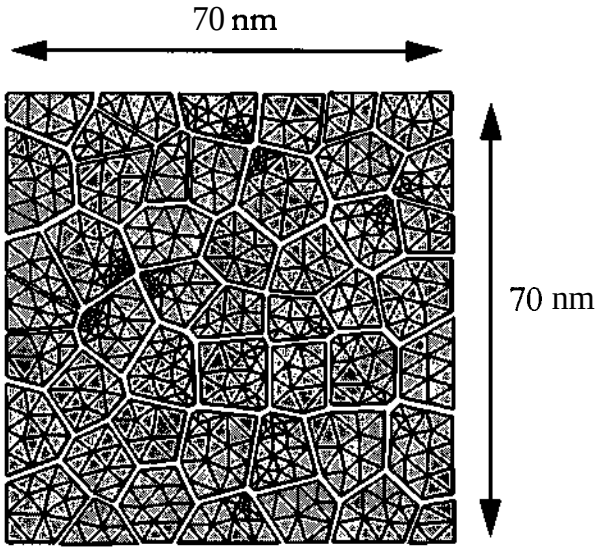

Figure 5.13 Island of patterned media showing grain structure (49 grains) and finite element mesh (18300 elements, 5560 nodes). The grains are separated by 1 nm grain boundaries. The exchange coupling between the grains can be varied. The film thickness is 21 nm and the average grain size diameter 9 nm.

We investigate the dependence of the energy barrier on the strength of the intergrain coupling. A model of 49 irregularly shaped grains was constructed (figure 5.13). The grains are separated by a nonmagnetic grain boundary of 1 nm thickness. We vary the coupling strength / between the grains from 0 up to 5 mJ/m^2. The average grain volume in the model is $9 \cdot 9 \cdot 21$ nm^3 and the total coupling area A to all neighbors $4 \cdot 9 \cdot 21$ nm. We can now express the coupling strength as a ratio of the maximum possible exchange energy due to intergrain coupling versus the anisotropy energy KV of one grain:

$$h = \frac{A \cdot J}{K \cdot V} \tag{5.9}$$

K is the magnetocrystalline anisotropy constant and V the volume of the grain. For K=300 kJ/m^3 and J=0.1 mJ/m^2 this gives h=15%. This gives a better understanding of the observed effects as a function of the coupling. For $h > 1$ the coupling is strong compared to the anisotropy energy and the grains will reverse more like one large grain. For weaker cou-

pling the exchange is too weak to induce a collective reversal of the grains. The grains will reverse individually. Other coupling strengths expressed in KV are found in table 2

J [mJ/m^2]	b [%]
0.01	1,5 %
0.1	15 %
0.5	74 %
1	148 %
5	741 %

Table 2 Some values of the exchange coupling expressed in terms of the uniaxial anisotropy energy of one grain.

Snapshots of the magnetization states during the reversal in a quasistatic hysteresis are shown in figure 5.14. For weak coupling, the grains reverse individually. For strong coupling, the reversal again starts with the nucleation of a reversed domain near the edge and its expansion.

Fig. 5.15 shows demagnetization curves in a quasi static calculation for different intergrain exchange coupling. For $J > 0.5$ mJ/m^2 the demagnetization curve becomes squared. Below this value the island switches in steps and the resulting H_c is higher than at stronger exchange. However the nucleation field increases with increasing coupling strength. In [5] experiments were performed on Co patterned elements. Single island hysteresis measurements show the squared characteristic of the demagnetization curve as described above.

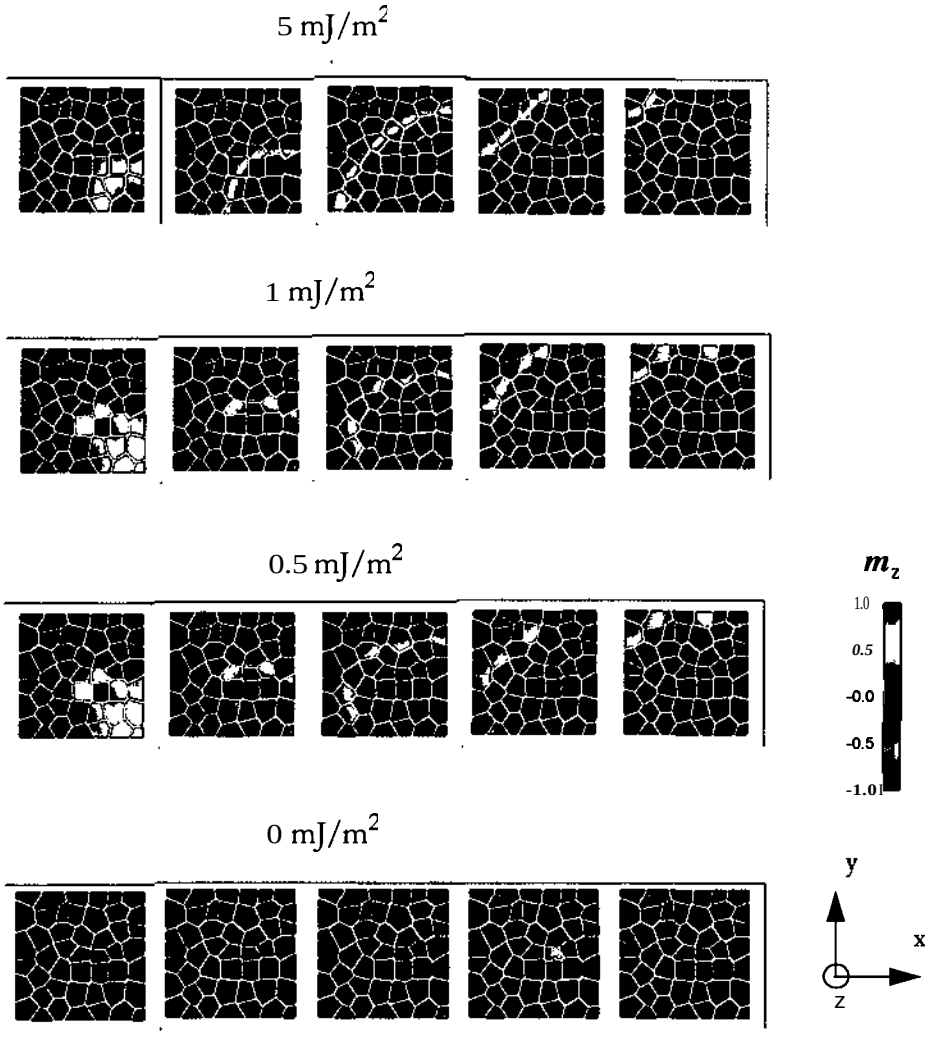

Figure 5.14 Reversal modes during a hysteresis loop as function of the intergrain exchange coupling. The field was applied perpendicular to the film plane. The easy axis distribution (up to 8° disturbed from the film normal) was same for all cases. The first image shows the nucleation start. A damping constant $\alpha = 1$ was used.

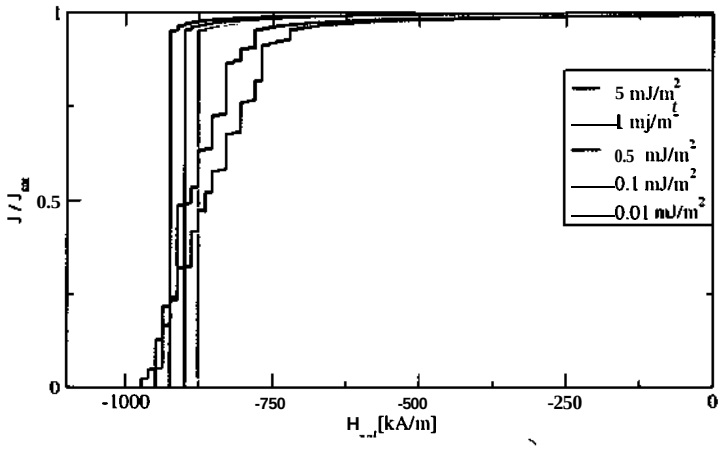

Figure 5.15 Demagnetization curves in a quasistatic calculation for different intergrain exchange coupling. For / > 0.5 mJ/m^2 the demagnetization curve becomes squared. Below this value the island switches in more steps and the resulting H_c is higher than at strong exchange. The nucleation field however increases with increasing coupling strength.

In a next step we calculated the energy barrier for a 70 nm island as function of the intergrain coupling strength. The grain boundary thickness was 1 nm. Fig. 5.16 compares the minimum energy paths for zero intergrain exchange (J = 0 mJ/m^2) and strong (J=5 mJ/m^2) coupling strength. For zero intergrain exchange, the grains in the island all switch individually. The thermal stability is determined by the thermal stability of the individual grains. At strong coupling the grains behave like one large grain. The resulting energy barrier is much higher than at weak coupling. The reversal starts with nucleation on one corner and the expansion of the reversed domain. Note that also a metastable state is present where the magnetization is in a two domain state. The total energy barrier is much higher than at weak coupling. This allows a further downscale of the island size without running into problems of thermal stability.

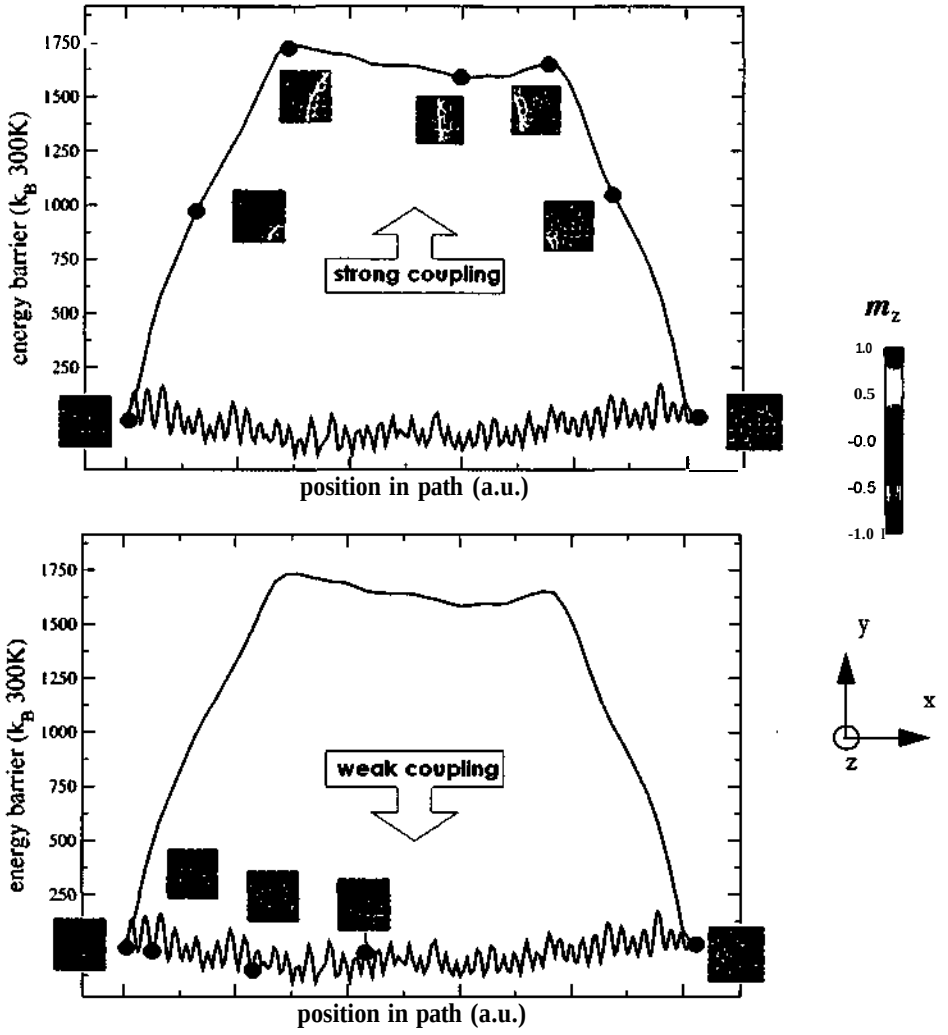

Figure 5.16 Comparison of the minimum energy paths for zero intergrain exchange (h=0) and strong (h — 740%) intergrain coupling. Intergrain exchange has a strong effect on the total energy barrier of the system.

5.10 Dependence of the energy barrier on the island size

In the following we assume perfectly coupled grains. The energy barrier was calculated as a function of the island size and the results were compared with a simple analytical estimate. Fig. 5.16 shows that the thermal reversal of the patterned island basically involves the creation of a two domains. Due to the high magnetocrystalline anisotropy, the height of the energy

barrier is mainly determined by the domain wall energy of the two domain state. In the following analytical estimation we neglect the contribution from the magnetostatic interaction. The energy barrier height is then equal to the domain wall energy

$$E_1 = Area \cdot 4\sqrt{AK_1} \quad . \tag{5.10}$$

Here *Area* is the total domain wall area. Below a critical si2e, this energy will be higher than the energy barrier for coherent rotation which is

$$E_2 = Volume \cdot K_1 \quad , \tag{5.11}$$

where *Volume* is the island volume. For an island with lateral extension l and thickness t, we have $Area = lt$ and $Volume = llt$. If we set $E_1 = E_2$, we obtain the critical size for coherent rotation

$$l_{critical} \leq 4\sqrt{\frac{A}{K_1}} = 4\delta_0 . \tag{5.12}$$

Note that the result is independent of the height of the island, and is equal to 4 times the Bloch parameter δ_0. If the island size is smaller than $4\delta_0$ we expect uniform rotation. With A = 10 pJ/m, K_1 = 300 kJ/m^3, and t = 21 nm the critical island size becomes ~23 nm.

The numerical calculation of the minimum energy path shows that there is a continuous transformation between the inhomogeneous reversal and the uniform rotation mode as the size decreases. Thus, non-uniform reversal modes were found even for an island size of 20 nm. Fig. 5.17 shows the size dependency of the energy barrier. The energy barrier is given in units of KV. This is equal to an effective switching volume, V_{eff} divided by the total volume ($E_B/KV = V_{eff}/V$). For all island sizes the analytical model overestimates the energy barrier height. The strongest deviation is found when the island size is near the calculated critical size. At 20 nm island size, the calculated energy barrier is 10% smaller than in the uniform rotation model (Figs. 5.17 and Fig. 5.18). The reversal mode is still inhomogeneous which is seen in Fig. 5.18.

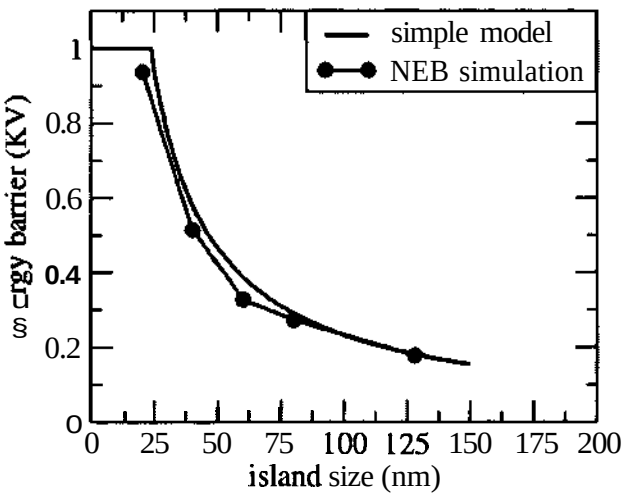

Figure 5.17 Energy barrier in units of KV as a function of the island size for squared islands. The analytical model always overestimates the energy barrier as compared to the micromagnetic energy barrier computation. Moreover it can be seen in Fig. 5.18 that the reversal mode is inhomogeneous even in the regime (< 23 nm) where uniform rotation is expected. The height of the islands was 21 nm, $K_1 = 300\ \mathrm{kJ/m^3}$, $A = 10\ \mathrm{pJ/m}$.

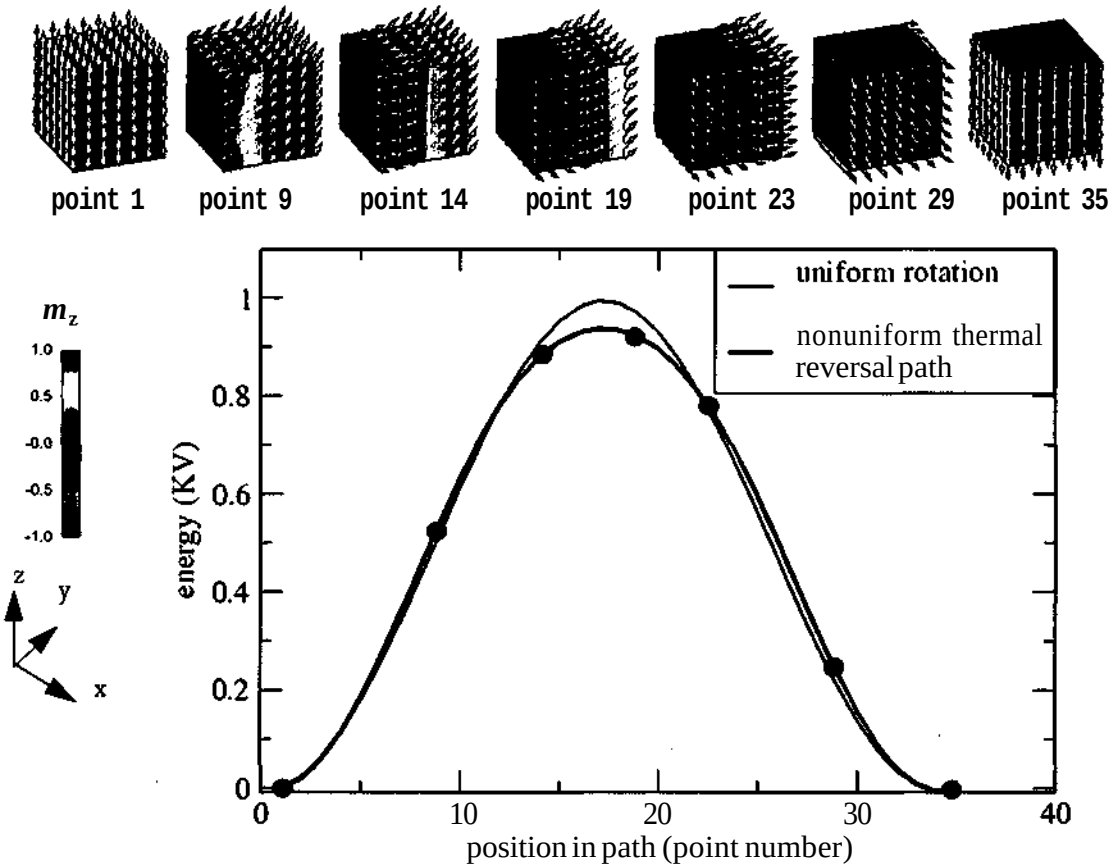

Figure 5.18 Energy along the minimum energy path (red) for the thermal reversal of a 20 nm island. The black curve shows the energy along the path for the uniform rotation mode. The micromagnetic NEB computation gives a 10% lower energy barrier than the uniform rotation model. The top sequence images show that the reversal mode in the minimum energy path is inhomogeneous even though uniform rotation would be expected at this island size. The height of the islands was 21 nm, K_1 - 300 kJ/m^3, A = 10 pJ/m.

6 VORTEX CORE REVERSAL BY BLOCH POINTS

Thin permalloy disks support a vortex configuration. We study how micromagnetic calculations can be applied to processes that involve a singularity of the magnetization field, namely the Bloch point. The reversal of the core of the vortex under an field applied perpendicularly to the disk plane is investigated. We apply two different procedures to evaluate switching fields and processes: direct micromagnetic time-dependent calculation, and the evaluation of the energy barrier that separates the two orientations of the vortex core in the configuration space, using the nudged elastic band method. Both methods show the occurrence of Bloch points during reversal. The numerical results are compared with recent experiments.

6.1 Introduction

In 1965, Ernst Feldtkeller first considered the consequences of the hypothesis of continuity of magnetic structures [40]. He showed that in certain situations, non-continuous configurations have to exist. The basic such configuration is the so-called Bloch point (BP). It is defined by the following property: For any closed surface (i.e. sphere-like) surrounding of the point, the magnetization vectors on this surface cover exactly once the surface of the unit sphere. Topological arguments have been used to show that the BP is the only stable singularity in a ferromagnet [71] when one considers all the continuous transformations. Thus, a BP cannot appear alone within a continuous structure: either it is created in a pair, or it comes in by the boundary of the sample.

The modeling of this singular structure is, however, not fully satisfactory. Indeed, the definition of the BP implies that the modulus of the magnetization must vanish at the BP center, so that micromagnetics does not apply in this region. Indeed, micromagnetics is derived from atomistic models under the assumption of a continuous magnetization distribution, slowly varying on atomistic scale [18]. Considering a sphere surrounding the BP and sufficiently far from it so as to apply micromagnetic theory, Feldtkeller [40] showed that the leading energy density is the exchange energy. This term is smallest when the magnetization direction at a given point is the unit vector from the BP to the point considered. A rotation of all moments by the same amount does not change the exchange energy. In this case the exchange energy density becomes

$$dE_A = (2A/r^2)r^2 dr \sin\theta d\theta d\varphi \tag{6.1}$$

with r, 0 and 9 being the spherical coordinates, and A the exchange constant. Although the exchange energy density diverges at the origin, the integrated energy within a sphere of radius R is finite

$$E_A(R) = 8\pi AR \tag{6.2}$$

Döring then showed that the next important term is the demagnetizing energy.

Only crude estimates exist for the energy of the core of a BP, where the magnetization falls to zero. Reinhardt [82] computed classically the exchange energy around a BP, using a Heisenberg formulation (such a formulation does not rely on the assumptions of a continuous and slowly varying magnetization distribution). He found that the atomiclike computation gave a lower energy than the continuous calculation. The difference is

$$\Delta E_{discrete} = -Aa_0\Delta(\boldsymbol{r}_0) \tag{6.3}$$

with a function A depending slightly on the exact location $\boldsymbol{r}_0$ of the BP within the lattice. For a cubic lattice Reinhardt computed A ~ 13. Therefore, as already stated by Hubert [63], the core corrections can be estimated to be much smaller than the micromagnetic contribution, as soon as the extension of the BP micromagnetic structure is large compared to atomic distances. This justifies micromagnetics calculations with BP cores.

We consider a disk-shaped permalloy sample, of such size so as to develop a vortex structure. Using to different methods, micromagnetic dynamics and the nudged elastic band method, we study the reversal of the vortex core under a field applied perpendicular to the disk plane. This reversal involves the creation and motion of BPs while the core reverses. The complete work with detailed investigations of the Bloch point at rest in the middle of the core of the vortex, and the comparison of the evolution of the calculation results under decreasing mesh size to analytical results can be found in [108].

The situation corresponds to recent experiments by Okuno et al. [79], in which the vortex core orientation is observed by MFM in remanent state. An array of permalloy disks is subjected to an applied field for a macroscopic duration (l min. typically), and a subsequent image allows to count the number of cores that have switched. A switching field distribution

is measured, for series of disk diameters at a fixed thickness of 50 nm. An example of MFM images of an array of permalloy disks is shown in Fig. 6.1.

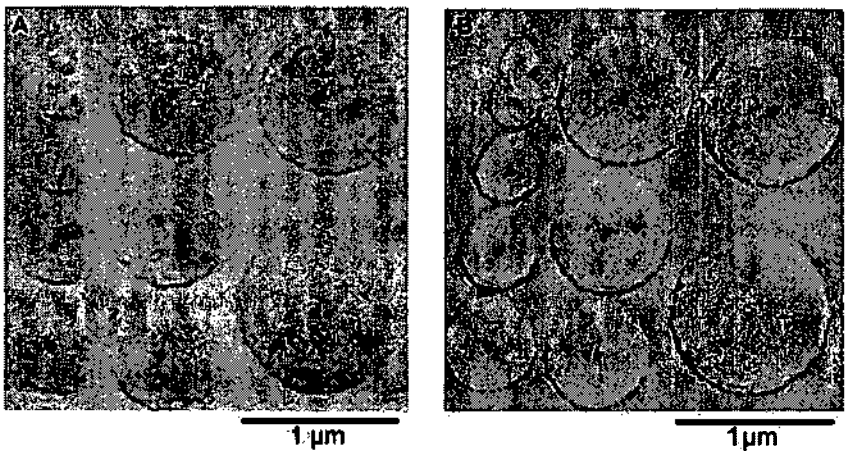

Figure 6.1 MFM images [97] of an ensemble of 50 nm thick permalloy dots with diameters varying from 0.1 to 1 µm after applying an external field of 1.5 T along an in-plane direction (A) and parallel to the plane normal (B). The dark and bright points in the center are showing the position of the vortex core. Both types of the vortex core orientations are present (dark and bright) in the left image.

In a recent work arrays of squared permalloy elements which support vortex configurations were studied with MFM [47]. Both the vortex rotation sense and the vortex core orientation can be clearly seen (Fig. 6.2). These two can be addressed independent of each other. This gives 4 possible magnetization states and one could think of a 4-bit recording as a possible application.

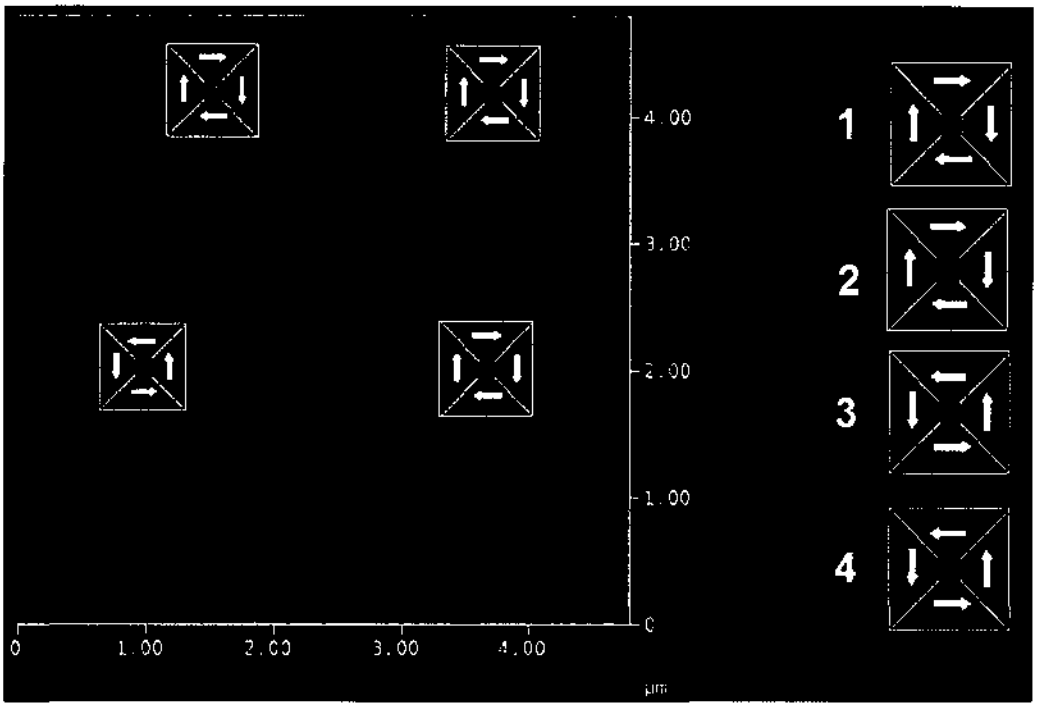

Figure 6.2 MFM images [47] of permalloy squares. Magnetization rotation sense and the vortex core orientation can be seen as independent degrees of freedom. This results in 4 possible magnetization states.

6.2 Finite element model

The finite element method turned out to be a powerful tool in this particular problem using adapted meshes, as the vortex core only extends over a small part of the sample. For the calculation we used a 50 nm thick permalloy disk with the diameter of 200 nm, with a variation of the mesh size close to the disk symmetry axis. The central zone, of diameter 20 nm, was meshed with an average mesh size *d* between the nodes (d=1,2,3 and 4 nm). In the middle region, a ring with the radius from 10 to 20 nm, the mesh size increases from *d* for the radius of 10 nm up to 4 nm at radius 20 nm. In the outer ring (radius from 20 to 100 nm) the mesh size increases from 4 nm to 10 nm. The mesh size along the thickness was constant. This is achieved with the following strategy using the mesher "MSC Patran" [124]:

- Create a disk with radius R1 (4 quarter disks)
  a) create a line of length Rl

b) create a quarter circle (create->surface->revolve)
c) copy this quarter (shifted)
d) create a solid with this two surfaces (create solid, method = 2 surfaces)
e) delete the "points", "lines" and "surface" objects
f) copy the solid to get the other 3 quarters (with transform object)

- Create a ring from R1 to R2 (also 4 quarters rings)
- Create a ring from R2 to R3 (also 4 quarters rings)
- We have now 3 cylindrical surfaces which are meshed with surface meshes. Mesh sizes were *d* nm at the cylinder surface (actually 4 quarters) with r=R1, 4 nm at the cylinder surface with r=R2 and with 10 nm at the one with r=R3 (=radius of the disk). See also Fig. 6.3 step 6.
- Now mesh the inner region with the average mesh size *d*, the ring between Rl and R2 with 4 nm and the outer ring with 10 nm.
- Delete the surface mesh and equivalence with about 0.05 tolerance.
- Now optimize, create surface elements, verify and export the file, finished!
- Note: Methods where the mesh is created using mesh seeds along edges or on surfaces of the dot does not work. Here the mesh size varies along the thickness of the dot

The above procedure is illustrated in Fig. 6.3.

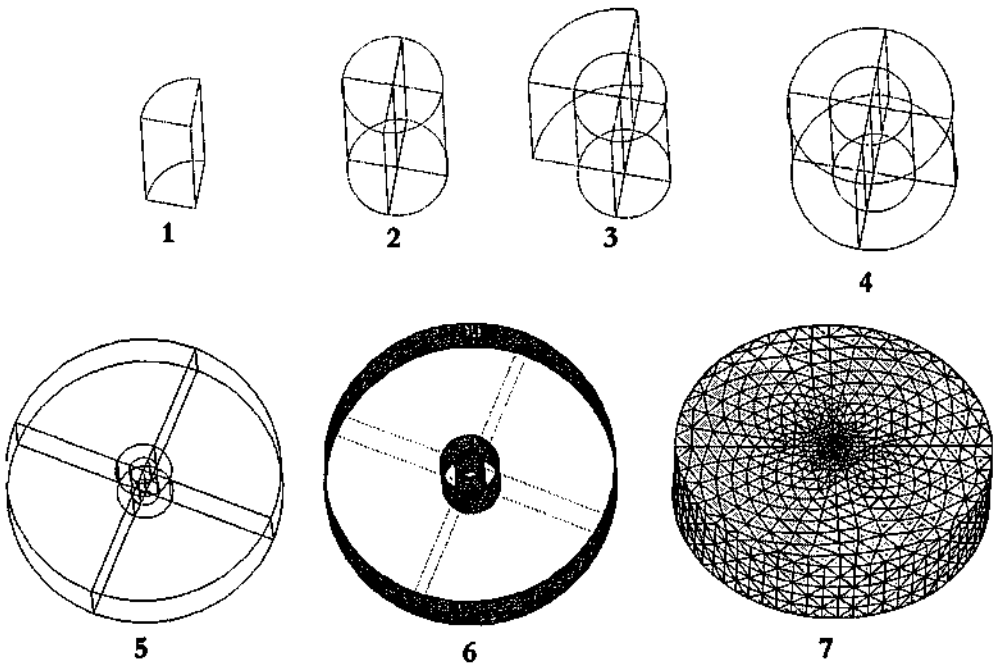

Figure 6.3. Construction of a graded mesh for the investigation of magnetic vortex structures. Concentric cylinders are meshed with different mesh size. This procedure guarantees a mesh where the mesh size does not vary across the thickness of the disk (see Fig. 6.4).

Fig 6.4 shows such a cut for a mesh with $d = 2$. The figure shows that the extension of a Bloch point structure is smaller than 20 nm and that the adapted mesh is fine where it is needed. A large mesh size in the outer regions is allowed since the processes occur in the central region. The vortex and BPs stay along the rotation axis of the disk during the reversal processes when the field is applied perpendicular to the film plane. The core mesh size was varied from 1 to 4 nm in order to investigate the mesh size dependency on the calculated energy barriers and switching fields.

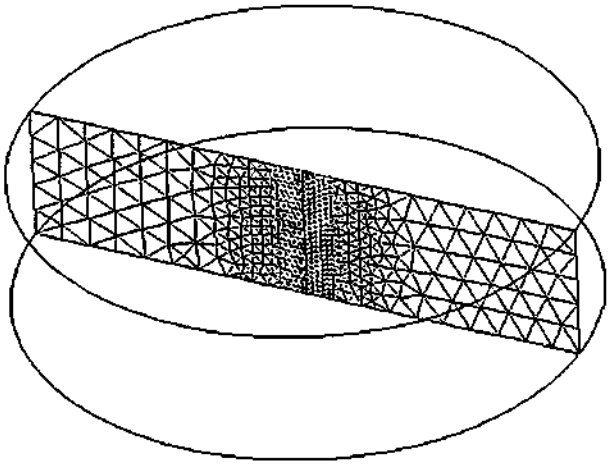

Figure 6.4 A) Perspective view of the mesh used for the barrier calculations. The cut was made trough one of the node planes used to generate the mesh. The finest mesh size is 2 nm in the central region (d=20 nm). Note that the extension of the vortex core is about 20 nm. The color code corresponds to the z-magnetization. Red: Magnetization up; Blue: Magnetization down; Green: Magnetization in-plane. The magnetization state has a bloch point in the center. The mesh is fine in the region where the magnetization is inhomogeneous.

6.3 Dynamic calculations

The switching of the vortex core under an applied field perpendicular to the film plane was investigated by quasistatic calculations: The field is increased by small steps. At each field value the Landau-Lifshitz Gilbert equation is integrated until equilibrium is reached. For the sake of completeness also dynamic calculations were performed where the field was increased

linearly from 0 T to l T in a time of about 5-10 ns. A realistic value for the damping constant a = 0.01 was adopted. The reversal mode found in the dynamic calculations was the same as in the quasistatic calculations, involving the creation and motion of a BP. In all calculations we used a permalloy disk with 200 nm in diameter and 50 nm thickness.

Fig. 6.5 shows a computed magnetization curve for a core mesh size of 2 nm. A linear slope is seen followed by saturation. On this curve the reversal of the core is seen as a small step since the volume of the vortex core is small compared to the rest of the sample at this size. In Fig. 6.5 this step is marked with a circle. The reversal of the core is seen more clearly when plotting the exchange energy versus the applied field (Fig. 6.6). The vortex core compresses under the action of an opposing field and the exchange energy increases. At 540 mT the vortex is so compressed, that the exchange energy density becomes higher than the exchange energy density around a BP. A BP can be created and the core switches by displacement of the BP across the thickness. After the core has switched the exchange energy is smaller since the reversed vortex core is decompressed (see magnetization states in Fig. 6.6). The results are in good agreement with the experimental results by Okuno [79] et al. For a disk diameter of 400 nm and a thickness of 50 nm, mean core switching fields of 380 mT to 450 mT were found.

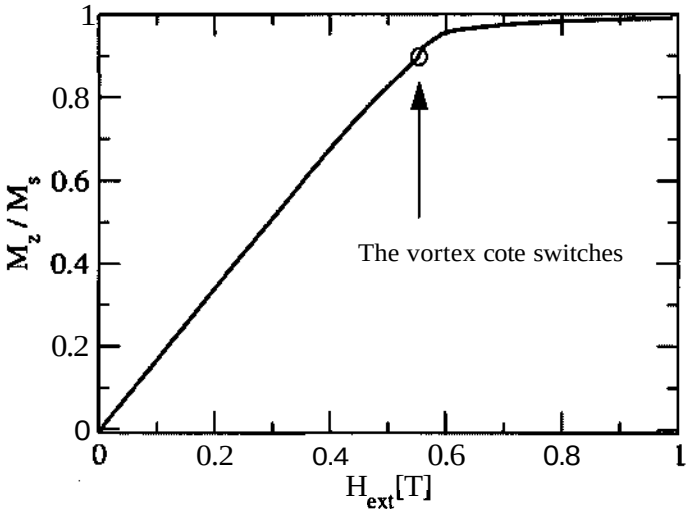

Figure 6.5 Magnetization curve for a permalloy disk (diameter = 200 nm, thickness = 50 nm) with a core mesh size of 2 nm. The field was applied opposite to the vortex core orientation. A linear slope is seen followed by saturation. On the curve the reversal of the core is seen as a small step since the volume of the vortex core is small compared to the rest of the sample at this size. This step is marked with a circle.

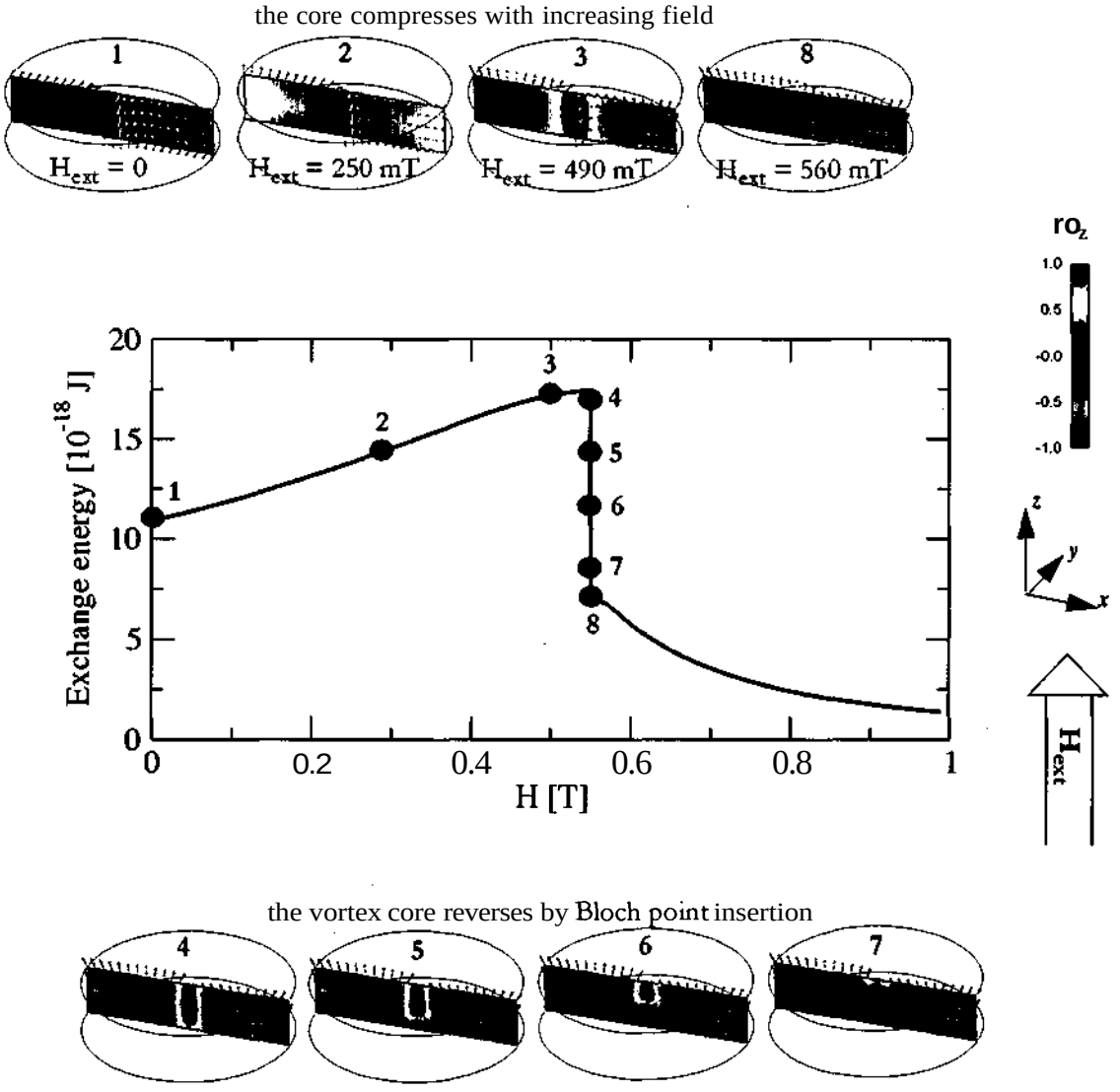

Figure 6.6 Quasistatic calculation of vortex core switching. A field is applied opposite to the vortex core orientation. The vortex core compresses with increasing field. At H_{ext} =540 mT the exchange energy density exceeds the exchange energy density of a BP structure. As a result the vortex core switches by insertion and motion of a BP. The disk diameter was 200 nm, thickness = 50 nm. The magnetization states during vortex core switching are shown as perspective cuts across the thickness through the center of the disk. In Fig. 6.4 the reversal is marked with a circle.

For the sake of completeness also dynamic calculations were performed where the field was increased linearly to 1 T in a time of about 4 ns. In these calculations a realistic value for the damping constant (X = 0.01 was used in order to involve the dynamic precessional effects

correctly. The reversal mode found in the dynamic calculations were same as in the quasistatic calculations, involving the creation and motion of a BP. Fig. 6.7 compares a quasistatic with a dynamic calculation for a permalloy disk with 200 nm diameter and 50 nm thickness. The magnetization state has a vortex core in the center of the disk. The field was applied opposite to the vortex core orientation. In the quasistatic calculation equilibrium is reached at each field step using a damping constant α — 1 (this speeds up the calculation). In the dynamic calculation the field increases linearly from 0 T to l T in a time of 4 ns. Thus, for the black curve the x-axis is also the physical time (H_{ext} = l T corresponds to t = 4 ns).

In both calculations the vortex core switches by insertion followed by displacement of a BP. However slightly higher switching fields are obtained with the dynamic calculation. This is explained by the rate at which the external field increases. With decreasing rate, also the reversal fields of the core decreases towards the results of the quasistatic calculation.

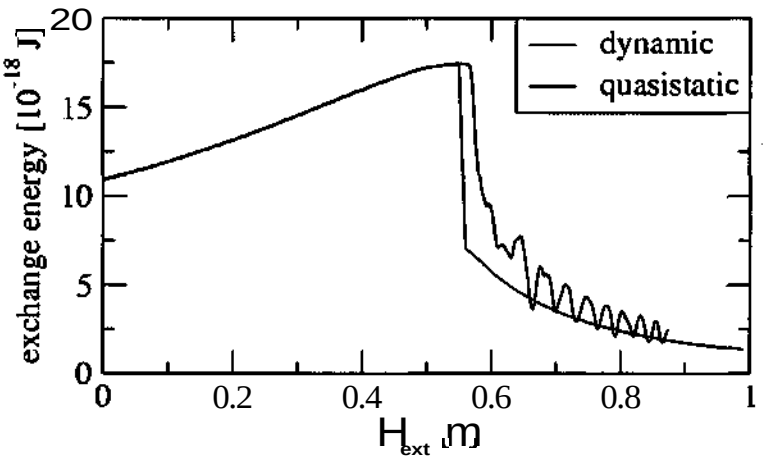

Figure 6.7 Comparison of a quasistatic with a dynamic calculation for a permalloy disk (200 nm diameter, 50 nm thickness) with a vortex core. The exchange energy during vortex core switching is plotted as a function of the external field. The core mesh size was 2 nm. The field was applied opposite to the vortex core orientation. In the quasistatic calculation equilibrium is reached at each field step. a = 1 was used. In the dynamic calculation the field increases linearly from 0 to l T in a time of 4 n and. (X = 0.01 was used. Thus, for the black curve the x-axis is also the physical time (H_{ext} = l T corresponds to t = 4 ns).

6.4 Direct computation of the energy barrier

We apply the nudged elastic band method in order to determine the relevant saddle points for the reversal of the vortex core. For the discretization of the path we typically use 25 points (images). When a field is applied the two stable magnetization states are possible which correspond to local minima of the energy. The saddle point moves closer to the initial (non switched state) and more than 25 points may be needed to achieve the desired resolution and accuracy at the saddle point position. The situation is shown in Fig. 4.5. Using the "climbing image" algorithm (see section 4.8) an improved resolution is obtained also with fewer images. The image with the highest energy moves along the path upwards trying to maximize the energy. Thus, it "floats" up exactly to the saddle point and eliminates the error which results from the discrete representation of the path. For the calculation of energy barriers at zero field one can also use only 3 images to speed up the computation. It may sound strange to use 3 points to discretize the path since the first and last state do not move. This means that only the middle image is optimized. From calculations with larger meshes we know that the saddle point is a state where the BP is exactly in the middle of the disk. Thus, the saddle point has the same distance in the configuration space to both the initial and the final state. Using 3 images only, the spring force keeps the central image equally spaced to both the starting and the final configuration. This means, that with 3 images an energy minimization is performed, however with the additional constraint that the configuration must stay in a hyperplane of the configuration space. This plane is normal to the straight line in the configuration space connecting the initial with the final state and is positioned in the middle of this line. All images in this hyperplane have the same distance to the initial and final state. Using this strategy we were able to compute the zero field saddle point with a mesh size of 1 nm in the center.

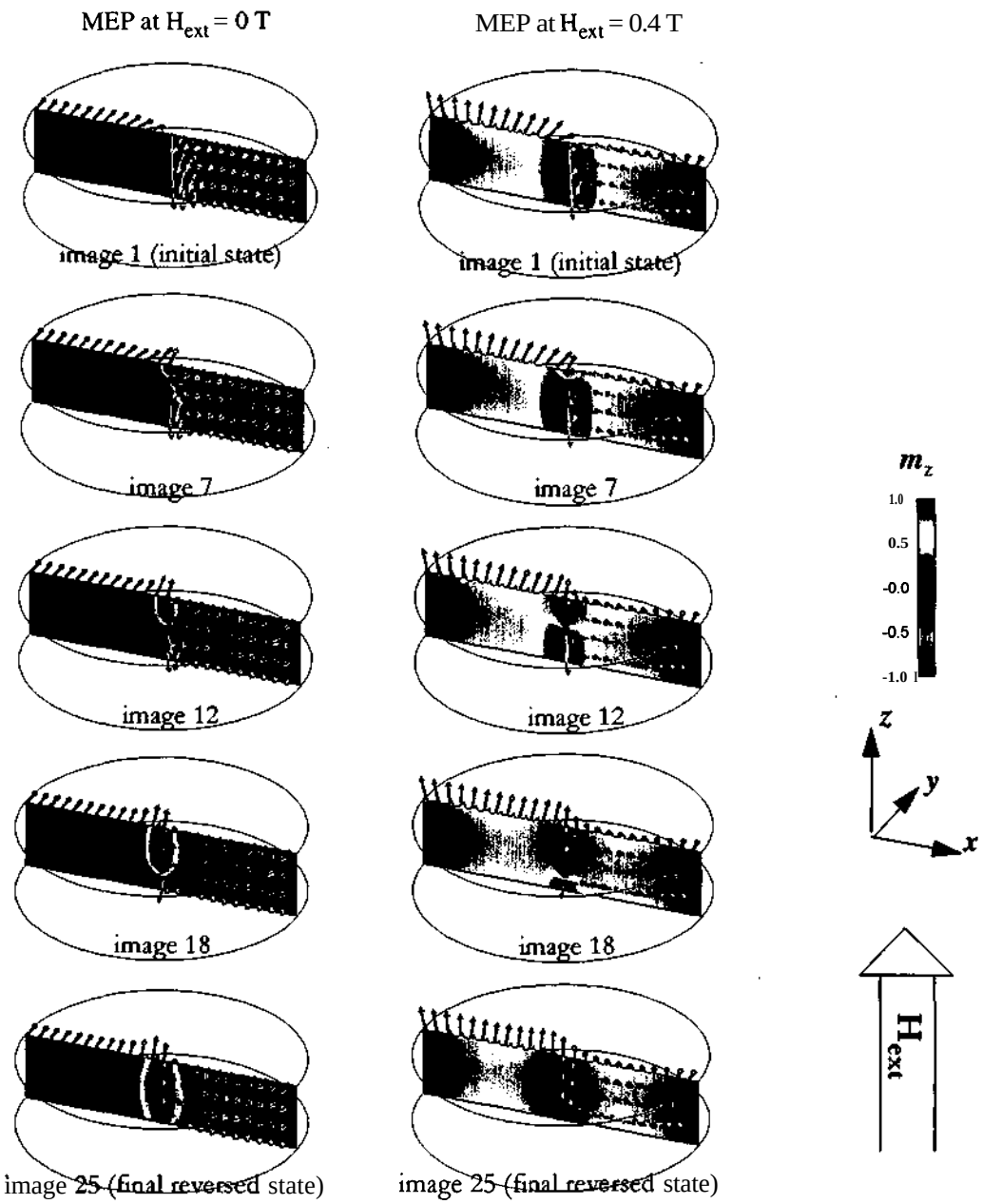

Figure 6.8 Minimum energy paths for the reversal of a vortex core in a permalloy disk (50 nm thickness, 200 nm diameter) at different external fields. The field is applied opposite to the initial vortex core orientation. The displayed plane shows a cut through the disk center. 25 images were used to discretize the path. The number of arrows does not correspond to the number of mesh points. The sequence on the left hand side shows the MEP for zero applied field. Note the compressed non-reversed vortex when a field is applied (sequence on the right). In both reversal paths a BP appears on the surface and moves through the vortex core. See Fig. 6.11 for the energy along these paths.

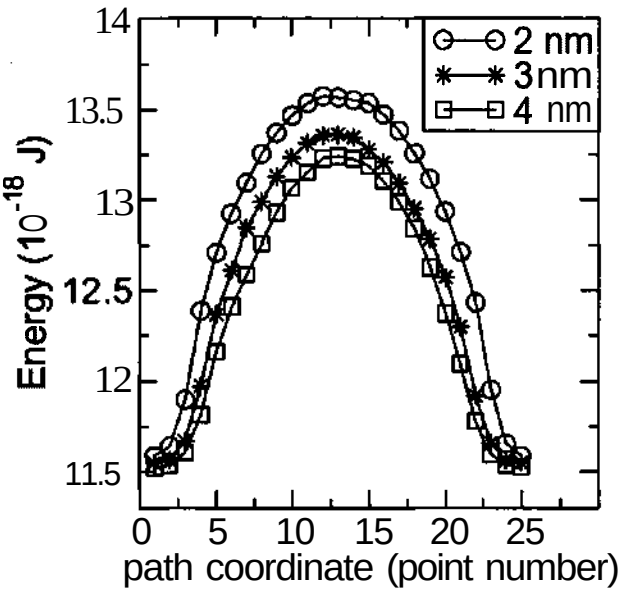

Figure 6.9 Calculated minimum energy paths for the reversal of the vortex core in zero applied field. The use of a finer mesh in the central zone (the mesh size, *d*, is indicated in the legend) leads to a higher barrier. Samples have a diameter of 200 nm and a thickness of 50 nm.

Figure 6.8 shows two magnetization states of two computed minimum energy paths. The left hand side sequence shows the path at zero applied field while 400 mT was applied (in the opposite direction of the initial vortex core direction) in the right hand side sequence. Note the compressed non-reversed vortex when a field is applied. In both reversal paths a BP appears on the surface and moves through the vortex core. Since the problem is symmetric, it is completely arbitrary on which of the surfaces (top or bottom) the BP appears. Indeed we obtained both paths. In order to avoid confusion we always show paths where the BP comes from the top.

In some cases minimum energy paths are obtained which involve the creation of two BPs, one on each of the two surfaces (Fig. 6.10). The two BPs move into the core and annihilate in the center. However this minimum energy path gives a much higher energy barrier than the minimum energy path where just one BP is created. Thus, it is important to repeat the calcu-

lation with different initial guesses. Depending on the initial guess then either the one or the other of these two paths will be obtained.

Figure 6.9 shows the energy along the computed paths (energy vs. arc-length), at zero field and for different mesh sizes *d* in the central zone. The number of configurations along the path was 25. The initial configurations (vortices with the same rotation sense, but with opposite core magnetizations) were equilibrated first under the field that was applied. Then, the initial path was constructed by linear interpolation of all magnetization vectors. It means that the initial intermediate state is a 2D vortex (all vectors in the disk plane), with no core. The barrier energy for the initial paths is very high, ~6.2 10^{-18} J. The converged paths have much lower energy barrier. When no field is applied, the saddle point (top of barrier along the path) is a configuration with a BP sitting in the middle of the sample (see Fig. 6.8 and Fig. 6.12). When a field is applied, the saddle point is still a configuration with a BP. However the position is now not more in the middle of the sample, but shifted towards one of the surfaces (Fig. 6.12).

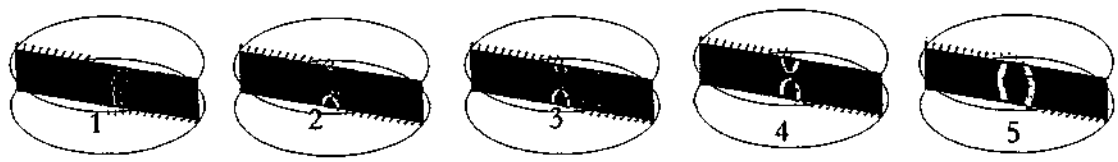

Figure 6.10 Minimum energy path for the reversal of a vortex core in a permalloy disk (50 nm thickness, 200 nm diameter) in zero external field. The displayed plane shows a cut through the disk center. The number of arrows does not correspond to the number of mesh points. The reversal path involves the creation of two BPs. The resulting energy barrier is thus higher than in a minimum energy path with a single BP.

In a next step an external field was applied. The Zeeman energy increases the energy of the antiparallel state, and decreases the energy of the parallel state. The energy barrier for the escape out of the metastable state decreases with increasing field. In order to emphasize this last feature, the energies during vortex core switching are plotted in Fig. 6.11 where the reference energy (zero energy) is that of the metastable state. The corresponding saddle point configurations are shown in Fig. 6.12. They all display one Bloch point. Its vertical position shifts from the center (B = 0) towards one surface. The surface can be either the top or bottom one, depending on how the path calculation breaks the symmetry, and indeed both situations were obtained. The BP shift can be understood by looking again at Fig. 6.11, thinking that the

horizontal axis now represents the vertical position of the BP. In a rough estimate the average magnetization in the field direction depends linearly on the BP position. The corresponding Zeeman energy adds a linear contribution to the total energy profiles. As a consequence the position of the maximum shifts linearly with the strength of the field towards either the one or the other surface (depending on the sign of the BP). When the barrier becomes close to zero, the barrier top state has a BP which is very close to the surface. The field at which the barrier reaches zero is the switching field of the vortex core.

It is now instructive to plot the calculated barriers versus the applied field (Fig. 6.13). The variation of the barrier with the field is of the form $c\,(H_s\text{-}H)^n$, where H_s has the meaning of a switching field. It can be obtained from an extrapolation of the curve in Fig. 6.13 to zero barrier. A good fit is obtained for $n = 2$. There is no justification of this law at present for general magnetization reversal processes, although similar forms are often used, sometimes with a different power than 2. Refining the mesh leads to an increase of the barriers, and thus to an increase of the extrapolated switching field H_s. Switching can be considered to occur in a reasonable time as soon as the barrier is below 10^{-19} J (~25 $k_B T_{amb}$). The switching field derived from extrapolation of the energy barriers to zero is similar to the switching field obtained from the quasistatic simulation of vortex core switching.

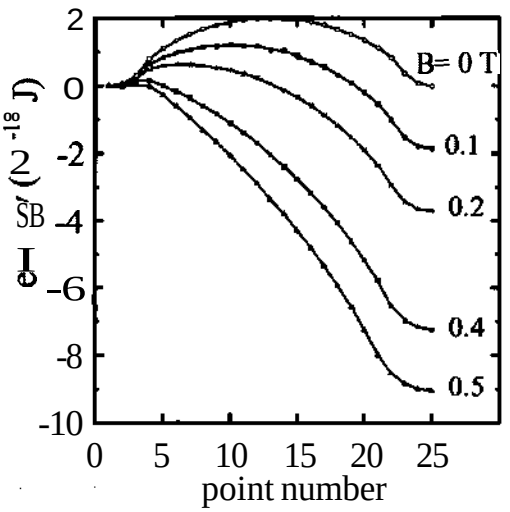

Figure 6.11 Calculated minimum energy paths for the reversal of the vortex core, for fields applied antiparallel to the core magnetization (induction values are indicated in T). The reference energy is that of the metastable state. The mesh in the central region is 2 nm. Sample dimension are same as in Fig. 6.9

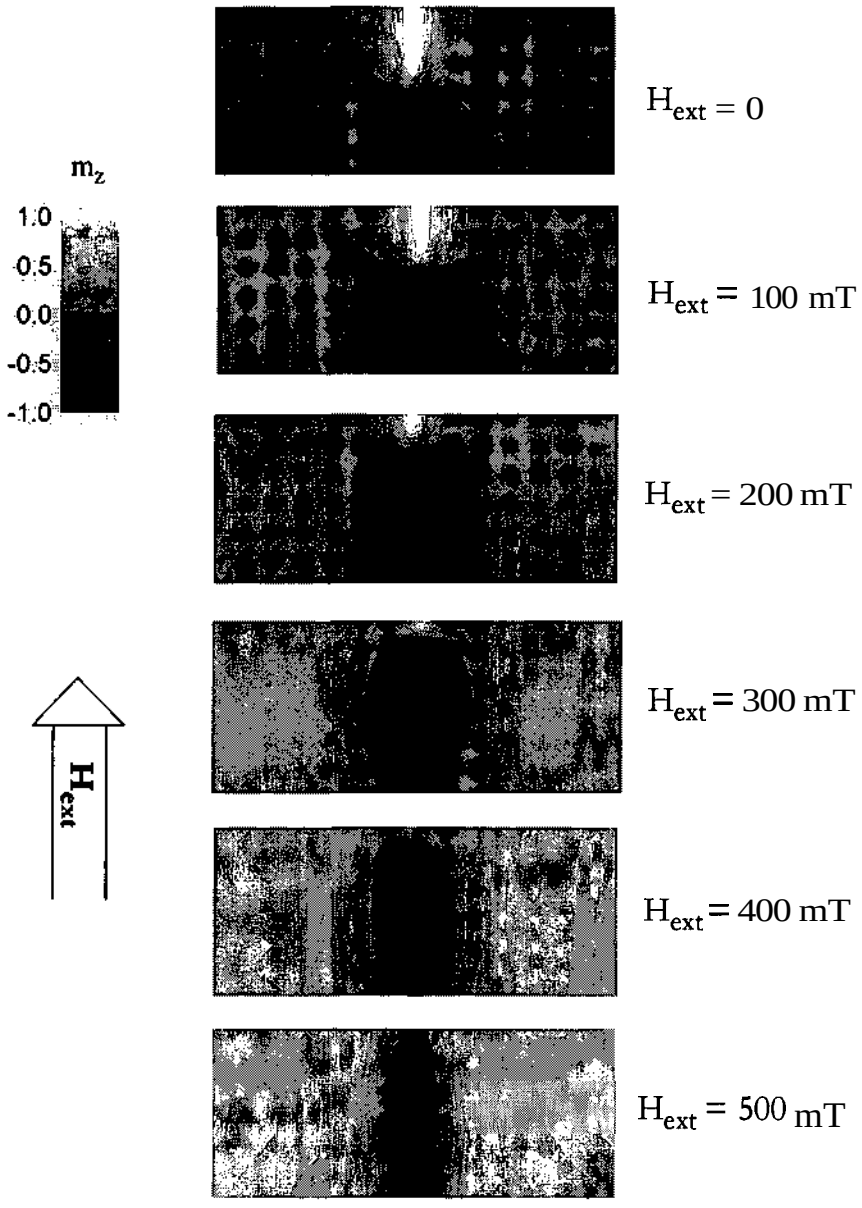

Figure 6.12 View (cut across the thickness) of the saddle point states under an applied field corresponding to Fig. 6.11. The image size is 100*50 nm, the field is oriented upwards and the shading relates to the z-component of the magnetization unit vector (initial core magnetization is down (dark)). The core mesh size is 2 nm. Note the progressive magnetization rotation outside the core as the field increases, and the displacement of the BP saddle point position towards the film surface.

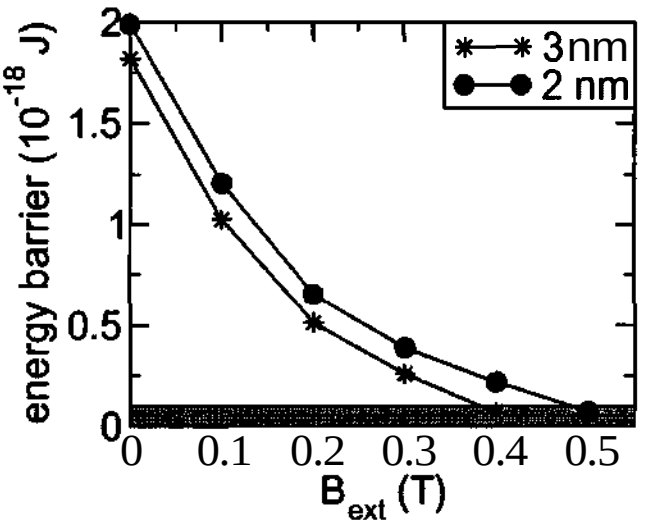

Figure 6.13 Plot of the energy barrier height versus the applied field, for two different core mesh sizes. The barrier decreases under the applied field roughly as a second order polynomial. The extrapolation to zero barrier height from the 4 height field points gives a switching field of $\mu_0 H_s = 490$ mT (3 nm) and 660 mT (2 nm). The shaded region corresponds to a barrier height below a thermal threshold (25 $k_B T$ at room temperature). Mesh refinement increases the calculated barriers and switching fields as seen before.

Aharoni's concern was: "you cannot let the computer decide when to jump" [4] when computing switching fields with numerical methods. Using the path method we visualize the energy barrier and can define the switching event as the field where the energy barrier has become smaller than a certain threshold value (see figure 6.13). This is justified since thermal fluctuations will drive the magnetization over the energy barrier within a certain relaxation time τ. Depending on the time scale of measurement and the temperature at which experiments are performed, the threshold value for the energy barrier is obtained using the Néel-Brown theory

$$f = f_0 exp\left(-\frac{E_{Barrier}}{k_B T}\right). \tag{6.4}$$

The energy barrier decreases with increasing opposing field. Thus, the threshold value for the energy barrier will give the switching field at non-zero temperature. At room temperature

we obtain the following threshold values of the energy barrier. The table gives the threshold values of the energy that defines the finite temperature switching field for three different measuring times, T = $1/f$. With f_0 - 1 ns^{-1} we get

$1k_BT, \quad f \sim 10^9 s^{-1}$

$15k_BT, \quad f \sim 99s^{-1}$

$20k_BT, \quad f \sim 2s^{-1}$

The measurements by Okuno et al. [79] were performed on a time scale of minutes. An energy barrier of 20 k_BT can be overcome with about 99% probability in the time of one minute. This allows a threshold for the energy barrier of at least 20 k_BT.

6.5 Mesh size dependency

The calculated switching fields depend on the mesh size in the vortex core region. With decreasing mesh size the exchange energy increases. As a result the obtained energy barriers also increase with decreasing mesh size. An example for the energy barrier as function of the mesh size in zero applied field is shown in Fig. 6.14 (B). The increase of the switching field with decreasing mesh size observed in the quasistatic calculations corresponds to the increase of the energy barrier with decreasing mesh size calculated with the nudged elastic band method. Since the energy barriers increased also the obtained switching field increases with decreasing mesh size (Fig. 6.14 (B)). The obtained switching fields are in the order of magnitude of the experimental values if a reasonable mesh size is used. The extrapolation to zero mesh size at room temperature predicts fields that are larger than the experimental values. Thus, the BP insertion is probably assisted by defects in the samples.

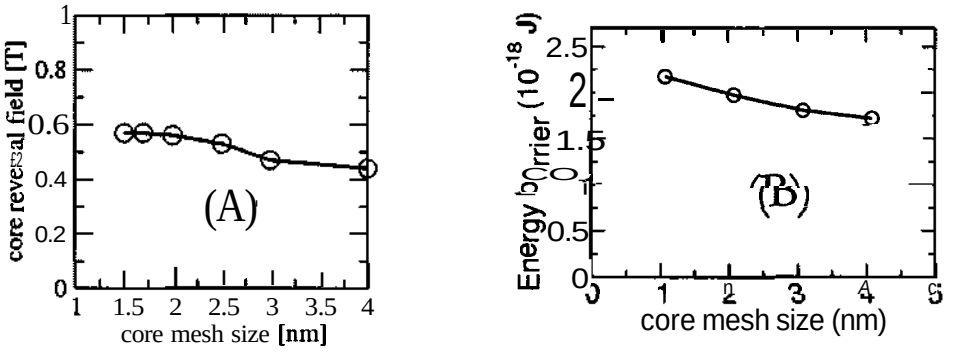

Figure 6.14 Effect of the mesh refinement on (A) the computed reversal fields by a quasistatic calculation and (B) the energy barrier at zero field. The disk diameter was 200 nm, thickness = 50 nm, permalloy parameters were used.

7 CONFIGURATIONAL AND SHAPE ANISOTROPY IN PERMALLOY PLATELETS

The nudged elastic band method is used to calculate minimum energy paths, global minima, metastable states and, most importantly, saddle points between energy minima of permalloy platelets. Configurational anisotropy effects in thin permalloy elements, e.g. 5 nm thick squares, are studied. For squares with the size of 15-200 nm the ground states are so called "leaf" states with the average magnetization along one of the diagonals. However a second state ("buckle") becomes stable with the average magnetization along one edge at sizes larger than ~80 nm. The superposition of the 4 easy axes leads to a combination of 4- and 8-fold anisotropy. At ~200 nm size both states have about the same energy so that the overall picture becomes that of an effective 8-fold in-plane configurational anisotropy. Good agreement is obtained when comparing the minimum energy paths, which represent the paths for thermally assisted switching, with the trajectories obtained from Langevin dynamics.

7.1 Introduction

Magnetic nanoelements form a strongly growing field with very promising future applications in magnetic storage devices such as MRAMs and sensor applications. While it is straightforward to calculate energy minima which represent stable magnetization configurations by minimizing the energy a much more demanding task is to compute the intermediate saddle point configurations between minimum energy configurations. The nudged elastic band method yields both local energy minima and saddle points. This gives us the energy barrier which determines how stable such a state remains against thermal fluctuations. In this chapter we focus on magnetic elements which have no in-plane shape anisotropy but only configurational anisotropy. Detailed experimental and theoretical work on configurational anisotropy has been performed by Cowburn [28]. Schabes and Bertram [89] investigated remanent states of small magnetic particles and possible reversal mechanisms.

To calculate minimum energy paths we use the nudged elastic band method. The detailed description of the method is found in section 4. Depending on the system more than one MEP can exist between two energy minima. Especially for larger sample sizes this can be the case. The MEP with the lowest energy barrier will then be preferred, which results from the exponential dependence on the energy barrier in the Néel-Brown equation [18]. For soft mag-

netic materials the only important energy contributions considered here are the exchange energy and the Zeeman energy. In a (meta)stable state the magnetic system occupies a local minimum of E - E_{exchange} + E_{Zeeman}.

7.2 Configurational anisotropy

Cowburn [28] performed experimental and theoretical work on thin soft magnetic elements as for example squares, triangles and pentagons. The geometries have a special property: They have no in-plane shape anisotropy and show only a so called configurational anisotropy. To explain what is meant with configurational anisotropy see figure 7.1. In elongated particles (rectangular thin prisms) the magnetostatic energy is lower when uniformly magnetized along the long axis than when magnetized along the short axis. This can be explained easily by just assuming perfectly uniform magnetization. In this case there are only magnetic surface charges and no volume charges. When magnetized along the long axes the distance between opposite charges is larger than in an element magnetized along the short axis. Thus, the energy of the sample that is magnetized along the long axis is lower than the energy of the sample magnetized along the short axis. For a squared platelet the situation is more complex. When assuming perfectly uniform magnetization the energy becomes independent of the direction of the in-plane magnetization (see figure 7.1). However small deviations from the uniformly magnetized state can lower the energy. The particle is small enough to be in a single domain state. However the non uniform demagnetizing field in turn causes a non uniform magnetization configuration. The "uniform magnetization" is replaced by "near-uniform magnetization". This unexpected complexity in the near single-domain regime was first pointed out by Schabes [89], and experimentally demonstrated for thin film elements by Cowburn [28,29]. For a square of 100 nm size and 5 nm thickness the so called "leaf states" are found to have the smallest energy with the average magnetization along the diagonals (see figure 7.1). In experiments [28] this effect is seen as an "effective anisotropy" which depends on the direction of the in-plane magnetization. This is shown in the left picture of figure 7.1. Due to the leaf state, the diagonals now behave like easy axes (blue regions) while directions along the edges are hard axes (yellow regions). In order to know how stable such minima are, we have to calculate the separating energy barriers between the minima. This means that we need to calculate the saddle points between the local energy minima.

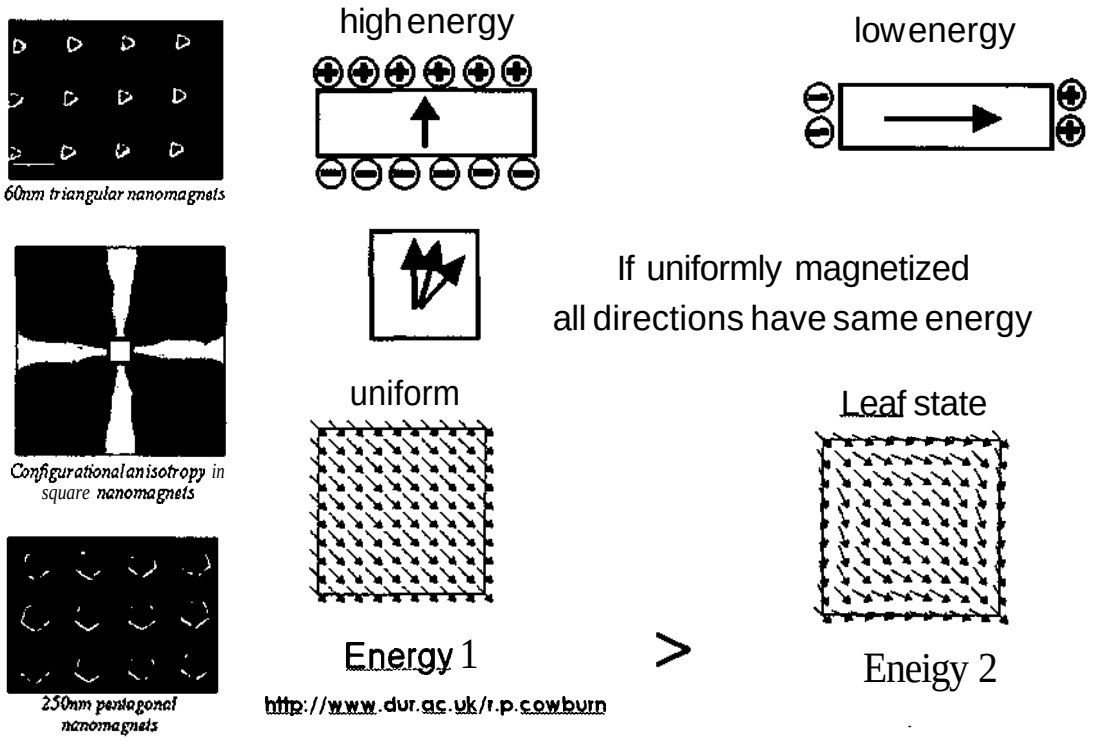

Figure 7.1 Configurational anisotropy in thin softmagnetic elements. In the single domain regime, the competition between exchange energy and magnetostatic energy requires that the uniform magnetization state changes to so called "near-uniform" magnetization. An example is the so called leaf state in thin squares. Experimentally [28] this effect is seen as an effective in-plane anisotropy which depends on the configuration of the magnetization.

7.3 Results

Configurational anisotropy effects in thin magnetic nanoelements are investigated. Quadratic and triangular elements have no in-plane shape anisotropy: If uniformly magnetized the energy of the system does not depend on the magnetization direction. However there is a so called Configurational anisotropy [28,29] which results from deviations of the magnetization from the homogeneous state. Starting from an initial guess we calculate minimum energy paths (MEPs) of the system. For the initial guess of the path we start by simply rotating the homogeneous magnetization state in-plane by 180° for squares and 120° for triangles. As an

alternative initial guess we rotate the magnetization by 180° in the plane perpendicular to the film which then typically results in a minimum energy path involving vortex motion. However, for squares this path has a much higher energy barrier for all sizes studied here (< 200 nm).

It is not necessary to calculate the equilibrium states (energy minima) in advance. As an illustration figure 7.2 shows this initial path and the MEP after optimization for a triangular element of 100 nm edge size and 5 nm thickness. The perfectly homogeneous state (=initial path) has a constant energy for all points along the path independent of the direction of the magnetization. After the optimization scheme we obtain the MEP which does not only reveal the equilibrium states already known [28] but also the saddle points between the minima (figure 7.2).

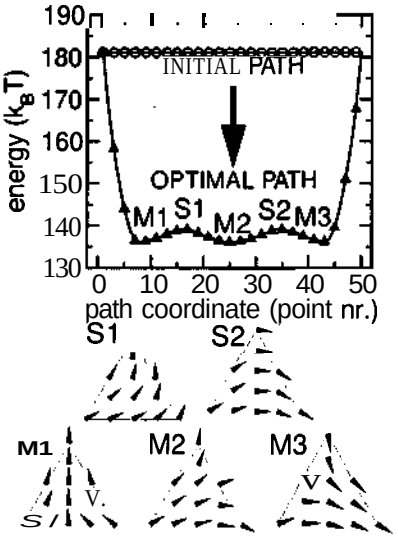

Figure 7.2 Initial path (circles) and optimal path (triangles) for a 100 nm triangular permalloy element of 5 nm thickness (number of mesh points N=5290). Minima and saddle points are labeled (M) and (S), respectively, and shown at the bottom of the figure. Note that the evolution from one state to the next proceeds by 90° rotation of the moments in the vicinity of one corner.

Fig. 7.3 shows an example for a minimum energy path calculation with the initial guess for a $100*100*5\,nm^3$ square. The two energy minima are the leaf states. As an initial guess we just rotate the uniform magnetization between these two states. As explained above, the energy does not depend on the direction of the magnetization as long as the magnetization is perfectly uniform. The red curve in figure 7.3 shows that the energy is constant along the initial path. After optimization we obtain the MEP. The energy along the MEP is shown in the black

curve in figure 7.3. The uniformly magnetized state along with the magnetization parallel to the edge would be a rough estimate for the saddle point. However, the calculated saddle points have lower energy than the homogeneous state. Thus, the energy barrier would have been strongly overestimated by a factor of about 2 when simply taking the energy barrier as the difference between the *energy of the uniform state* and the *energy of the minimum* instead of the difference between the *saddle point energy* and the *energy of the minimum.* As a second result we see that also a metastable C-state is occurs. A more detailed discussion on squared elements follows below.

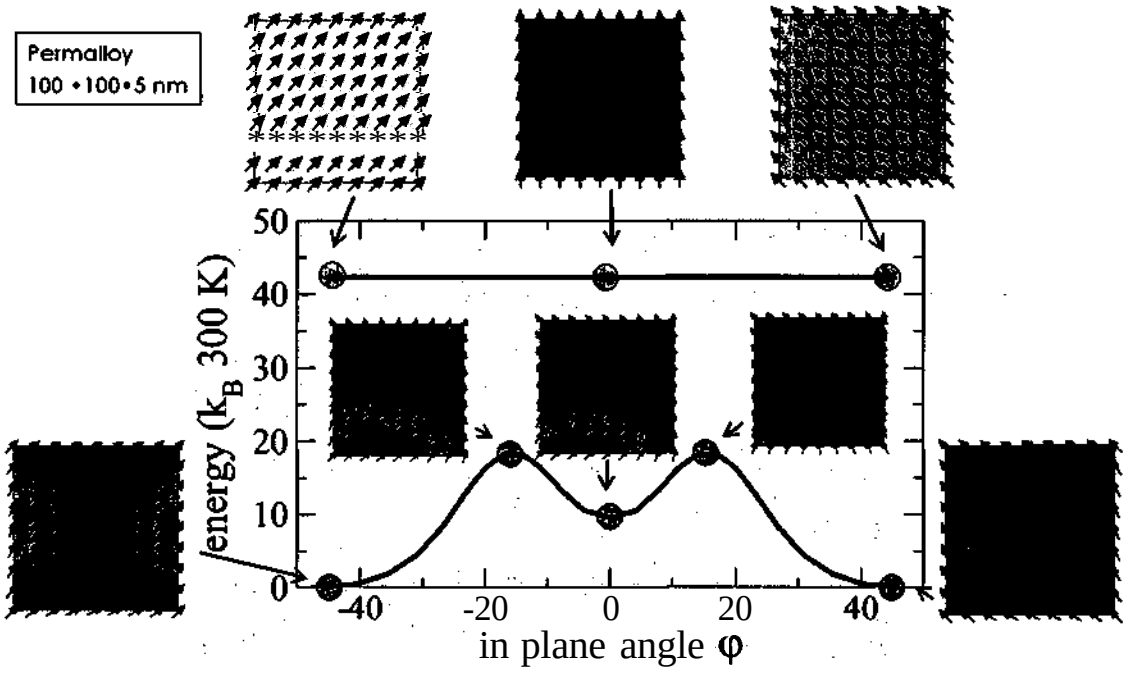

Figure 7.3 The initial guess (top 3 magnetization configurations and red curve) and the resulting minimum energy path (bottom 5 magnetization configurations and black energy curve). It is important to note that also the saddle point energies are below the energy of the perfectly uniform state. Thus, the energy barrier would have been strongly overestimated (43 k_BT instead of 19 k_BT) if calculated just as the difference between the energy of the uniform state and the energy of the leaf state (energy minimum). This shows the importance of a rigorous saddle point computation.

7.3.1 Quadratic elements

Quadratic permalloy platelets of 5 nm thickness were studied using an average mesh size of 2.5 nm. Four equilibrium states were found depending on the edge length. The possible

states (flower, leaf, buckle and vortex state) are shown in figure 7.4. The "leaf" state is called so because of the way that it blows out in the center and then nips together at the ends, like a plant leaf. Below a size of about 14 nm only the flower state is stable. The separating saddle points between the flower states were found to be leaf states. Above this critical size the situation reverses: The leaf states become stable while the flower states become saddle points. Increasing the size further, above 70 nm the buckle state appears as a metastable state. The saddle points evolve from flower states into more complex configurations (figure 7.7).

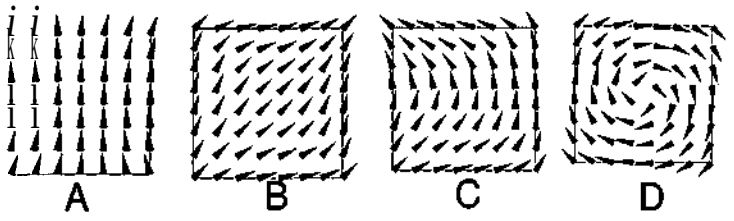

Figure 7.4 A) Flower, B) leaf, C) buckle and D) vortex state in a quadratic permalloy platelet.

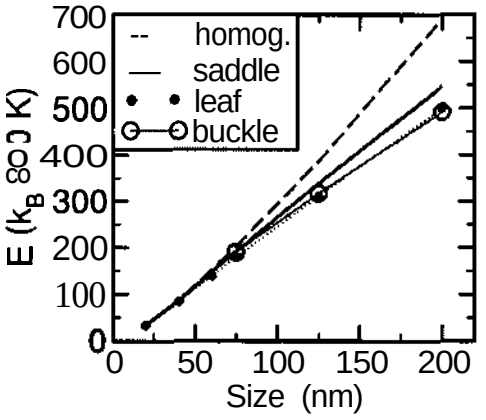

Figure 7.5 Total magnetic Gibbs free energy for a 5 nm thick quadratic platelet as a function of the element size for the 4 different states (leaf-, buckle-, homogeneous-state and saddle point).

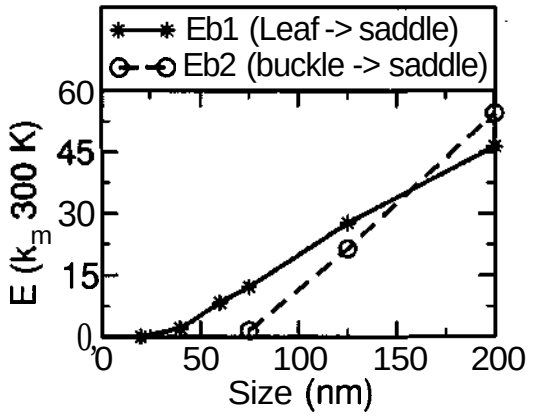

Figure 7.6 Energy barriers as a function of the element size for a 5 nm thick quadratic platelet. Eb1 is the energy barrier of the leaf state, Eb2 is the energy barrier of the buckle state.

Figure 7.5 shows that all states involved have lower energies than the homogeneous state. Fig. 7.5 also shows that the energy of the buckle state increases at a slightly lower rate than the energy of the leaf state with increasing element size. Thus, the energy barrier (buckle->leaf) increases with a higher slope than the energy barrier (leaf->buckle). Energy parity is obtained at ~ 150 nm element width. From the MEPs we calculate the energy barriers (Fig. 7.6).

Figure 7.7 shows the energy along the MEP for a lateral size of 200 nm. The equilibrium directions for the net average magnetization are located at 0°, 90°, 180° and at 270° for the buckle state and 45°, 135°, 225° and 315° for the leaf state. At 200 nm the energy barriers for the escape from the leaf state and from the buckle state are virtually identical. The overall picture thus becomes that of an 8 fold anisotropy (see Fig. 7.7) a feature overlooked in the previous studies [28].

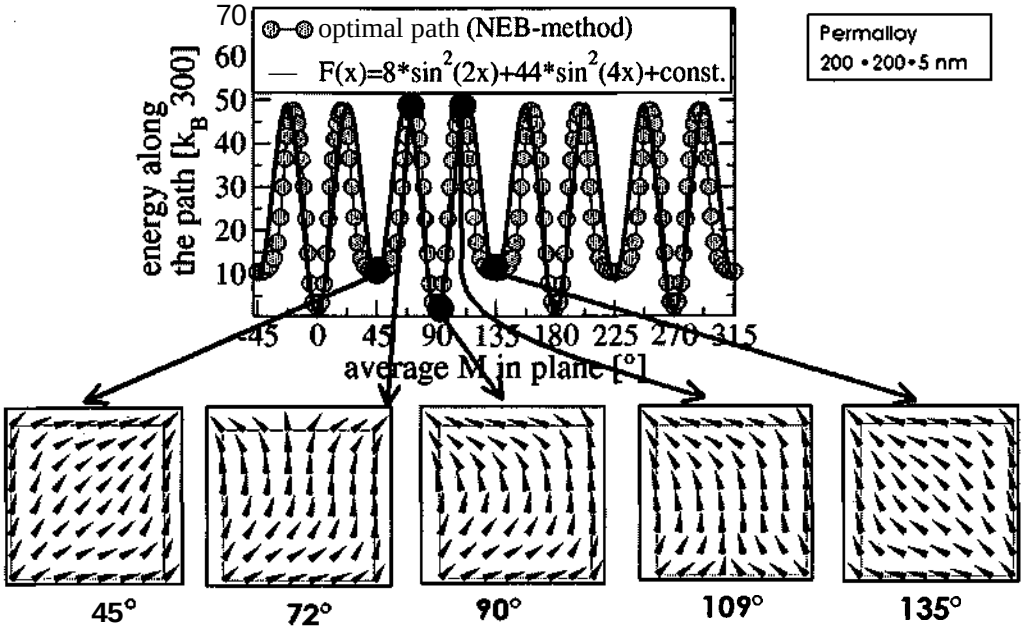

Figure 7.7 Energy along the optimal path with the characteristic magnetization states (minima and saddle points) for a 200 • 200 • 5 nm^3 square permalloy element showing the energy dependence versus the in-plane net magnetization direction. The bold solid curve corresponds to the formula.

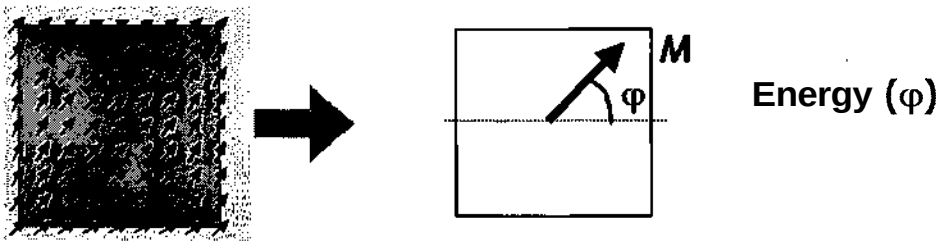

Figure 7.8 The results obtained with the NEB (see figure 7.7) can be used to simplify the model from a full finite element model to a macrospin model with a energy function that depends on the direction of the net in-plane magnetization.

Once the MEP is computed we know the energy as function of the net in-plane magnetization direction. With this information we can simplify the model as demonstrated in figure 7.8. Instead of a full finite element model a macrospin model with an energy function that depends on the direction of the net in-plane magnetization can be used. An application is the study of switching processes in the dynamic regime [77,8] using this simplified macrospin model.

As mentioned before the method always gives the MEP which is closest to the initial path. Starting with an initial path which is in-plane of the film we obtain a MEP which has the net magnetization in-plane. However if we start with the initial path in the plane perpendicular to the film we also obtain a path involving vortex motion with a vortex state as metastable state. Above sizes of 200 nm the energy of the vortex state becomes comparable with the energy of the buckle state. However the energy barrier to access the vortex state from the buckle state was found to be about 4 times higher than the energy barrier to access the leaf state from the buckle states. Therefore the "in-plane-MEP" is still preferred. It is possible (but not investigated in this work) that the "vortex-MEP" can become the path with the smallest barrier at sizes larger than 200 nm.

7.4 Thermal switching

As an application we compare the path method with Langevin simulations (see figure 7.9) for a $90 \cdot 90 \cdot 4.5\ nm^3$ square. First we calculate the minimum energy path between two leaf states. The graph shows the energy along this path. The energy is normalized to the energy of the leaf state and expressed in terms of k_BT for a temperature of 450 K. Two barriers have to be overcome and a metastable C-state is visited in between. The configurations along this path are shown in the top sequence in figure 7.9: The initial leaf state, the first saddle, the metastable C-state, the second saddle, and the final leaf state. But does this path really represent the path that will be taken during a thermally induced switching event? We perform a thermal waiting time experiment using Langevin dynamics. We start with a leaf state and wait for a spontaneous thermal switching event to occur. The bottom sequence in figure 7.9 shows such a switching event. The in-plane angle of the magnetization is plotted versus the time. The magnetization precesses around the ground state (leaf at 45°). At some point the oscillations get large enough and the magnetization switches to another leaf state. Comparing the

The waiting time to escape from the C-state is much smaller than the switching time between the leaf states. This becomes clear by looking at the energy barriers (see fig. 7.9): The energy barrier ΔE_1 is much smaller than the energy barrier ΔE_2. To demonstrate this difference in waiting times we perform a second Langevin simulation at much smaller temperature and we start in the metastable C-state (see figure 7.10).

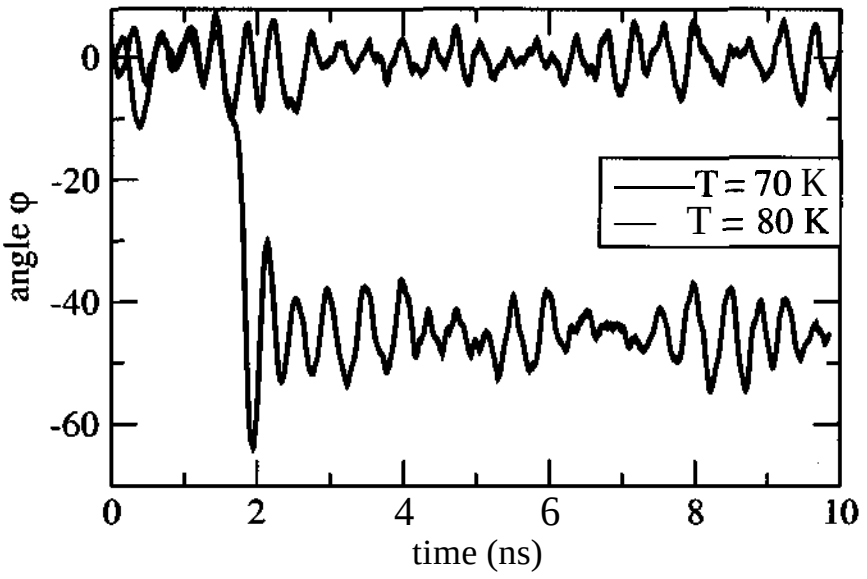

Figure 7.10 Thermal switching from a metastable C-state (9=0°) to the leaf-ground state for a 90 • 90 • 4.5 nm^3 permalloy square at T = 70 and 80 K. The figure shows the direction of the net in-plane magnetization as function of the time. At T = 70 K the energy barrier is higher than for 80 K and no switching (escape) is observed within 10 ns. At T = 80 K the magnetization switches and then stays near the ground state (leaf, 9=45°) since the temperature is too small to induce an escape from this state within the time scale studied here (10 ns).

The energy barrier to escape from the C-state at T=80 K is 5 k_BT and 5.7 k_BT for T = 70 K, while the energy barrier to escape from the leaf state is 34 k_BT at T = 80 K. According to the Néel-Brown equation for the transition rates in the case of high energy barriers ($E_B > 1\ k_BT$)

$$f = f_0 exp\left(-\frac{E_{Barrier}}{k_B T}\right) \tag{7.1}$$

magnetization states we see that the trajectory calculated by Langevin dynamics indeed passes the saddle points and the C-state as predicted with the nudged elastic band method.

To point out: The first path (top sequence in Fig. 7.9) was found just from geometrical aspects of the energy landscape using the nudged elastic band method, while for the second path (bottom sequence in Fig. 7.9) the stochastic differential equation of motion was integrated at a finite temperature. The advantage of the path method is that is generally applicable also to large scale systems with high energy barriers while the Langevin waiting time experiment is limited to small problems with small barriers and short time scales (some nanoseconds).

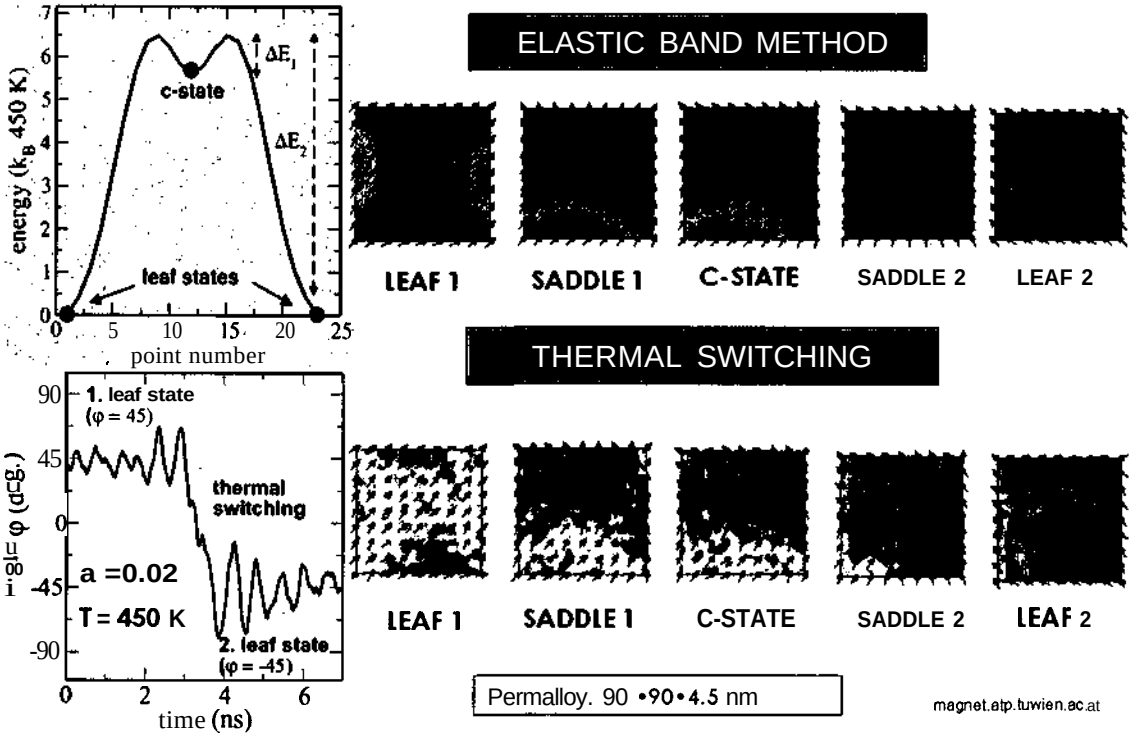

Figure 7.9 Comparison of the results obtained with the nudged elastic band method (top sequence) with a trajectory calculated by Langevin simulation (bottom sequence). Shown are magnetization states along the minimum energy path and the energy along this path. The energy barrier ΔE_1 is much smaller than the energy barrier ΔE_2. Thus, the waiting time to escape from the C-state is much smaller than the switching time between the leaf states. The magnetization states obtained with Langevin dynamics are in good agreement with the results obtained with the nudged elastic band method.

the transition frequency becomes/= 0.6 ns^{-1} when assuming a prefactor f_0 = 100 ns^{-1} for T = 80 K and E_B=5 $k_B T$. To escape from the leaf state a much higher energy barrier has to be overcome (34 $k_B T$). For T = 80 K this gives a transition frequency $f = 17 \cdot 10^{**}$ ns"* = 472 hour"' . The switching events would occur at the time scale of hours. The probability to observe such an event at the timescale of 10 ns is therefore very small and the magnetization stays near the ground state (leaf) after this state has been reached by switching from the C-state. At T = 70 K the transition frequencies are only half of the values at 80 K. In the simulation shown in Fig. 7.10 we do not observe an escape from the C-state in this case. For more quantitative analysis of this problem many repetitions of the simulation for different temperatures would be needed. Statistical quantities as the prefactor f_0 can then be calculated by averaging over the values in the sampled simulations. A more detailed study on this topic is presented in chapter 10.

8 THERMALLY INDUCED MAGNETIZATION REVERSAL IN AFC MEDIA.

The nudged elastic band method is applied to calculate optimal paths for the thermal switching in AFC media. Energy barriers and transition rates can be estimated from the saddle points and the energy minima along the minimum energy path. We investigate the dependence of the energy barrier on the strength of the antiferromagnetic coupling and study the reversal in the data bit transition region. Below a coupling strength of 1.1 mJ/m^2 a two step reversal occurs as the system passes a metastable state. Above a coupling strength of 1.1 mJ/m^2 this metastable state disappears. The energy barrier is constant for a coupling strength greater than 1.5 mJ/m^2.

8.1 Introduction

AFC media is a prominent candidate where thermal stability is increased by a stabilizing layer [52,66]. As described in the previous sections the calculation of thermal stability requires a detailed characterization of the energy landscape. To obtain the transition states one needs to calculate saddle points between stable states (energy minima). While it is straightforward to calculate energy minima a much more demanding task is to find the saddle points between the minima. Even for low dimensional models e.g. a macrospin model for AFC media where two spins are exchange coupled this calculation [87] is quite complex although it has just 4 degrees of freedom. We use the nudged elastic band method to calculate saddle points and energy barriers. We start with one irregularly shaped AFC grain (figure 8.1 B) discretized with about 800 nodes. In a next step the energy barrier for a grain in the data bit transition region was calculated in a model with 25 irregularly shaped AFC grains (figure 8.1 A) with a tetrahedral mesh of $\sim$5000 nodes.

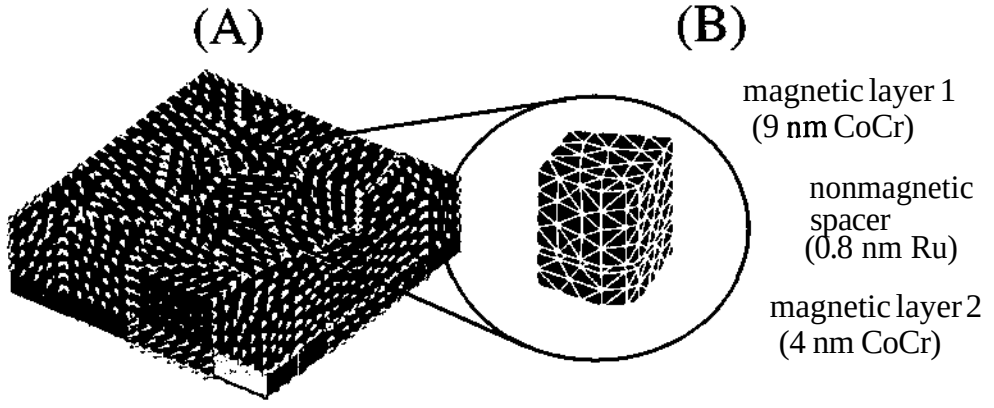

Figure 8.1 A) 25 AFC grains with random anisotropy axes in-plane. B) The interface area of the enlarged AFC grain is 96.15 nm^2. V_1 and V_2 are the volumes of the top and bottom layer grains. (V_1 = 865 nm^3, V_2 = 385 nm^3). The figure shows the surface triangles of the finite element mesh used in the calculations.

8.2 Results

Fig. 8.1 shows the model used in our calculations. The recording layer and the stabilizing layer are separated by a thin nonmagnetic Ru-spacer of about 0.8 nm thickness which couples the two layers antiferromagnetically. For an interface area of 96.15 nm^2 and a coupling strength up to 5 mJ/m^2 this gives energies up to 48 k_BT. The magnetic material is assumed to have uniaxially magnetocrystalline anisotropy with the easy axes oriented in the film plane. The magnetic films are grown epitaxial, therefore the bottom and top layer have the same easy axis orientations. However the magnetic materials can be different in the bottom and top layer. In this work we use the same material properties for both layers.

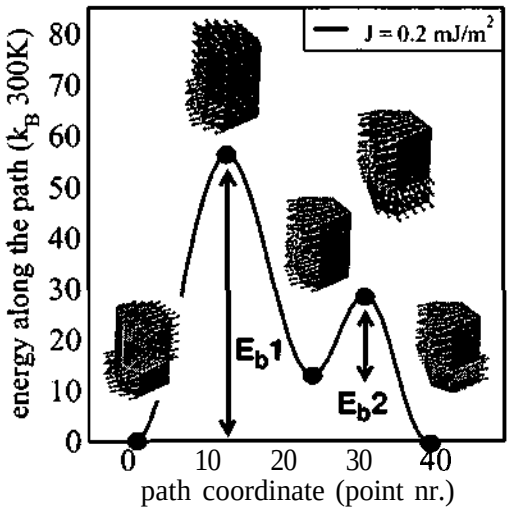

Figure 8.2 Energy along the optimal path for an exchange coupling $J=0.2\,mJ/m^2$ (J^*Area ~ 4.8 k_BT). The magnetization reverses by a two step process passing two energy barriers. Energy barriers and magnetization states are indicated in the figure.

We start by investigating the dependence of the energy barrier on the interface coupling strength for an isolated irregularly shaped AFC grain as shown in figure 8.1 B. As a basic set of parameters we choose the following values: $A_{bulk} = 10$ pJ/m, $J_{s1} = J_{s2} = 0.375$T and $K_{u1} = K_{u2}$ - 2.3 x 10^{5} J/m^{3}. For the top grain this gives a uniaxial anisotropy energy of about 50 k_BT. For weak coupling ($J <$ 1.1 mJ/m^2) a two step reversal occurs. First one layer reverses and the system remains in a metastable state where both grains are parallel until the second layer switches. The two step reversal mode is shown in figure 8.2. The energy barrier increases linearly with the coupling strength reaching 1.41 K_uV_1 at about 1 mJ/m^2. K_u is the uniaxial anisotropy and V_1 and V_2 are the volumes of the two subunits (see figure 8.1 B). Above a critical coupling strength of 1.1 mJ/m^2 the metastable state disappears (see figure 8.3). Above this critical value the interface coupling energy exceeds the energy for uniform rotation of the smaller grain. For thinner bottom layers a smaller coupling strength is sufficient to reach this

critical point. The energy barrier still increases with the coupling strength reaching 1.45 $K_u V_1$, at J ~ 2 mJ/m^2. Above this value saturation is reached (figure 8.3).

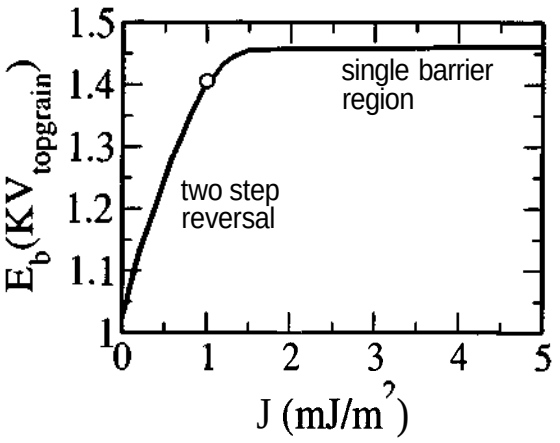

Figure 8.3 Energy barrier as a function of the interface coupling strength for one isolated AFC grain. The point indicates the critical coupling strength which separates the two- and the one-step reversal mode. V_1 and V_2 are the volumes of the top and bottom layer grains. (K_u= 230 kJ/m^3, V_1= 865 nm^3, V_2= 385 nm^3)

For high quality recording media a high energy barrier alone is not sufficient. This could be achieved by simply increasing the anisotropy in conventional media. The second important quality factor is the writeability of the media since the recording head has a limited writing field. The desired media should have a low switching field but keep a high energy barrier. In a second step we calculate the switching fields using standard dynamic micromagnetics [103]. The reversing field is applied in-plane under an angle of 21° [86] to the easy axis of the grain. The results are shown in figure 8.4. We compare the switching field H_c of conventional media with AFC media as a function of the corresponding energy barrier. In the case of conventional media (using the top layer grain only in our AFC model) we increased the energy barrier by varying (increasing) the anisotropy constant K_u (starting from 230 kJ/m^3). In AFC media the energy barrier is increased by varying (increasing) the interface coupling strength but keeping the anisotropy (K_u = 230 kJ/m^3) constant. The dashed line shows that the energy barrier of AFC media can be increased by 15% as compared to conventional media without increasing the switching field H_c. This best gain corresponds exactly to the interface coupling strength in the AFC media at which the reversal mode changes from two step to one step

reversal (see figure 8.3 and 8.4). Here the interface coupling energy is about 110% of the anisotropy energy of the bottom layer. The situation is further illustrated in fig. 8.6 where the ratio of the energy barrier and the switching is plotted as a function of the interlayer coupling strength.

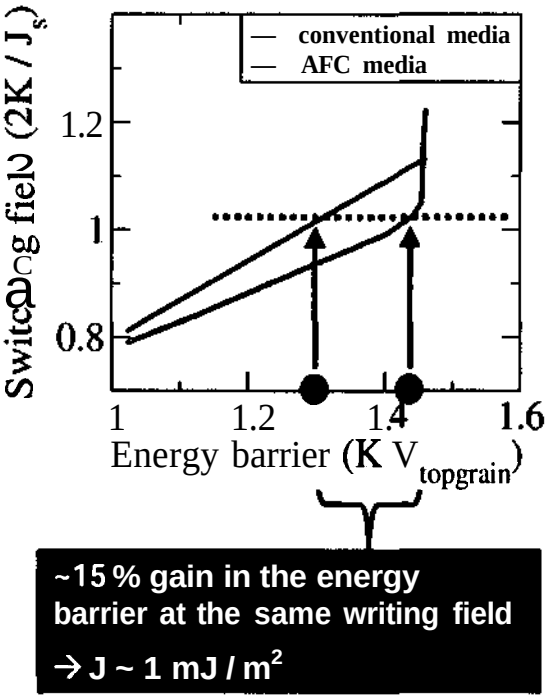

Figure 8.4 Switching field as a function of the energy barrier. Compared are conventional media with AFC media. The reversing field is applied 21° [86] to the easy axis. From the horizontal line we see that the energy barrier of the AFC media is 15% higher than the one of conventional media at the same switching (writing) field.

The method also allows the calculation of more complex models. We constructed a model of 25 irregularly shaped AFC grains. The average grain diameter was 9 nm and with 0.9 nm thick non magnetic grain boundaries in between. The top and bottom layer had equal parameters as in the example of the single grain. The energy barrier was calculated for a grain in the data bit transition region as shown in figure 8.5. Although the model is complex and the dimension of the discretization space high the method gives the proper saddle point and corresponding energy barrier in a reasonable computing time (1/2 day, when meshed with 5 000 nodes) on a single processor desktop computer. The calculated energy barriers differ only

slightly from the energy barrier of the isolated grain and are about 3% smaller. This is explained by the demagnetizing field in the transition region (figure 8.5).

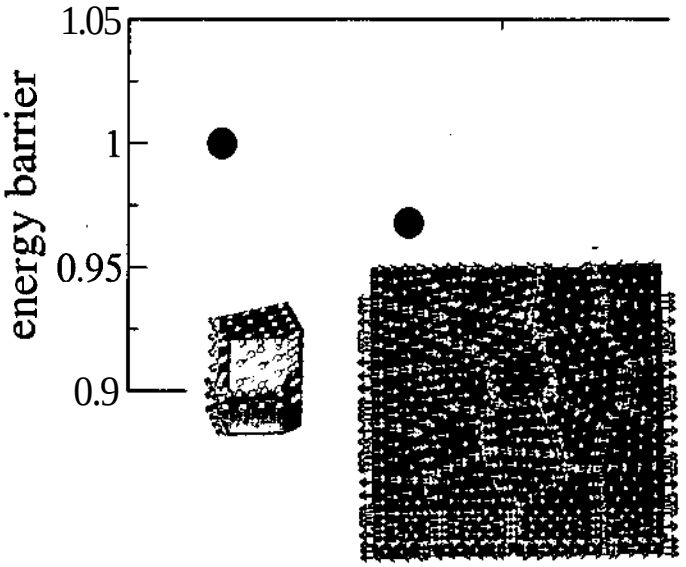

Figure 8.5 Comparison of the energy barrier for the thermal reversal of an AFC grain. When located in the transition region (right) of a data bit, the barrier is 3% smaller than for a completely isolated grain (left).

In a last step we compared our results that we obtained with a micromagnetic model using sub-grain discretization with a simpler model where each grain is assumed to be single domain (macrospin model). Fig. 8.7 shows a snapshot of the magnetization during the thermal reversal for a coupling strength of 1 mJ/m^2. The top grain shows a slight deviation of the magnetization from the perfectly uniform state. Thus, some part of the total energy can be stored in the bulk exchange energy (5% here). This means that it is important to use subgrain discretized models in order to obtain a high accuracy estimate of the energy barrier. The simplified macrospin model overestimates the energy barrier by some percent. Note that due to the exponential nature of the Néel-Brown equation for the calculation of transition rates, small errors in the energy barrier can already give significant deviations in the calculated transition rates.

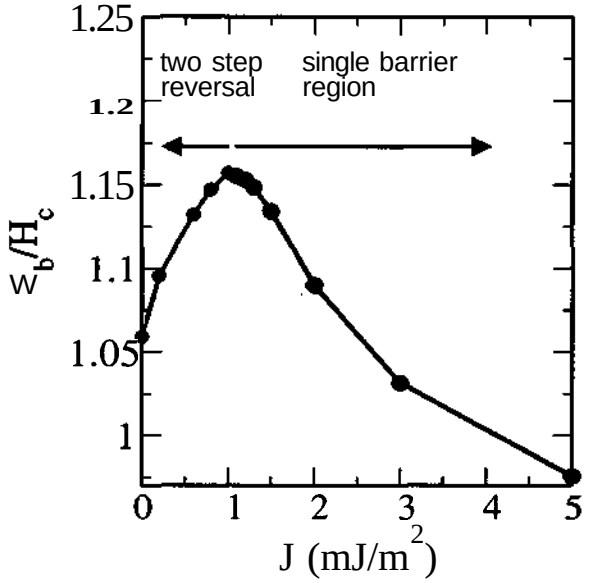

Figure 8.6 Ratio of the energy barrier and the coercive field as function of the interface coupling strength. For conventional media this would be a horizontal line. This means that the barrier increases at the same rate as the switching field. In AFC media there is a trade-off. The maximum in the curve gives the optimal working point for AFC media. At this point we have a high energy barrier but at the same time a low switching field.

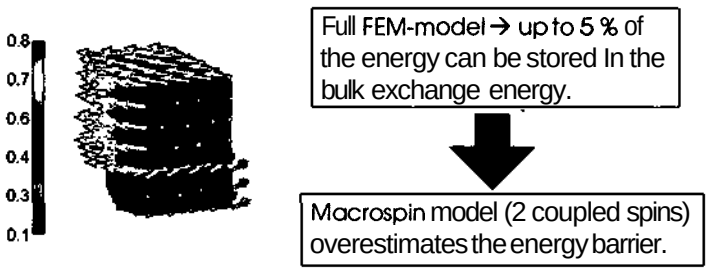

Figure 8.7 Snapshot of the magnetization during the thermal reversal for a coupling strength of 1 mJ/m^2. The top grain shows a slight deviation of the magnetization from the perfectly uniform state. Thus, some part of the total energy can be stored in the bulk exchange energy (5% here). The color code maps the in-plane magnetization direction along the easy axis.

9 ENERGY BARRIERS IN MAGNETIC RANDOM ACCESS MEMORY ELEMENTS

Minimum energy paths and energy barriers are calculated for the free data layer in elliptical magnetic random access memory elements using the nudged elastic band method. The reversal mode in the minimum energy path depends on the strength of the external field. With increasing easy axis field the reversal mode becomes more inhomogeneous than at lower fields. Even at small sizes inhomogeneous modes are found.

9.1 Introduction

The energy barrier between stable configurations determines the probability of a thermal switching event. In MRAM elements the energy barrier is determined by the shape of the element ("shape anisotropy") and the induced crystalline anisotropy. This should guarantee a lifetime of a stored bit of about 10 years. We calculate energy barriers for elliptical MRAM elements using the nudged elastic band method (NEB) [56]. This method finds minimum energy paths in high dimensional energy landscapes and is a rigorous way to compute the saddle point(s) between local energy minima.

Previous studies [72] on thermal effects in MRAMs are based on Langevin dynamics. A field near the switching field must be applied in order to decrease the energy barrier and to observe thermal switching of the magnetization. Using the nudged elastic band method we can calculate energy barriers also for zero applied external field.

9.2 Model of the free data layer

Our models of the free layer of the MRAM cell are based on an experimental work [88], which studies the thermal reversal of elliptical NiFeCo MRAM elements. We calculated minimum energy paths (MEP) as a function of the external in-plane field which is smaller than the zero temperature switching field. Material parameters of NiFeCo [65] were used (J_s=1.068 T, A=10 pJ/m, K=510 J/m^3) with the easy axis along the long axis of the element. We varied the size of the elements starting with an element of 1120 x 400 nm^2 size and decreasing the size

down to 62.5 x 25 nm^2. Aspect ratio (2:5) and thickness (4 nm) were kept constant. Fig. 9.1 shows a top view of the model with three possible paths for a 1120 nm element.

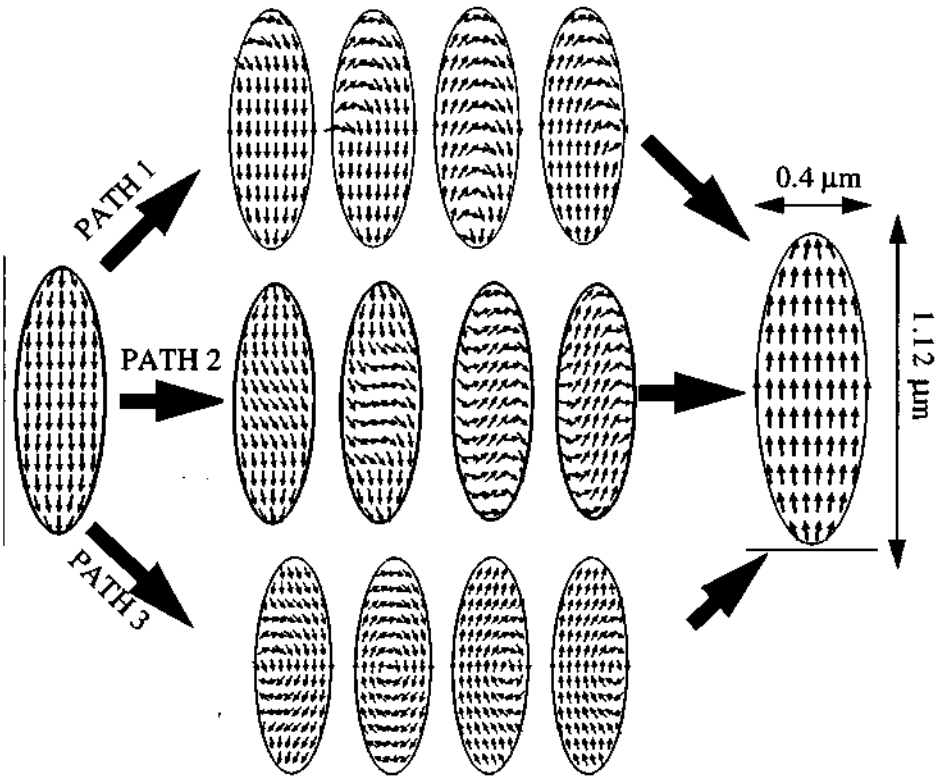

Figure 9.1 Three minimum energy paths for the thermal reversal of a 4 nm thin NiFeCo MRAM element are found between the two stable magnetization states. An opposing field is applied along the easy axis (= long axis of the cell). In paths 1 and 2 the magnetization stays in-pkne crossing a single barrier. In path 3 a two step reversal mode is found passing a metastable state (vortex in the center). For an applied field in the range 0-15 Oe path 3 has the lowest barrier. From 15-80 Oe path 1 has the lowest barrier and above 80 Oe path 2 has the lowest barrier (see figure 9.2). The zero temperature switching field in a quasistatic calculation is 94 Oe.

9.3 Reversal modes at 1.12 μm size

By varying the field strength along the easy-axis three minimum energy paths are found (Fig. 9.1) for a particle size of 1.12 μm. Two of them show a single energy barrier where the magnetization reverses by inhomogeneous rotation in the film plane (path 1 and path 2 in Fig. 9.1). The third mode is a two-step reversal which has a metastable state where a vortex is in the center of the element (path 3 in Fig. 9.1).

A dynamic hysteresis calculation (integration of the Landau-Lifshitz Gilbert equation using a Gilbert damping constant of $\alpha = 1$) [103] gives a zero temperature switching field of 94 Oe. The underlying reversal mode during the switching driven by an external easy-axis field larger than 94 Oe is similar to the mode of path 2 in Fig. 9.1. This is in agreement with the following observation: At a field strength of $H < 15$ Oe the mode path 3 has the lowest barrier while for $H > 15$ Oe the mode of path 1 becomes favorable. Above 80 Oe we are already close to the zero temperature switching field and the mode of path 2 becomes the mode with the smallest energy barrier. Fig. 9.2 shows the energy barriers of the tree paths as a function of the applied field.

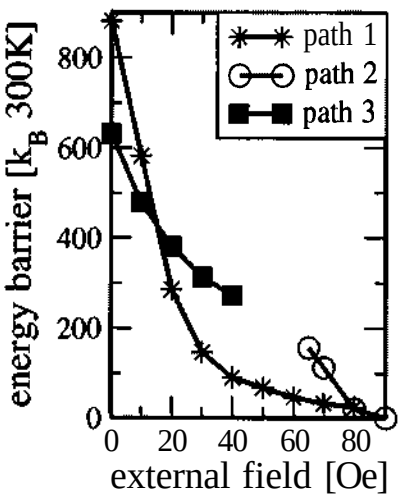

Figure 9.2 Energy barrier as a function of the easy-axis field strength for 1.12 μm particle size (figure 9.1). The underlying thermal reversal mode (paths) depend on the strength of the external field. In Paths 1 and 2 the magnetization stays in-pkne crossing a single barrier. In path 3 a two step reversal mode is found passing a metastable state (vortex in the center).

9.4 Variation of the particle size

Fig. 9.3A and 9.3B show the size dependence of the energy barrier when an easy-axis field is applied. The extrapolation to the zero barrier height (Fig. 9.3A) gives a switching field that agrees with the value obtained in the dynamic calculation of the switching fields (Fig. 9.4A). At zero external field the energy barrier depends almost linearly on the square root of the area of the top surface of the element (Fig. 9.3B).

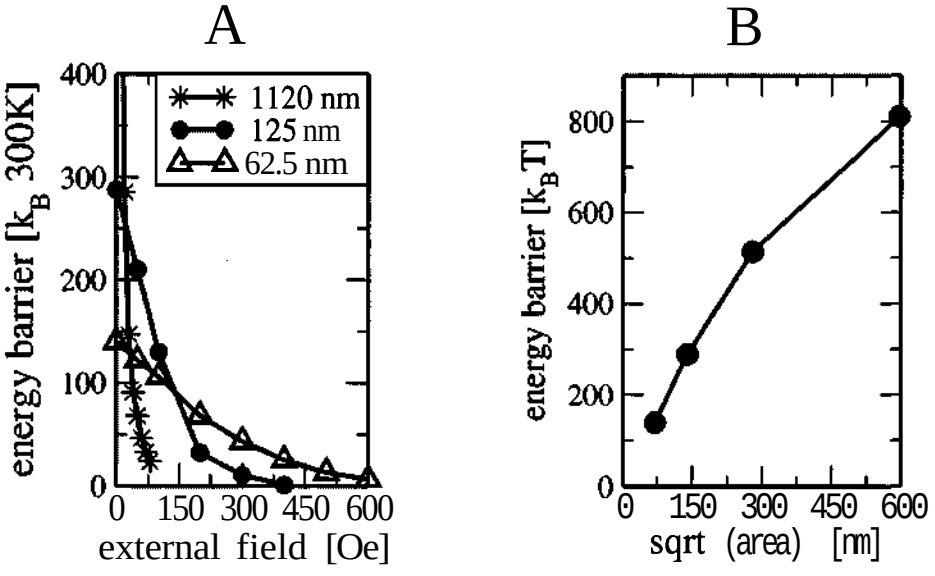

Figure 9.3 A) Energy barrier as a function of the easy-axis field strength for different particle size. The extrapolation to zero barrier height gives the switching field. B) Energy barrier at zero external field as a function of the particle size (given as the square root of the surface area). Thickness (4 nm) and aspect ratio (2:5) are fixed as in figure 9.1 The energy barrier depends close to linearly on the square root of the area of the MRAM element.

9.5 Stability of half selected cells

Fig. 9.4 shows that the lowest switching fields are obtained when applying the field in-plane at about 45° to the easy axis (see Fig. 9.4). At 1.12 μm size of the long axis this corresponds to a hard axis and easy axis field of 43 Oe (both a 43 Oe easy axis field and a 43 Oe hard axis field are applied to obtain the 45° in-plane field). To ensure thermal stability the

magnetization must stay stable when applying either a hard- of or an easy-axis field of this strength. At an easy-axis field of 43 Oe the energy barrier is 75 k_B300K (Fig. 9.3) which is high enough to ensure stability in the range of decades.

For hard-axis fields the situation was found to be less critical. Fig 9.5 compares the energy barrier dependence of half selected cells on the external field for a particle size of 125 nm. The lowest switching field (Fig. 9.4) is obtained with a superposition of a 148 Oe hard-axis field and 148 Oe easy-axis field. The energy barrier is about 140 k_B300K for a hard axis field of 148 Oe and 80 k_B300K for an easy axis field of 148 Oe (see Fig. 9.5). Also note that the thermal stability is more critical when the field is applied opposite to the easy axis than when applied perpendicular to it.

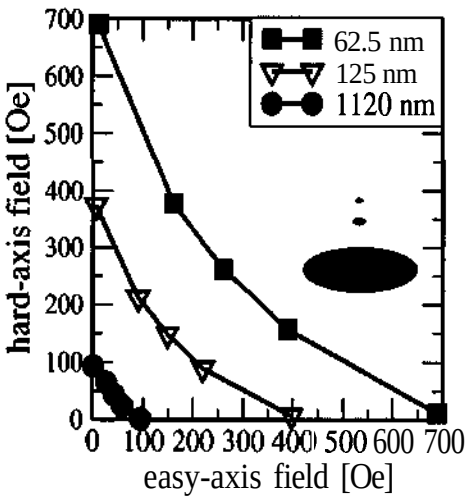

Figure 9.4 Switching astroid obtained in a quasistatic calculation for three different sizes of a 4 nm thin elliptical MRAM element of aspect ratio 2:5. The given *size* is the length of the long axis.

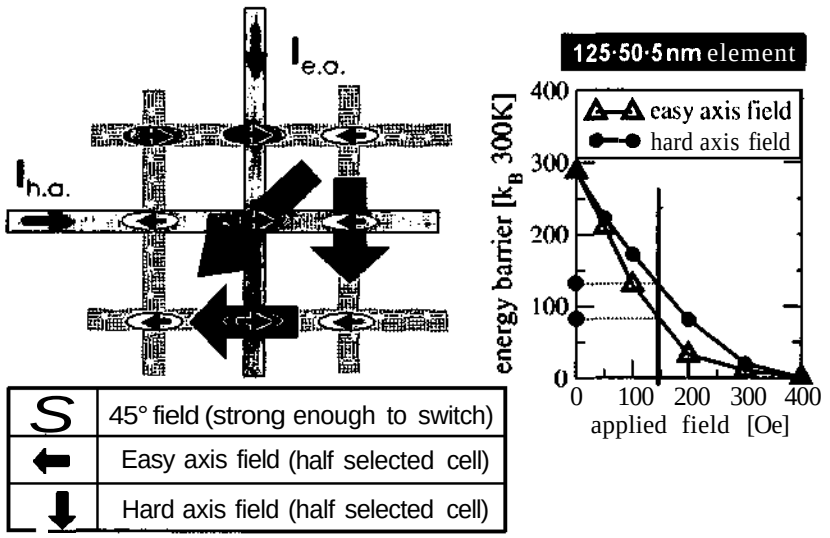

Figure 9.5 left) Array of MRAM cells with current lines. To switch the center cell a current is applied in the two red colored current lines. The resulting field (red arrow) is strong enough to switch the magnetization. Half selected cells feel a weaker field (blue arrows) either parallel or perpendicular to the easy axis. right) Energy barrier as a function of the applied field strength for the half selected cells with a size of 125 nm. The blue line corresponds to the field strength when a switching current is applied. Applying an easy-axis field is more critical for the stability than when applying a hard-axis field.

In the case studied above, the energy barrier (~100 k_BT) would be sufficient to guarantee the thermal stability over the lifetime of an MRAM device. In practice the situation is more critical since the production process gives deviations in the properties of the individual MRAM cells from their desired specifications. Variations in size, shape, magnetic properties and roughness will result in a spread of the switching field and energy barrier distribution (figure 9.6). A larger spread in the distribution leads to a much stricter requirement on the energy barrier. This is explained by the following two arguments:

- Due to the distribution of the switching fields, higher fields are needed in order to switch the strongest MRAM cells.
- On the other hand also the weakest MRAM cells must stay stable at applied external fields during time when they are half selected.

These two arguments together result in a very strict requirement for the average energy barrier height.

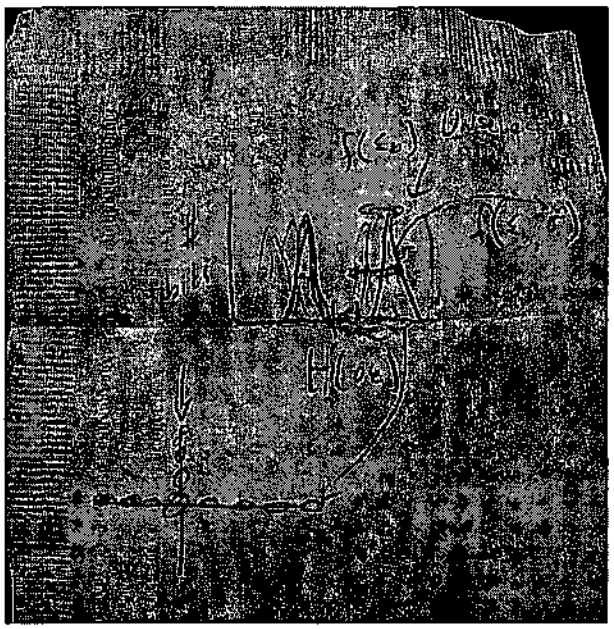

Figure 9.6 Switching field distribution. The first peak shows the switching field distribution for half selected cells. The second peak is the switching field distribution for unselected cells. Deviations of geometry, size, material properties and surface roughness result in a variation of the switching field and energy barrier distribution. [68]

9.6 Field dependence of the reversal mode

As shown above the reversal modes found in minimum energy paths depend on the field strength and direction of the field. For the large element we found three paths as shown in Fig. 9.1 and 9.2. Even more surprising we also see this for the smallest particle studied (62.5 nm). One would expect that the reversal mode would be close to homogeneous rotation at this size. Indeed, magnetization reversal by core rotation occurs in the case when no field is applied. At stronger easy-axis fields however (above 150 Oe), the mode changes to an inhomogeneous reversal involving domain wall motion similar to the mode of path 1 in Fig. 9.1. Now, the domain wall is oriented along the short axis (figure 9.7 left). Fig. 9.8 shows the energy along the minimum energy paths for the 62.5 nm element as a function of the

arclength. The reference energy (zero point) is the energy of the initial (non-reversed) state. The external fields of different strength are applied parallel to the easy axis.

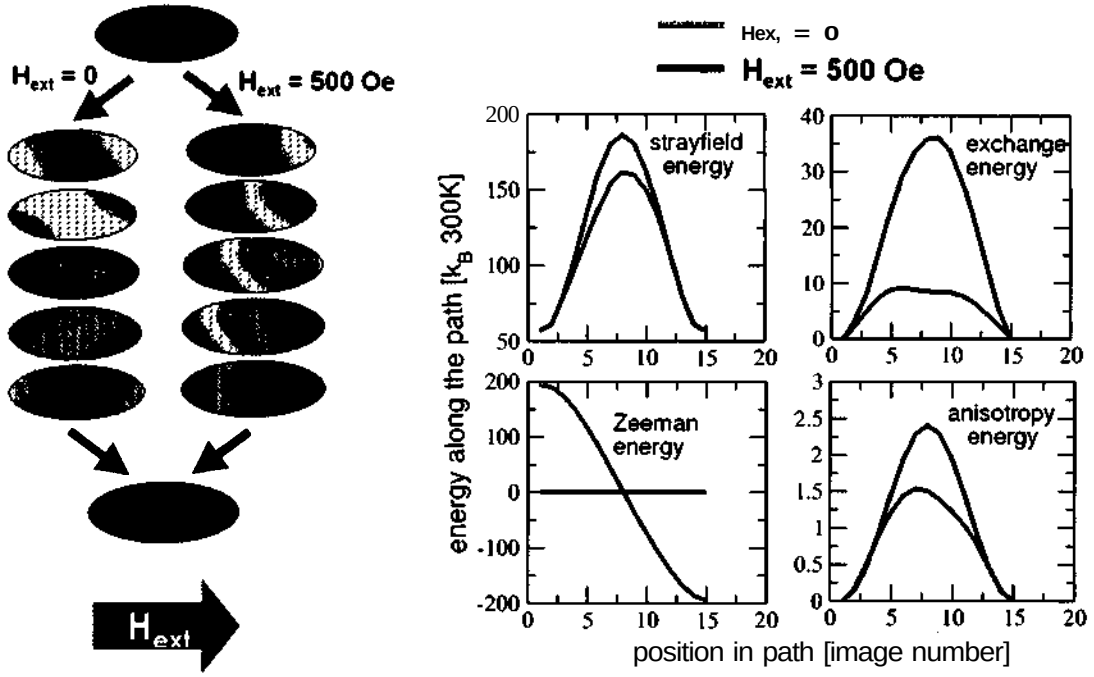

Figure 9.7 Left: Magnetization configurations along the minimum energy paths for the thermal reversal of a 4 nm thin NiFeCo MRAM element of 62.5 nm size. An opposing field is applied along the easy axis (=long axis). For fields stronger than 150 Oe there is an abrupt change of the reversal mode to the one shown here (500 Oe). Right: Energies along the minimum energy path. The blue lines show energies when no field is applied. The red lines are obtained at an easy axis field of 500 Oe. The exchange energy shows that at higher fields the reversal mode is more inhomogeneous than when no field is applied.

The change of the reversal mode is also observed in the increase of the arclength of the path above 150 Oe. The mode has become more inhomogeneous as shown in Fig. 9.7. As a consequence the total length of the path increased. Also note how the energy barrier decreases with increasing field strength.

The field dependence of the reversal mode is explained as follows: at low external fields the reversal mode is mainly determined by the competition of exchange and strayfield energy. At higher fields the Zeeman energy gets a stronger weight and it can get of advantage to follow a more inhomogeneous mode. More energy is "spent" in exchange, but therefore more energy is gained in the Zeeman part. In total the energy barrier is smaller even though the

mode has become more complex. This observation is shown in the plots in Fig. 9.7 on the right. The four energy contributions along the minimum energy paths are compared for 62.5 nm particle size. We compare the minimum energy path obtained with zero external field with the minimum energy path obtained for H_{ext} = 500 Oe. The exchange energy is 4 times higher at 500 Oe than at zero field since the reversal mode involves the motion of a domain wall. The anisotropy energy only plays a minor role which means that the shape of the particle and the external field dominates the behavior of the reversal mode and height of the energy barrier.

For hard-axis fields the opposite behavior is observed. The reversal mode becomes more homogeneous at stronger fields.

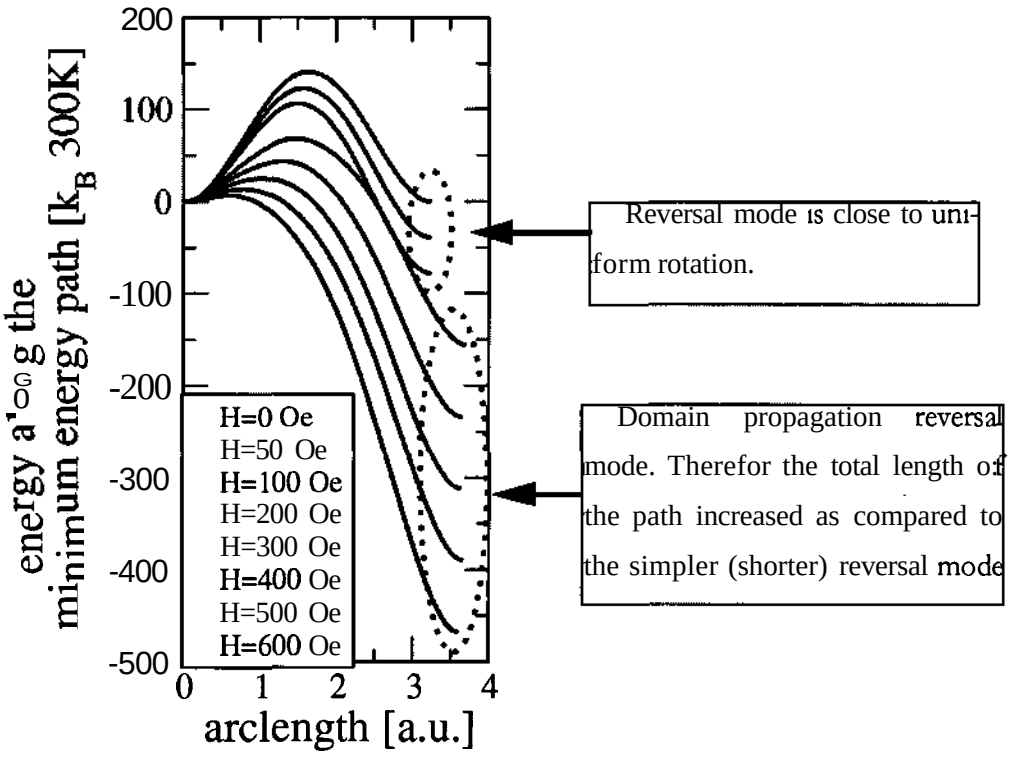

Figure 9.8 Energy along the minimum energy paths for a 62.5 nm element as a function of the arclength in the path. The energy is normalized to the energy of the initial (non-reversed) state. Different easy axis fields are applied. The increase of the length of the path above 200 Oe is due to a change of the reversal mode. The mode has become more inhomogeneous which is seen in figure 9.7.

10 COMPARISON OF LANGEVIN DYNAMICS WITH ENERGY BARRIER COMPUTATION

Thermal transition rates between ground states in small softmagnetic elements up to a size of 90x90x4.5 nm³. Two complementary methods to study thermal effects in micromagnetics are compared. On short time scales Langevin dynamics gives insight in the thermally activated dynamics. For longer time scales the nudged elastic band method is applied. The method calculates a highly probable thermal switching path between two local energy minima of a micromagnetic system. For small elements both methods can be applied. Good agreement is found between the results obtained with the different methods.

10.1 Transition rates in squared soft magnetic elements

We study squared softmagnetic permalloy platelets. The stable states in a $50 \cdot 50 \cdot 5$ nm^3 square are so called "leaf" states [28,29]. The average magnetization is aligned in-plane, and along one of the 4 diagonals (see Fig. 10.1). A finite element mesh with an average mesh size of 5 nm was used. The thermal fluctuations drive the magnetization to precess around the leaf states maintaining the magnetization in-plane. From time to time switching from one leaf state to another occurs (Fig. 10.1).

Using Langevin dynamics we first calculate the average relaxation time T for the thermally induced switching between the leaf states. The relaxation time, $T = \tau_0 \exp(\Delta E / k_B T)$ [16,78], is the inverse of probability per unit time for crossing the barrier AE. The attempt frequency, $f_0 = 1/\tau_0$, depends on material parameters, like anisotropy, particle shape, and damping.

In a first step we vary the temperature from 50-200 K. The total simulation time is chosen to sample at least 10 switching events which then give the average relaxation time T. By fitting these curves (see Figure 10.2) with the Néel-Brown theory [16,78] we obtain the energy barrier and the prefactor (attempt frequency). An energy barrier of (5.7 k_B 100 K) and an attempt frequency of $f_0 = 6 \cdot 10^9$ Hz was found for a = 0.02.

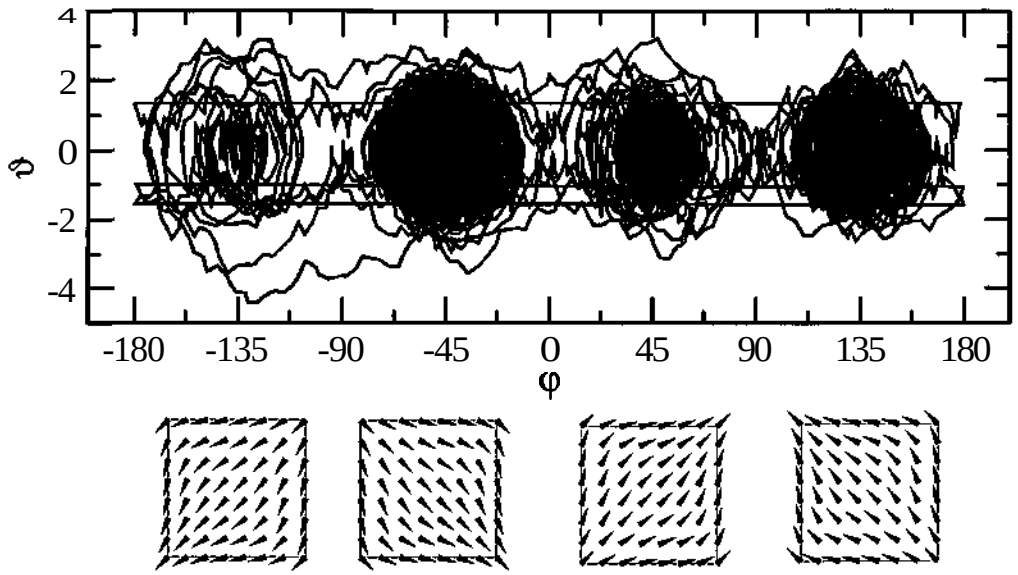

Figure 10.1 Thermal switching between the 4 "leaf" states *of* a *50* x *50 x 5* nm^3 platelet (T = 120 K). The average magnetization direction is shown in polar coordinates. Thermal fluctuations cause the magnetization to precess around the leaf states maintaining the magnetization almost in-plane (maximum theta is only 4°). From time to time a switching from one leaf state to another occurs. The squares schematically show the magnetization direction that correspond to a particukr region of (p.

In a second step we vary the damping constant, α, at constant temperature of 200 K. Figure 10.3 shows that for values of the damping constant $0.001 < \alpha < 0.1$ the attempt frequency reaches its maximum values of about $f_0 = 5 \cdot 10^9$ Hz. Outside this region the attempt frequency drastically decreases. This is understood since in the limit of zero or infinite damping the transition frequency has to vanish.

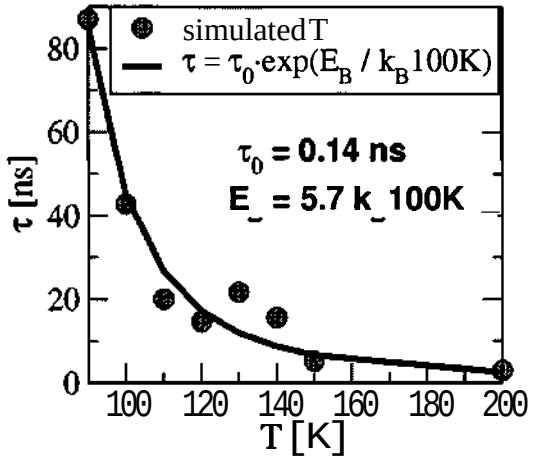

Figure 10.2 Thermally induced switching between the leaf states in a square NiFe nanoelement (50*50*5 nm^3). The relaxation time T is plotted as a function of the temperature. Fitting the values with the Néel-Brown theory gives the energy barrier and prefactor $f_0=1/\tau_0$.

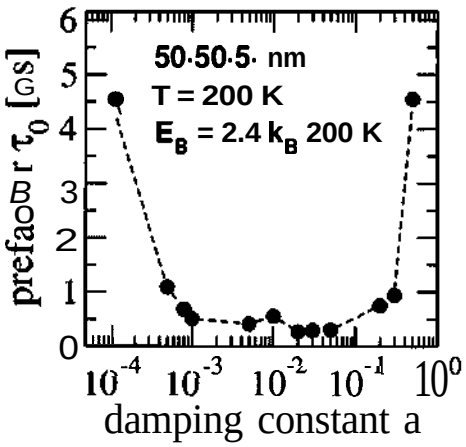

Figure 10.3 Thermally induced switching between the leaf states in a square NiFe nanoelement (50·50·5 nm^3). Dependence of the prefactor τ_0 in the Néel Brown law on the damping constant a. The temperature was fixed at 200 K.

The direct computation of the energy barrier using the nudged elastic band method gives a barrier height of 4.8 k_B 100 K which is in good agreement with the results obtained from Langevin dynamics. The deviation of the energy barrier obtained with Langevin dynamics can be attributed to the following effects: (1) work in the limit of low energy barriers, AE ~ k_BT. So it is not clear how to count recrossing events. Furthermore changes of the free energy with temperature are not taken into account with the standard NEB method. (2) The prefactor is temperature dependent [23]. (3) A limited number of calculated switching events causes poor statistics.

When comparing the transition states with those in the smaller 50·50·5 nm^3 square, we see that in the large elements the transition states are more complex than just a simple flower-state. For the small sample, 50·50·5 nm^3, the transition state (saddle point) is the flower state [29] with the net in-plane magnetization along the edges. In a larger sample, 90·90·4.5 nm^3, the situation is different. From the minimum energy path we see that also a metastable C-state is present. However the energy barrier (ΔE_1 = 0.9 k_B 450K) to escape from the C-state is much smaller than the energy barrier to access the C-state from a leaf state (ΔE_2 = 6.5 k_B450K). As a consequence, the relaxation time to escape from the C-state into a leaf-state is more than 3 orders of magnitude smaller than the relaxation time to access the C-state from the leaf state. With a prefactor in the Néel-Brown equation τ_0 = 0.1 ns, the average waiting time $T = \tau_0 \exp(\Delta E_2 / k_B 450K)$ becomes ~7.6 ns. Thus, we can expect to observe a thermal switching event with Langevin dynamics at a temperature of 450 K. Fig. 10.4 compares such a thermal switching event with the minimum energy path. For the minimum energy path magnetization states and the energy along the path are displayed. For Langevin dynamics the magnetization states and the time evolution of the net in-plane magnetization direction are displayed. With Langevin dynamics we observe a thermal switching between two leaf-states. The angle of the in-plane magnetization switches from 45° to –45°. Indeed the same saddle points and the metastable C-state (0°) are visited as predicted with the NEB-method. We see that the C-state is visited only for a very short time since the relaxation time $T = \tau_0 \exp(\Delta E_1 / k_B T) = 0.025\ ns$ is very small.

10.2 Summary

The comparison of the transition states obtained with the two different methods shows very good agreement: The thermal switching process obtained with Langevin dynamics agrees well with the minimum energy path obtained with the NEB-method. The advantage of the NEB-method is the possibility to calculate transitions over large energy barriers, while Langevin dynamics is limited to short transition times and therefore small energy barriers only.

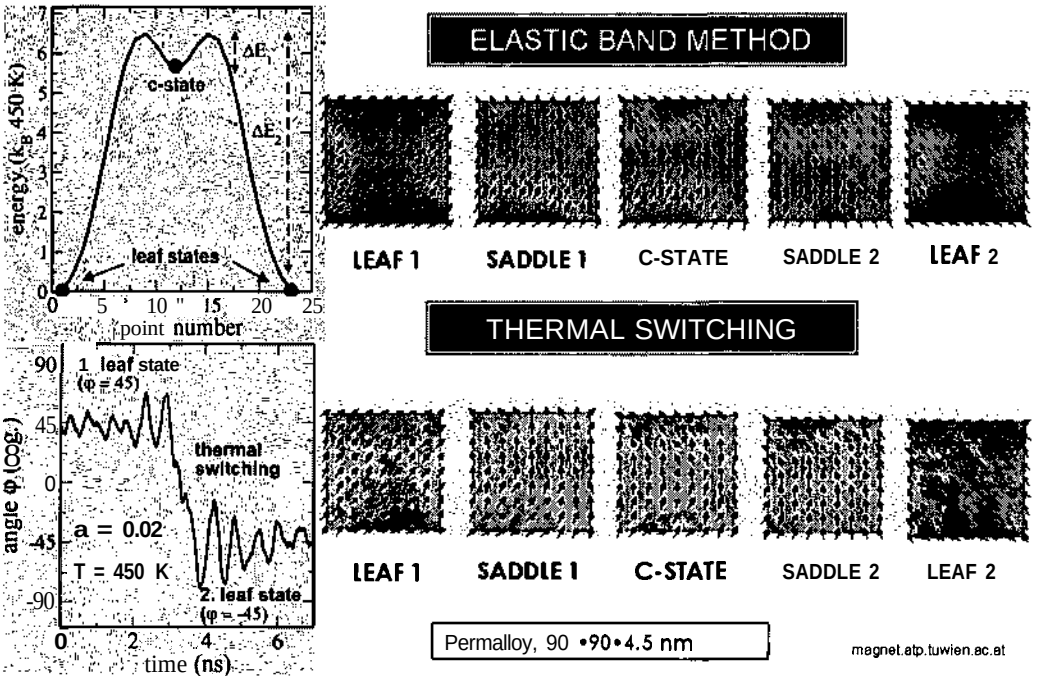

Figure 10.4 Comparison of the results obtained with the nudged elastic band method (top sequence) and with direct Langevin simulation (bottom sequence). Shown are magnetization states along the minimum energy path and the energy along this path. The magnetization states obtained with Langevin dynamics are in good agreement with the results obtained with the nudged elastic band method.

11 OUTLOOK

Since magnetic devices become smaller and smaller, especially in magnetic recording devices, thermal effects become crucial. Therefore the numerical simulation of thermal effects becomes important, especially the long time thermal stability of the magnetization in magnetic storage devices. The nudged elastic band method is a very powerful method for calculating energy barriers in magnetic systems even if the dimension of unknowns in a micromagnetic model is as high as 50000. The comparison with Langevin dynamics of thermally activated barrier crossing show that indeed the same transition state is chosen as predicted with the direct energy barrier calculation.

In order to derive transition rates theoretically, the attempt frequency is required in addition to the energy barrier. The efficient calculation of the prefactor in the Néel-Brown theory is still an open question. Several numerical methods and theories exist for the calculation of transition rates in chemical physics [59,62]. It is not obvious whether these methods will work efficiently for micromagnetic systems with a high number of degrees of freedom.

The knowledge of the minimum energy path and of the transition states is required to calculate thermal switching rates using transition state theory. The calculation of the minimum energy path using the nudged elastic band method is a first step towards the calculation of transition rates in complex micromagnetic systems.

12 APPENDIX

12.1 Demo source code for a 2D example

A C++ source code that demonstrates the path finding method is available at http://magnet.atp.tuwien.ac.at/dittrich.

12.1.1 Analyzing the "path.log" file

Compile the source code and run the "app" with the parameters as set. The results of the program are written to the "path.log" file. It looks like this:

```
#  iterNr, 3   arcLenght, 4      Energy, 5      thetal, 6      theta2, 7 springforce, 8    absforce, 9
P   1       1   0.000000e+00   0.000000e+00   0.000000e+00   0.000000e+00   0.000000e+00   0.000000e+00
P   2       1   3.189261e-01  -6.799977e-01   2.243995e-01  -2.266247e-01   0.000000e+00   0.000000e+00
P   3       1   6.377730e-01  -3.440985e-01   4.487990e-01  -4.531378e-01   0.000000e+00   0.000000e+00
P   4       1   9.564653e-01   1.402902e-01   6.731984e-01  -6.794333e-01   0.000000e+00   0.000000e+00
p   5       1   1.274936e+00   6.761750e-01   8.975979e-01  -9.054162e-01   0.000000e+00   0.000000e+00
P   6       1   1.593128e+00   1.156609e+00   1.121997e+00  -1.131007e+00   0.000000e+00   0.000000e+00
P   7       1   1.911000e+00   1.486173e+00   1.346397e+00  -1.356146e+00   0.000000e+00   0.000000e+00
P   8       1   2.228526e+00   1.599920e+00   1.570796e+00  -1.580796e+00   0.000000e+00   0.000000e+00
P   9       1   2.545698e+00   1.476021e+00   1.795196e+00  -1.804945e+00   0.000000e+00   0.000000e+00
P  10       1   2.862524e+00   1.139704e+00   2.019595e+00  -2.028605e+00   0.000000e+00   0.000000e+00
P  11       1   3.179032e+00   6.578820e-01   2.243995e+00  -2.251813e+00   0.000000e+00   0.000000e+00
P  12       1   3.495263e+00   1.257018e-01   2.468394e+00  -2.474629e+00   0.000000e+00   0.000000e+00
P  13       1   3.811274e+00  -3.522399e-01   2.692794e+00  -2.697133e+00   0.000000e+00   0.000000e+00
P  14       1   4.127131e+00  -6.823149e-01   2.917193e+00  -2.9194186+00   0.000000e+00   0.000000e+00
P  15       1   4.442911e+00  -8.000000e-01   3.141593e+00  -3.141593e+00   0.000000e+00   0.000000e+00
P   1       2   0.000000e+00   0.000000e+00   0.000000e+00   0.000000e+00   0.000000e+00   0.000000e+00
P   2       2   3.189261e-01  -6.799977e-01   2.245117e-01  -2.264969e-01  -7.927853e-05   1.133796e-03
P   3       2   6.377730e-01  -3.440985e-01   4.489835e-01  -4.529222e-01  -1.545261e-04   1.891740e-03
P   4       2   9.564653e-01   1.402902e-01   6.733212e-01  -6.792645e-01  -2.219246e-04   1.391826e-03
P   5       2   1.274936e+00   6.761750e-01   8.975384e-01  -9.054166e-01  -2.780692e-04   3.966666e-04
P   6       2   1.593128e+00   1.156609e+00   1.121692e+00  -1.131244e+00  -3.201441e-04   2.575746e-03
P   7       2   1.911000e+00   1.486173e+00   1.345871e+00  -1.356598e+00  -3.460637e-04   4.623021e-03
P   8       2   2.228526e+00   1.599920e+00   1.570159e+00  -1.581359e+00  -3.545728e-04   5.666752e-03
P   9       2   2.545698e+00   1.476021e+00   1.794681e+00  -1.805387e+00  -3.453009e-04   4.523721e-03
P  10       2   2.862524e+00   1.139704e+00   2.019306e+00  -2.028828e+00  -3.187696e-04   2.435844e-03
P  11       2   3.179032e+00   6.578820e-01   2.243949e+00  -2.251800e+00  -2.763552e-04   3.160370e-04
P  12       2   3.495263e+00   1.257018e-01   2.468525e+00  -2.474451e+00  -2.202106e-04   1.473189e-03
P  13       2   3.811274e+00  -3.522399e-01   2.692980e+00  -2.696912e+00  -1.531515e-04   1.924579e-03
P  14       2   4.127131e+00  -6.823149e-01   2.917318e+00  -2.919276e+00  -7.851570e-05   1.260859e-03
P  15       2   4.442911e+00  -8.000000e-01   3.141593e+00  -3.141593e+00   0.000000e+00   0.000000e+00
```

DESCRIPTION

column 2 image number

column 3 the current time step (iteration number)

column 4 arclength (length of the path from the initial image to the current image)

column 5 energy of the image

column 6,7 the 2 coordinates for this simple energy landscape

column 8 the springforce acting on the image

column 9 the total force acting on the image = L^norm[normalgradient + springforce].

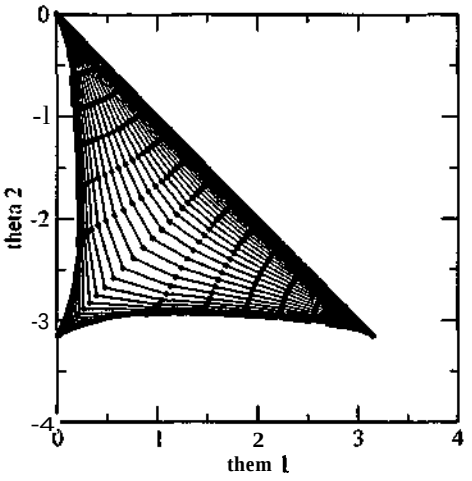

In 2D we can still visualize the path. To do this we plot column 6 and 7. The red curve is the initial guess for the path. The solid black curve is the path at the end (= minimum energy path).

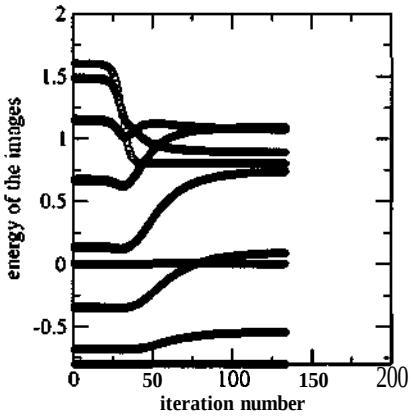

To see the evolution of the energy of the images during the optimization plot column 3 and 5.

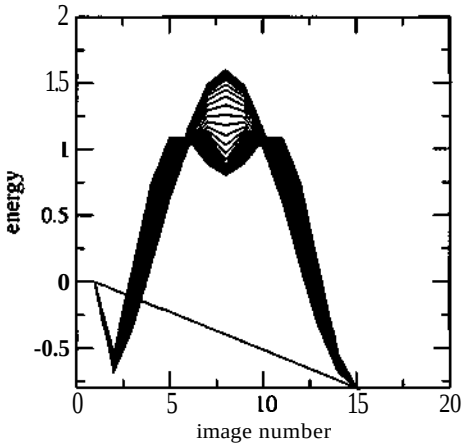

When plotting column 2 and 5 we see the energy along the path during the optimization

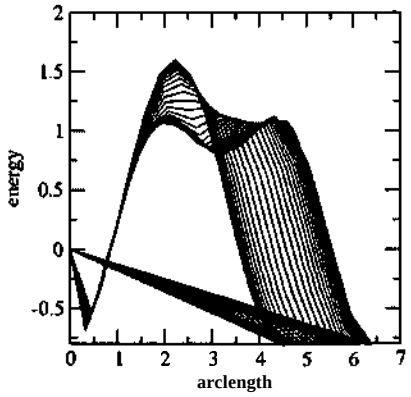

Or you plot column 4 and 5. Here we also see that the length of the path changes while the optimization proceeds.

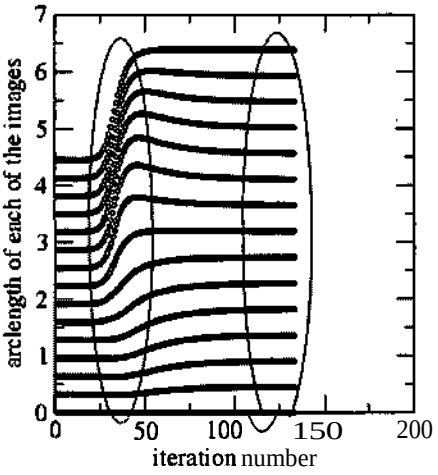

Length changes are also seen by plotting columns 3 and 4. In this case the length increases. In the initial guess the images were equally spaced. But in an intermediate path of the simulation this is not more the case. Since there is a springforce the images become equally spaced again at the end. A stronger springforce would have kept the equal distance all the time.

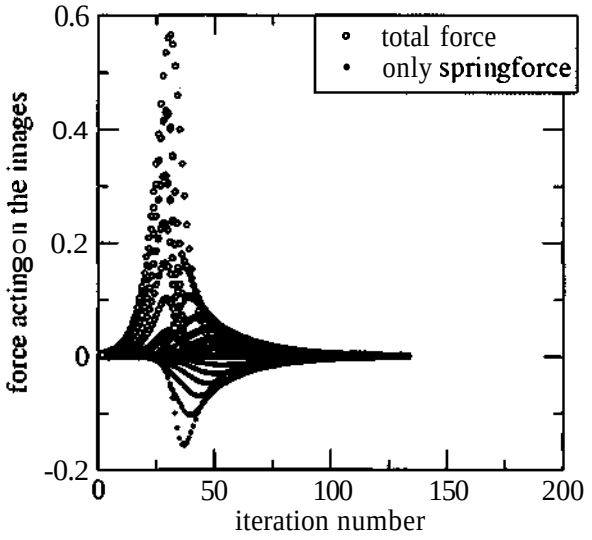

To see the forces acting on the images you can plot column 3 and 8 or 3 and 9. We see that in the beginning there is no springforce since the images were equally spaced in the initial path. Here the evolution of the path is dominated by the energy landscape (following the normal component of the gradient). But after a while the images get non-equally spaced and the spring forces increase. At the end the total force is dominated by the spring force. Here the path has reached the minimum energy path, but the images still move along the path according to the springforce until they are equally spaced again.

12.1.2 Changing the parameters

You can change the parameters in the "path.inp" file:

```
PATH_SIMULATION
15                      number_of_pathpoints
4                       dimension_of_space
1.0                     spring_constant
0.15                    euler_timestep
```

You can play with 3 parameters here:

The dimension of space cannot be changed without further implementation in the code (see below).

12.1.2.1 number of path points

Number of images used to describe the path.

12.1.2.2 dimension of space

Is set to 4 here. Why not 2? The code is implemented for the 4D case described in section 4.9.1. Four angles are needed to describe the unit vectors (only the direction of the spins can change) of two interacting spins. However the energy landscape reduces to 2D (here the 2 theta angles) due to symmetry arguments. The two phi angles will not change in this case. For the portability of the code we keep all 4 angels so that it can be extended to cases with many interacting spins.

The source code can easily be extended to higher dimensions. Set the dimension according to the number of spins that you have. For 1000 spins the dimension is 2000 and so on. The data format and most routines are implemented to work for higher dimensions except some of them: You need to calculate the energy and the energy gradient of your spin-system and change the two subroutines (which are limited to this 2D case).

"void Path::Energy(Mag* M)"

"void Path::calcgradient(Mag* M)"

in the "Path.cpp" file accordingly to the higher dimensional case. The rest (tangent, forces, springforces, integration) should work properly.

```
void Path::Energy(Mag* M)
{
/*** special case of energy for to spins -> dimension=4 !! *«•••/

//m. . .magnetization in theta and phi

double* m=M->mag;
double k=0.2, h=0, b=0;//3.141527;
//k. . .dipolarexchange
//h. . .external field
//b. . .bondangle


M->energy= sin(m[0])*sin(m[0])+sin(m[2])*sin(m[2])
           +2*k*(sin(m[0])*sin(m[2])*cos(m[1]-m[3])+cos(m[0])*cos(m[2])-3*cos(m[0]-b)*cos(m[2]-b))
           +2*h*(cos(m[0])+cos(m[2]));

)
void Path: :calcgradient(Mag* M)
1
/***• special case of gradient for to spins -> dimension=4 J! *••**/

//m. . .magnetization in theta and phi
//gradient. . .in theta and phi

double* m=M->mag;
double k=0.2, h=0, b=0;//3.141527;
//k. . .dipolarexchange
//h. . .external field
//b. . .bondangle

gradient[0] - 2.0*sin(m[0])*cos(m[0])+2.0*k*(cos(m[0])*sin(m[2])*cos(m[1]-m[3])-sin(m[0])*cos(m[2])+3.0*sin(m[0]-b)*cos(m[2]-b))-2.0
*h*sin(m[0]);

gradient[1]=2.0*k*(-sin(m[0])*sin(m[2])*sin(m[1]-m[3]));

gradient[2] = 2.0*sin(m[2])*cos(m[2])+2.0*k*(sin(m[0])*cos(m[2])*cos(m[1]-m[3])-cos(m[0])*sin(m[2])+3.0*cos(m[0]-b)*sin(m[2]-b))-2.0
*h*sin(m[2]);

gradient[3]=2.0*k*(sin(m[0])*sin(m[2])*sin(m[1]-m[3]));

for(int i=0;i<=3;i++) gradient[i]=-gradient[i];

}
```

And of course you need to implement the input of the initial path and output of the final path and add things you want into the log file. You should also change the time integration method to increase efficiency (see below).

12.1.2.3 spring constant

Try to make it weaker and stronger. You may have to choose smaller time steps at stronger springforce.

12.1.2.4 Euler timestep

Should be no surprise that if the timestep is too large one runs into numerical problems. If you extend the code to higher dimensions you should use something more efficient than Euler. Euler is used here just for demonstration and in order to keep the demo-code simple and short. We found that the BDF method in the ODE-solver package CVODE (free C-code) is about 100 times faster than the explicit Adams method (also available within the CVODE package) when simulating magnetic systems discretized with finite elements. Note that the Adams method is also faster than Euler since it makes use of past values.

12.1.2.5 Changing the initial path

You can change the initial path in the source code. However it only works now for the special case of two spins (4D). The routine "void Path::init()" creates the initial path. Change this if you want something else than the straight line initial path or if you want different initial and final states.

REFERENCES

[1] A. Aharoni, *Demagnetizing factors forectangular ferromagnetic prisms.*, J. Appl. Phys. 83, 3432, (1998)

[2] A. Aharoni, *Usefuiupperand lower bounds to the magnetostatic self-energy*, IEEE Trans. Magn., 27, 4793 (1991)

[3] A. Aharoni, *Introduction to the Theory of Ferromagnetism*, Clarendon Press Oxford, 1996.

[4] Amikam Aharoni, *Coherent and incoherent magnetization processes in non-interacting particles*, NATO AS1 E338, 1 (1997), "Magnetic hysteresis in novel magnetic materials", G. C. Hadjpanayis Ed.

[5] T. Aign, P. Meyer, S. Lemerle, J. P. Jamet, J. Ferré, V Mathet, C. Chappert, J. Gierak, C. Vieu, F. Rousseaux, H. Launois, and H. Bernas, *Magnetization Reversal in Arrays ofPerpendicularly Magnetized Ultrathin Dots Coupled by Dipolar Interaction,* Phys. Rev. Letters 81 (1998) 5656

[6] Simone Anders, IBM, private communication, 2001

[7] G. Albuquerque, J. Miltat and A Thiaville, *Self-consistency based control scheme for magnetization dynamics*, J. Appl. Phys., vol. 89, 6719, 2001.

[8] Goncalo Albuquerque, *Magnetisation Precession in Confined Geometry: Physical and Numerical Aspects,* Ph.D. Thesis (Université Paris XI Orsay, 2002)

[9]M. N. Baibich, J. M. Broto, A. Fert, F. Nguyen Van Dau, and F. Petroff , *Giant Magnetoresistance of (001)Fe/(001)Cr Magnetic Superlattices.*, Phys. Rev. Lett., vol. 61, pp. 2472, 1988.

[10] Josh Barnes & Piet Hut, *A hierarchical O(Nkg N) forcecalculation algorithm,* 1986. Nature 324, 446.

[11] D.V. Berkov, *Numerical calculation ofthe energy barrier distribution in disordered many-particle systems: thepath integral method*, J. Magn. Magn. Mater. 186 (1998) 199.

[12] D. V. Berkov, *Calculation ofenergy barriers in strongly interacting many-partick systems,* J. Appl. Phys. 83 (1998) 7390

[13] H. N. Bertram, V. L. Safonov, Z. Jin, *IEEE Trans. Magn.* 38, 2514 (2002).

[14] P. G. Bolhuis, D. Chandler, C. Dellago, P. L. Geissler, *Transitionpath sampling: Throwingropes over rough mountainpasses, in the dark*, Annu. Rev. Chem.,53 (2002) 291-318

[15] H.-B. Braun, *J. Appl. Phys.* 76, 6310 (1994).

[16] W F. Brown, Jr., *Thermal fluctuationsof a single domain particle,* Phys. Rev. 130 (1963) 1677.

[17] W F. Brown, *Theory ofthe approach to magnetic saturation,* Phys. Rev, vol. 58, pp. 736, (1940).

[18] W. F. Brown Jr., *Micromagnetism*, New York: Interscience, 1963.

[19] A. M. Bruaset, *Krylov subspace iterations for sparse linear systems in Numerical Methods and Software Tools in Industrial Mathematics,* Eds. Morten Daehlen and Aslak Tveito, Birkhauser,

Boston, 21, 1997.

[20] R. L. Burden J. D. Faires, *Numerical Analysis*, sixth edition, Brooks/Cole Publ. Co., Pasific Grove, 1997.

[21] S. H. Charap, P. L. Lu and Y. He, *Thermal stability of recorded information at high densities*, IEEE Trans. Magn., vol.33, pp. 978, 1997.

[22] W. Chen, S. Zhang, H. N. Bertram, J. Appl. Phys. 71 (1992) 5579.

[23] W T. Coffey, D. S. F. Crothers, J. L. Dormann, Yu. P. Kalmykov, E. C. Kennedy, W Wernsdorfer, Phys. Rev. Lett. 80 (1998) 5655.

[24] S. D. Cohen and A. C. Hindmarsh, *CVODE User Guide*, Lawrence Livermore National Laboratory report UCRL-MA-118618, Sept. 1994.

[25] S. D. Cohen and A. C. Hindmarsh, *CVODE, A Stiff/Nonstiff ODE Solver in C*, Computers in Physics, vol. 10, pp. 138, 1996.

[26] R. Comerford, *Magnetic storage: The medium that wouldn't die*, IEEE Spectrum, pp. 36, December 2000,

[27] R. P. Cowburn, M. E. Weiland, *Room temperature magnetic quantum cellular automata*, Science, vol. 287, pp. 1466, 2000.

[28] R.P. Cowburn, *Property variation with shape in magnetic nanoelements*, J. Phys. D: Appl. Phys. 33 (2000) R1-R16

[29] R. P. Cowburn, M. E. Weiland, *Phase transitions in planar magnetic nanostructures*, Appl. Phys. Letters, 72 (1998) 2041

[30] James Daughton, *Magnetoresistive Random Access Memory (MRAM)*, review 2000, www.nve.com/otherbiz/mram.pdf

[31] C. Dellago, P. G. Bolhuis, F. S. Csajka, D. Chandler, J. Chem. Phys. 108 (1998) 1964.

[32] C. Dellago, P. G. Bolhuis, P. L. Geissler, *Transition path sampling*, Contribution for the "Advances in Chemical Physics" Oct. 2001

[33] R. Dittrich, T. Schrefl, D. Suess, W Scholz, H. Forster and J. Fidler, *A path method for finding energy barriers and minimum energy paths in complex micromagnetic systems*, J. Magn. Magn. Mater. 250, (2002) L12

[34] R. Dittrich, T. Schrefl, V. Tsiantos, H. Forster, D. Suess, W. Scholz, J. Fidler, *Micromagnetic simulation of thermal effects in magnetic nanostructures*, MRS Symposium Proceedings, 746 (2002) 183

[35] P. D. Drummond and I. K. Mortimer, *J. Comput. Phys.* **93**, 144 (1991).

[36] W E and X.-P. Wang, SIAM Journal on Numerical Analysis, vol. 38, pp. 1647, 2000.

[37] W. E, W. Ren and E. Vanden-Eijnden, *String method for the study of rare events*, Phys. Rev. B 66, 52301 (2002)

[38] W E, W Ren, E. Vanden-Eijnden, *Energy landscape and thermally activated switching of submicron-sized ferromagnetic elements*, J. Appl. Phys., 93 (15.2.2003), in press

[39] W. E, W Ren, E. Vanden-Eijnden, *Energy Landscape and Rare Events,* ICM 2002

[40] E. Feldtkeller, Z. angew. Phys. 19, 530 (1965).

[41]H. Forster, *Reversal modes in mesoscopic structures,* PhD thesis, 2003, Vienna University of Technology

[42]H. Forster, N. Bertram, X. Wang, R. Dittrich, T. Schrefl, *Energy barrier and effective thermal reversal volume in columnar grains,* J. Magn. Magn. Mater. 2003, in press

[43]D.R. Fredkin and T. R. Koehler, *Numerical micromagnetics of small particles,* IEEE Trans. Magn., vol. 24, pp. 2362, 1988.

[44] D.R. Fredkin, T.R. Koehler, *IEEE Trans. Magn.* 26, 415 (1990).

[45] H. Fukushima, Y. Uesaka, Y. Nakatani and N. Hayashi, *J. Magn. Magn. Mater.* 242-245, 1002 (2002).

[46] J. Gadbois and J. G. Zhu, *Effect of edge roughness in nano-scale magnetic bar switching,* IEEE Trans. Magn., vol. 31, pp. 3802, 1995.

[47] Jose-Miguel Garcia, MFM images were performed in the group of Jacques Miltat, CNRS Université Paris-sud, LPS Paris Sud, Laboratoire de physique des solides, 91405 Orsay, France

[48] J. L. Garcia-Palacios and F. J. Lazaro, *Langevin-dynamics study of the dynamical properties of small magnetic particles,* Phys. Rev. B 58, 14937 (1998).

[49] C. W Gardiner, *Handbook of Stochastic Methods,* Berlin, Springer, 1985.

[50] P. L. Geissler, 2-D demo programm, http://www.science.uva.nl/~bolhuis/tps/

[51] T. L. Gilbert, *A Lagrangian formulation of gyromagnetic equation of the magnetization field,* Phys. Rev., Vol 100, p. 1243, 1955

[52]L Guan, J. G. Zhu, J. Appl. Phys. 91 (2002) 7688.

[53] M.A.M. Haast, *Patterned magnetic thin films for ultra high density recording,* Thesis University of Twente, Enschede, The Netherlands, 1999

[54] Chiseki Haginoya, Seiji Heike, Masayoshi Ishibashi, Kimio Nakamura, Kazuyuki Koike, Toshiyuki Yoshimura, Jiro Yamamoto, Yoshiyuki Hirayama, *Magnetic nanoparticle array with perpendicular crystal magnetic anisotropy,* J. Appl. Phys. 85 (1999) 8327

[55] C.H. Hee, J.P. Wang and T.C. Chong, *Micromagnetic simulation for antiferromagnetically coupled recording media,* IEEE Trans. Mag., 37 (2001) 1515

[56] G. Henkelman and H. Jonsson, *Improved tangent estimate in the NEB method for finding minimum energy paths,* J. Chem. Phys. 113 9978 (2000).

[57]G. Henkelman, B. P. Uberuaga and H. Jónsson, *A cUmbingimage nudged elastic band method for finding saddle points and minimum energy paths,* J. Chem. Phys. 113, 9901 (2000).

[58] G. Henkelman, G. Jóhannesson, and H. Jonsson, *Methods for finding saddle points and minimum energy paths,* Progress on Theoretical Chemistry and Physics, ed. S. D. Schwartz (Kluwer Academic Publishers, 2000).

[59] G. Henkelman and H. Jonsson, *Theoretical calculations of associative adsorption of methane o an Ir(111) surface,* Physical Review Letters 86: 664 (2001).

[60] A. C. Hindmarsh and L. R. Petzold, *Algorithms and Softwar for Ordinary Differentia Equations and Differential-Algebraic Equations,* Computers in Physics vol. 9, pp. 148, 1995.

[61] S. Hoefinger, J. Fidler, T. Schrefl, *TEM Characterization ofhigh density hard disk media,* 6th Multinational Congress on Microscopy, Pula (CRO), June 2003

[62] G. A. Huber, S. Kim, *Weighted-Ensemble Brownian Dynamics Simulation for Protein Association Reactions,* Biophysical Journal, 70 (1996) 97-110

[63] A. Hubert, J. Magn. Magn. Mater. 2, 25 (1976).

[64] N. Inaba, Uesaka Y, Nakamura A., Futamoto M., Sugita Y, Narishige S., *Damping constants of Co-Cr-Ta and Co-Cr-Pt thin films,* IEEE Trans. Mag. 33 (1997) 2989

[65] S. Ingvarsson, Gang Xiao, S.S.P. Parkin, W.J. Gallagher, *Thickness-dependent magnetic properties of Ni81Fe19, Co90Fe10 and Ni65Fe15Co20 thin films,].* Magn. Magn. Mater. 251, 202 (2002)

[66] A. Inomata, B. R. Acharya, E. N. Abarra, A. Ajan, D. Hasegawa, I. Okamoto, J. Appl. Phys. 91 7671 (2002).

[67] D. Jackson, *Classical electrodynamics,* 2nd edition, John Wiley & Sons, New York 1975

[68] Jason Janesky, private communication, Intermag 2003

[69] G. H. Jóhannesson and H. Jonsson, *Optimization of Hyperplana Transition States,* submitted to Journal of Chemical Physics 2001.

[70] M. Jones and J. J. Miles, *An accurate and efficient 3-D micromagnetic simulation of metal evaporated tape,* J. Magn. Magn. Mater., vol. 171, pp. 190, 1997.

[71] M. Kléman, Points, Lines and Walls (J. Wiley, Chichester, 1983).

[72] R. H. Koch, G. Grinstein, G. A. Keefe, Yu Lu, P. L. Trouilloud, and W J. Gallagher, *Thermally Assisted Magnetization Reversal in Submicron-Sized Magnetic Thin Films,* Phys. Rev. Lett. 84 (2000) 5419

[73] J. Lohau, A. Moser, C. T. Rettner, M. E. Best, and B. D. Terns, *Writing and reading perpendicular magnetic recording media patterned by a focused ion beam,* Appl. Phys. Lett. 78 (2001) 990

[74] Jens Lohau, Andreas Moser, Charles T. Rettner, Margaret E. Best, and Bruce D. Terns, *Effect of ion beam patterning on the mite and read performance of perpendicular granular recording media,* IEEE Transactions on Magnetics, 37, No. 4, 1652–1656 (2001).

[75] P. Maragakis, Stefan A. Andreev, Yisroel Brumer, David R. Reichman, Efthimios Kaxias *Adaptive nudged elastic band approach for transition state calculation,* J. Chem.Phys. 117 (2002) 4651

[76] W H. Meiklejohn, C. P. Bean, *New magnetic anisotropy,* Phys. Rev. , vol. 102, pp. 1413, 1956.

[77] Jacques Miltat, Gonçalo Albuquerque, Andre Thiaville, *An Introduction to Micromagnetics in the Dynamic Regime,* Spin Dynamics in Confined Magnetic Structures 1, Topics Applied Physics 83 (Springer-Verlag, 2002)

[78] L. Néel, *Ann. Geophys.* 5, 99 (1949).

[79] T. Okuno, K. Shigeto, T. Ono, K. Mibu, and T. Shinjo, J. Magn. Magn. Mater. **240**, 1 (2002).

[80] Alexander Polansky, *Mathematische Methoden der Computergrafik,* Interaktives Elektronisches Skriptum, Diplomarbeit TU-Wien, http://www.apm.tuwien.ac.at/docs/lva/mmgdv/

[81] G. A. Prinz, *Magnetoelectronics applications,* J. Magn. Magn. Mater., vol. 200, pp. 57, 1999.

[82] J. Reinhardt, Int. J. Magn. 5, 263 (1973).

[83] W Ren, *Numerical Methods for the Study of Energy Landscapes and Rare Events,* Ph.D thesis, New York University

[84] CT. Rettner, M. E. Best and B.D. Terris, *Patterning of Granular Magnetic Media with a Focused Ion Beam to Produce Single-Domain Islands at > 140 Gbit/in^2,* IEEE Trans. Magn. 37 (2001) 1649-1651

[85] C. T. Rettner, S. Anders, J. E. E. Baglin, T. Thomson, and B. D. Terns, *Characterization of the magnetic modification of Co/Pt multilayer films by He+, Ar+, and Ga+ ion irradiation,* IBM Almaden Research Center, Applied Physics Letters, 80 (2002) 279-281

[86] HJ. Richter, IEEE Trans. Magn. 35, 2790 (1999).

[87] H. J. Richter, Er. Girt, IEEE Trans. Mag. 37 (4) July 2001

[88] N. D. Rizzo, M. DeHerrera, J. Janesky, B. Engel, J. Slaughter and S. Tehrani, *Thermally activated magnetization reversal in submicron magnetic tunnel junctions for magnetoresistive random access memory,* Appl. Phys. Lett. 80, (2002) 2335

[89] M. E. Schabes, H. N. Bertram, J. Appl. Phys. 64 pp. 1347-1357, 1988

[90] W. Scholz, J. Fidler, D. Suess and T. Schrefl, *Langevin dynamics of small ferromagnetic particles and wins,* Proceedings of 16th IMACS World Congress on Scientific Computation, Applied Mathematics and Simulation, Aug. 2000, Lausanne, Switzerland. (2000) in press.

[91] W. Scholz, T. Schrefl and J. Fidler, J. Magn. Magn. Mater. **233,** 296 (2001).

[92] W Scholz, T. Schrefl and J. Fidler, IEEE Trans. Magn. **36,** 3189 (2000).

[93] T. Schrefl, J. Fidler, C. Kirk, and J. N. Chapman, *Simulation of magnetization reversal in polycrystalline patterned Co elements,* J. Appl. Phys., vol. 85, pp. 6169, 1999.

[94] T. Schrefl, J. Fidler, R. W Chantrell, and M. Wongsam, *Micromagnetics II: Finite element approaches,* Encyclopedia of Materials: Science and Technology, K. H. J. Buschow, R. W Cahn, M. C. Flemings, B. Ilschner, E. J. Kramer, S. Mahajan (eds.), Elsevier, 2001, pp. 5651-5661

[95] T. Schrefl, J. Fidler, *Numerical simulation of magnetization reversal in hard magnets using a finite element method,* J. Magn. Magn. Mater. 111 (1992) 105

[96] T. Shimatsu, H. Uwazumi, Y. Saki, A. Otsuki, I. Watanabe, H. Muraoka, Y. Nakamura, IEEE Trans. Mag. 37(2001) 1567.

[97] T. Shinjo, T. Okuno, R. Hassdorf, K. Shigeto, T. Ono, *Magnetic Vortex Core Observation in Circular Dots of Permalloy*, Science 289 (230) 930

[98] T. Shinjo, T. Okuno, R. Hassdorf, K. Shigeto, T. Ono, "Magnetic Vortex Core Observation in Circular Dots of Permalloy", Science (2000) vol 289

[99] N. Smith and P. Arnett, *Appl. Phys. Lett.* 78, 1448 (2001).

[100] D. Suess, T. Schrefl, J. Fidler, IEEE Trans. Magn. 36 (2000) 3282.

[101] D. Suess, T. Schrefl, J. Fidler, IEEE Trans. Magn. 37 (2001) 1664.

[102] Dieter Suess, *Micromagnetic simulations of antiferroand ferromagnetic structures for magnetic recording*, PhD thesis, Vienna University of Technology, 2002

[103] D. Suess, V. Tsiantos, T. Schrefl, J. Fidler, W Scholz, H. Forster, R. Dittrich, *Time resolved micromagnetics using a preconditioned time integration method*, J. Miles, J. Magn. Magn. Mater. 248 (2002) 298

[104] S. Sun, C. B. Murray, D. Weller, L. Folks, A. Moser, *Monodisperse FePt Nanoparticles and Ferromagnetic FePt Nanocrystal Superlattices*, Science, vol. 287, pp. 1989, 2000.

[105] K. M. Tako, K.M., M. A. Wongsam. and R. W Chantrell, *Numerical Simulation of 2D Thin Films Using a Finite Element Method*, J. Magn. Magn. Mater., vol. 155, pp. 40, 1996.

[106] B. D. Terns and C. T. Rettner, *Ion Beam Patterning of Magnetic Media,* Datatech edition 6, page 79

[107] B. D. Terns, *Magnetic nanostructures for magnetic recording*, Intermag presentation 2002, Amsterdam

[108] Andre Thiaville, Jose Miguel García, Rok Dittrich, Jacques Miltat, Thomas Schrefl, *Micromagnetic study of Bloch-point-mediated vortex core reversal*, Phys. Rev. B 67 (2003) 094410

[109] J. C. Toussaint, B. Kevorkian, D. Givord, and M. F. Rossignol, in *Proceedings of the 9th International Symposium Magnetic Anisotropy and Coercivity In Rare-Earth Transition Metal Alloys* (World Scientific, Singapore , 1996), p. 59-68.

[110] V. Tsiantos, *Numerical methods for ordinary differential equations in micromagnetic simulations,* Ph.D. Thesis, University of Manchester, 2000.

[111] V. D. Tsiantos, T. Schrefl, J. Fidler, and A. Bratsos, *Cost-Effective Way to Speed-up Micromagnetic Simulations in Granular media,* Applied Numerical Mathematics, in press.

[112] R. A. Victora, *Quantitative theory for hysteretic phenomena in CoNi magnetic thin films*, Phys. Rev. Lett., vol. 58, pp. 1788, 1987.

[113] A. F. Voter, F. Montalenti, T. C. Germann, *Extending the time scale in atomistic simulation of materials*, Annu. Rev. Mater. Res. 32, 321 (2002)

[114] Xiaobin Wang, H.N. Bertram and V Safonov, *Thermal induced reversal in coupled grains and elongated particles,* Phys.Rev. B 2002

[115] D. Weller and A. Moser, *Thermal effect limits in ultrahigh-density magnetic recording*, IEEE Trans. Magn., vol. 35, pp. 4423, 1999.

[116] R. L. White, R. M. H. New, and R. F. W Pease, *Patterned Media: A Viable Routeex to 50 Gbit/in2 and Upfor Magnetic Recording?*, IEEE Transactions on Magnetics 33, 990 (1997)

[117] K. Zhang, D. R. Fredkin, J. Appl. Phys. 85, 5308 (1999).

[118] J. G. Zhu and H. N. Bertram, *Magnetization reversal in CoCr perpendicularthin films*, J. Appl. Phys., vol. 66, pp. 1291, 1989.

[119] J.-G. Zhu, *J. Appl. Phys.* **91**, 7273 (2002).

[120] J. Xue and R. H. Victora, *Micromagnetic predictions for thermally assisted reversal over long time scales*, J. Appl. Phys. 77, 2432 (2000)

[121] B. Yang and D. R. Fredkin, *Dynamical micromagnetics by the finite element method*, IEEE Trans. Magn. vol. 34, pp. 3842, 1998.

[122] OOMMF was developed by M.J. Donahue and D. Porter mainly, from NIST. It is available at http://math.nist.gov/oommf. We used the 3d version of the 1.2 alpha2 release.

[123] http://www.research.ibm.com/resources/news/20010518_pixie_dust.shtml

[124] www.mscsoftware.com

LEBENSLAUF

Dittrich Rok
Rosengasse 12
2601 Sollenau
Geboren in Ljubljana, Slowenien

1982-1984	Volksschule in Slowenien
1984-1990	Grundschule in Schweden
1990-1994	Realgymnasium in Wien und Wr. Neustadt
Juni1994	Reifeprüfung, BORG Wr. Neustadt
1994-1999	Studium der Technischen Physik an der TU-Wien
1999-2000	Diplomarbeit an der EPFL in Lausanne (CH) und Praktikum bei Unaxis in Liechtenstein.
Jan. 2001	Diplom mit Auszeichnung
seit März 2001	Wissenschaftlicher Mitarbeiter in der Arbeitsgruppe von J. Fidler und T. Schrefl. Doktoratsstudium an der Technischen Universität Wien
März 2002- Aug. 2002	Forschungsaufenthalt in der Arbeitsgruppe von Jacques Miltat auf der CNRS Universite Paris-sud im Rahmen des EU Marie Curie Mobilitätsprogramms.
Nov. 2002	Wissenschaftlicher Besuch bei der Arbeitsgruppe von William Bailey an der Columbia University in New York
Juni 2003	Rigorosum

CURRICULUM VITAE

Dittrich Rok
Rosengasse 12
2601 Sollenau
Born in Ljubljana, Slovenia

1982-1984	Elementary school in Slovenia
1984-1990	Elementary school in Sweden
1990-1994	High school in Austria
June 1994	High school final exam
1994-1999	Studying physics at the Vienna University of Technology
1999-2000	Master thesis at the EPFL in Lausanne (CH) and internship at Unaxis in Liechtenstein.
Jan. 2001	Graduated "with excellence" and achieved masters degree in physics
since March 2001	Researcher in the working group of J. Fidler and T. Schrefl Working on dissertation
March 2002-Aug. 2002	Research stay with the EU Marie Curie Host fellowships in the group of Jacques Miltat at the CNRS Université Paris-sud
Nov. 2002	Research visitor to the group of William Bailey at the Columbia University
June 2003	PhD thesis defense

LIST OF PUBLICATIONS

Preprints and electronic versions of the papers can be found on the group's home page:

http://magnet.atp.tuwien.ac.at or http://magnet.atp.tuwien.ac.at/dittrich

[1] R. Dittrich, T. Schrefl, A. Thiaville, J. Miltat, V Tsiantos, J. Fidler, *Comparison of Langevin dynamics and direct energy barrier computation,* J. Magn. Magn. Mater., submitted

[2] R. Dittrich, T. Schrefl, H. Forster, D. Suess, W Scholz, J. Fidler, *Energy barriers in magnetic random access memory elements,* IEEE, 2003, in press.

[3] R. Dittrich, T. Schrefl, D. Suess, W. Scholz, H. Forster, J. Fidler, *Thermally induced magnetization reversal in AFC media,* JAP (2003) in press.

[4] R. Dittrich, A. Thiaville., J. Miltat, T. Schrefl, *A rigorous micromagnetic computation of configurational anisotropy energies in nanoelements,* JAP (2003) in press.

[5] A. Thiaville, J.M. Garcia, R. Dittrich, J. Miltat, T. Schrefl, *Micromagnetic study of Bloch points nucleated vortex core reversal,* Phys. Rev. B. 67 (2003) 094410.

[6] H. Forster, R. Dittrich, T. Schrefl, J. Fidler, *Anisotropie magnetoresistivity effect in a Co nanowire,* Physica B, submitted

[7] T. Schrefl, J. Fidler, R. Dittrich, D. Suess, W Scholz, V. Tsiantos, H. Forster, *Fast switching of mesoscopic magnets,* Spin Dynamics in Confined Magnetic Structures II, Springer Verlag, eds: B. Hillebrands and K. Ounadjela, (2003) in press.

[8] V. Tsiantos, T. Schrefl, W. Scholz, H. Forster, D. Suess, R. Dittrich, J. Fidler, *Thermal Fluctuations in Magnetic Sensor Elements,* Journal Sensors and Actuators (2003) in press.

[9] H. Forster, T. Schrefl, R. Dittrich, W Scholz, J. Fidler *Fast boundary methods for magnetostatic interactions in micromagnetics,* IEEE Trans. Magn., (2003) submitted.

[10] H. Forster, N. Bertram, X. Wang, R. Dittrich, T. Schrefl, J. Fidler, *Energy barrier and effective thermal reversal volume in columnar grains,* J. Magn.Magn.Mater. (2003) in press

[11] T. Schrefl, H. Forster, R. Dittrich, D. Suess, *Reversible magnetization processes and energy density product in Sm-C/Fe bilayers,* JAP (2003) in press.

[12] D. Suess, M. Kirschner, T. Schrefl, W Scholz, R. Dittrich, H. Forster, J. Fidler, *Micromagnetic calculations of bias field and coercivity of compensated ferromagnetic/antiferromagnetic bilayers,* JAP (2003) in press.

[13] R. Dittrich, T. Schrefl, D. Suess, W Scholz, H. Forster, J. Fidler, *A path method for finding energy barriers and minimum energy paths in complex micromagnetic systems,* J. Magn. Magn. Mater. 250 (2002) L12-L19.

[14] R. Dittrich, T. Schrefl, V. Tsiantos, H. Forster, D. Suess, W Scholz, J. Fidler, *Micromagnetic simulation of thermal effects in magnetic nanostructures,* MRS Symposium Proceedings, 746 (2002) 183

[15] Dittrich, R.; Schrefl, T.; Forster, H.; Suess, D.; Scholz, W; Fidler, J.; Tsiantos, V., *Finite element simulation of discrete media with granular structure,* IEEE Trans Magn. 38 (2002) 1967-1969.

[16] D. Suess, V. Tsiantos, T. Schrefl, J. Fidler, W Scholz, H. Forster, R. Dittrich, J. Miles, *Time resolved micromagnetics using a preconditioned finite element method,* J.Magn.Magn.Mater. 248 (2002) 298-311.

[17] H. Forster, T. Schrefl, D. Suess, W Scholz, V. Tsiantos, R Dittrich, J. Fidler, *Domain wall motion in nano-wires using moving grids,* JAP 91 (2002) 6914-6919.

[18] J. Fidler, T. Schrefl, H. Forster, D. Suess and R. Dittrich, *FE-Simulation of fast switching behavior of magnetic nanoelements,* Proceedings of 5th Int. Conference on Modeling and Simulation of Microsystems, Puerto Rico, Eds: M. Laudon and B. Romanowicz, 2002, pp. 348-351.

[19] Fidler, J.; Schrefl, T; Tsiantos, VD.; Forster, H.; Dittrich, R.; Suess, D, *FE-simulation of fast switching behavior of granular nanoelements,* IEEE Trans Magn. 38 (2002) 2520-2522.

[20] Forster, H.; Schrefl, T; Dittrich, R.; Suess, D; Scholz, W; Tsiantos, V.; Fidler, J.; Nielsch, K.; Hofmeister, H.; Kronmuller, H.; Fischer, S., *Magnetization reversal in granular nanowires,* IEEE Trans Magn. 38 (2002) 2580 -2582.

[21] T. Schrefl, H. Forster, J. Fidler, R. Dittrich, D. Suess and W. Scholz, *Magnetic hardening of exchange spring multilayers,* Proc. of XVII Rare Earth Magnets Workshop, University of Delaware, ed: G. Hadjipanayis and M.J. Bonder, 2002, pp. 1006-1026.

[22] T. Schrefl, D. Suess, H. Forster, V.D. Tsiantos, W. Scholz, J. Fidler, R. Dittrich, *Micromagnetic simulations and applications,* Proc. 5th Int. Workshop on Mathematical Methods in Scattering Theory and Biomedical Technology, Corfu, Greece, World Scientific, Eds: D. Fotiadis, Ch. Massalas, (2001) pp. 141-158.

PRESENTATIONS

1. **Thermal Activation in Micromagnetics.** Joint Summer Workshop on Mesomagnetism, Spin Dynamics and Spin Electronics, July 2001, Santorini, Greece
2. **Finite Element Simulation of Discrete Media with Granular Structure.** Intermag 2002, Amsterdam, Netherlands
3. **A method for finding energy barriers and minimum energy paths in complex micromagnetic systems.** Séminaire Magnétisme, Laboratorie de Physique des Solides, 1. July 2002, Orsay, France
4. **Thermally induced magnetization reversal in AFC media. MMM** conference 2002, November, Tampa, Florida, USA, paper DH-10
5. **A rigorous micromagnetic computation of configurational anisotropy energies in nanoelements.** MMM conference 2002, November, Tampa, USA, paper FC-02
6. **Micromagnetic simulations of thermal effects in magnetic nanostructures.** MRS Fall 2002, December, Boston, USA, paper Q4.8
7. **Magnetic domain structures during thermal switching of magnetic thin film elements.** Gamm seminar 2003, Bochum, Germany
8. **Thermische Stabilität von magnetischen Speichermedien.** Seminar am Inst. für Festkörperphysik, März 2003
9. **Thermal stability of magnetic random access memory elements.** Intermag conference 2003, Boston, USA
10. **Anisotropie magnetoresistivity effect in a Co nanowire.** HMM 2003, Salamanca, Spain
11. **Comparison of Langevin dynamics and direct energy barrier computation.** International Conference of Magnetism (ICM) 2003, Roma, Italy